University of Alberta

A Novel Design and Optimization Process of MEMS Devices Using Artificial Intelligence and Finite Element Analysis

by

Hesham Ahmed ©

A thesis submitted to the Faculty of Graduate Studies and Research in partial fulfillment of the requirements for the degree of Master of Science.

Department of Mechanical Engineering

Edmonton, Alberta

Spring 2004

Library and
Archives Canada

Published Heritage
Branch

395 Wellington Street
Ottawa ON K1A 0N4
Canada

Bibliothèque et
Archives Canada

Direction du
Patrimoine de l'édition

395, rue Wellington
Ottawa ON K1A 0N4
Canada

Your file Votre référence
ISBN: 0-612-96439-6
Our file Notre référence
ISBN: 0-612-96439-6

The author has granted a non-exclusive license allowing the Library and Archives Canada to reproduce, loan, distribute or sell copies of this thesis in microform, paper or electronic formats.

The author retains ownership of the copyright in this thesis. Neither the thesis nor substantial extracts from it may be printed or otherwise reproduced without the author's permission.

L'auteur a accordé une licence non exclusive permettant à la Bibliothèque et Archives Canada de reproduire, prêter, distribuer ou vendre des copies de cette thèse sous la forme de microfiche/film, de reproduction sur papier ou sur format électronique.

L'auteur conserve la propriété du droit d'auteur qui protège cette thèse. Ni la thèse ni des extraits substantiels de celle-ci ne doivent être imprimés ou aturement reproduits sans son autorisation.

In compliance with the Canadian Privacy Act some supporting forms may have been removed from this thesis.

While these forms may be included in the document page count, their removal does not represent any loss of content from the thesis.

Conformément à la loi canadienne sur la protection de la vie privée, quelques formulaires secondaires ont été enlevés de cette thèse.

Bien que ces formulaires aient inclus dans la pagination, il n'y aura aucun contenu manquant.

Canada

Abstract

The objective of this thesis is to investigate the design parameters of lateral Electrostatic Comb-Drive actuators, where the effect of these parameters on the actuation performance was explored using Finite Element Analysis (FEA). To achieve this, a 2D model was developed using Reduced Order Modeling (ROM) principles, where the Comb-Drive was reduced into two electromechanical transducer elements. In these elements, the mechanical structures are modeled with equivalent springs, dampers, and masses. The equivalent system value for each element was extracted through a series of FEA. Simulation results were validated using the analytical model obtained from the literature and showed a good agreement. Furthermore, to overcome some limitations in the 2D model, a full 3D parametric model was constructed. This 3D model utilized the application of two different meshing techniques commonly known as, the Volume Refining Meshing (VRM) method, and the Exposed Face Meshing method (EFM). The latter, showed a significant reduction in the computation time over the (VRM) method with better agreement with the analytical results. Finally, a tool was developed to calibrate the (VRM) FE results. In this process, the results obtained from both meshing techniques were used to train a Feedforward Backpropagation Neural Networks. These networks showed a good generalization performance. Finally, general overview of reliability issues related to MEMS devices were discussed. Reliability models and different failure modes/mechanisms were explained. Dynamic analysis was performed to evaluate the reliability of Comb Drive. Dynamic analysis results in conjunction with Fatigue curve (S-N data for polysilicon) were used to estimate the Comb Drive lifetime.

This thesis is dedicated to the greatest source of inspiration in my life, my parents.

Acknowledgements

I would like to take this opportunity to express my sincere gratitude to my supervisor, Dr. Walied A. Moussa. I would like to acknowledge his persistent guidance and encouragement during the course of this work.

My sincere thanks are due to the various faculty members and everyone who helped me to bring this work to existence. It is also my wish to extend special thanks to my fellow graduate students: Khaled Sadek and others for their advice and support. I would also like to acknowledge the financial support provided to me by the Department of Mechanical Engineering and BigBangWidth.

TABLE OF CONTENTS

Chapter 1

Introduction 1

1.1 Motivation 1

1.2 Thesis overview 2

Chapter 2

Background and Literature Review 6

2.1 Introduction 6

2.2 MEMS Background 6

2.3 MEMS Microactuator 9

  2.3.1 Electrostatic actuators 11

  2.3.2 Piezoelectric actuators 12

  2.3.3 Thermal actuators 13

2.4 Comb Drive actuators 14

2.5 Comb Drive design limitations 19

  2.5.1 Side Sticking 20

  2.5.2 Front Sticking 21

  2.5.3 Levitation Phenomenon 22

Chapter 3

Reduced Order Modeling 29

3.1 Introduction 29

3.2 MEMS top-down design 29
3.3 Comb Drive Theory 31
3.4 Reduced order modeling (ROM) 34
  3.4.1 Electromechanical Transducer (TRANS126) 35
  3.4.2 Capacitance Extraction (CMATRIX) 37
  3.4.3 Lumped parameter elements 38
  3.4.4 Circuit Simulation 40
3.5 Results and Discussion 41
3.6 Conclusion 44

Chapter 4

Three-dimensional FE Modeling 59
4.1 Introduction 59
4.2 Motivation and Chapter Overview 60
4.3 Volume Refining Meshing (VRM) method 61
4.4 Finite element procedure for VRM 62
4.5 Exposed Face Meshing (EFM) method 65
4.6 Finite element procedure for EFM 67
4.7 Results and Discussion 69
4.8 Conclusion 72

Chapter 5

Application of Artificial neural network 88
5.1 Introduction 88
5.2 ANN Literature Review 88

5.3 Neural Network Principles 91

5.4 Neural Networks Classification 93

  5.4.1 Supervised learning type 93

  5.4.2 Reinforcement learning type 94

  5.4.3 Self-organising (Unsupervised learning) type 94

5.5 Creating the Neural Network 94

  5.5.1 Network Model key elements 96

    5.5.1.1 The Hidden Layers 96

    5.5.1.2 Learning Rule (Training Function) 97

    5.5.1.3 Data pre-processing and post-processing 98

5.6 Results and Discussion 98

  5.6.1 Effect of the Number of Neurons 99

  5.6.2 Effect of number of training cycles (number of epochs) 100

  5.6.3 Effect of number of Hidden Layers 101

  5.6.4 Final Network 102

5.6 Conclusion 103

Chapter 6

Reliability Modeling 112

6.1 Introduction 112

6.2 Reliability overview 112

6.3 Reliability Models 114

6.4 Failure modes and Mechanisms 116

  6.4.1 Mechanical Fracture 117

  6.4.2 Stiction 119

6.4.3 Friction and Wear 119
6.4.4 Delamination 121
6.4.5 Electrostatic Discharge 121
6.4.6 Parasitic capacitance 121
6.5 Comb Drive reliability analysis 122
6.5.1 Mechanical fracture 123
6.5.1.1 Static-actuation induced failure 123
6.5.1.2 Dynamic-actuation induced failure 125
6.5.2 Fatigue 127
6.5.2.1 Comb Drive Dimensions 128
6.5.2.2 Young's Modulus 128
6.5.2.3 Residual Stresses 129
6.6 Conclusion 130

Chapter 7

Conclusions 140
7.1 Lateral Electrostatic Comb Drive Actuators 140
7.2 Future Work 143

Bibliography 144

LIST OF FIGURES

Figure 2.1: Schematic diagram of Parallel plate capacitor actuator 24

Figure 2.2: (a) Rotary electrostatic micromotor 24

Figure 2.2: (b) Silicon inchworm motor 24

Figure 2.3: Thin film piezoelectric material 24

Figure 2.4: Schematic diagram for thermal pneumatic microactuator 25

Figure 2.5: Schematic diagram for Bimetallic microactuator 25

Figure 2.6: Schematic diagram for array of thermal actuators 26

Figure 2.7: Folded-flexure Comb Drive microactuator fabricated in the MUMPs process (a) Layout. (b) Cross-section A-A' 26

Figure 2.8: Comb finger under levitation force induced by two adjacent fingers biased at positive potential 27

Figure 2.9: Comb finger when differential dc bias is applied to two adjacent fingers 27

Figure 2.10: Comb finger when differential dc bias is also applied to the striped ground conductors 28

Figure 3.1: Design processes for MEMS with the various levels of design and typical modeling approach used at each level. 46

Figure 3.2: Schematic details for one movable finger between two fixed fingers. 46

Figure 3.3: Schematic details for the mutual capacitance between Comb fingers 47

Figure 3.4: Schematic for the electromechanical transducer element (TRANS126) 47

Figure 3.5: Finite element mesh-only air domain shown 48

Figure 3.6: System Capacitance Extraction Procedure 49

Figure 3.7: Reduced Order Model (ROM) for Comb Drive actuator 50

Figure 3.8: The variation of Comb Drive displacement vs. the applied driving voltage, (V): Comparison between analytical and simulation results 50

Figure 3.9: The variation of the Comb Drive displacement vs. the number of moving fingers, (n) 51

Figure 3.10: The variation of the Comb Drive electrostatic force vs. the number of moving fingers, (n) 51

Figure 3.11: The variation of Comb Drive displacement vs. the applied driving voltage, (V) 52

Figure 3.12: The variation of Comb Drive electrostatic force vs. the applied driving voltage, (V) 52

Figure 3.13: The variation of the Comb Drive displacement vs. the gap between Comb fingers, (g) 53

Figure 3.14: The variation of the Comb Drive electrostatic force vs. the gap between Comb fingers, (g) 53

Figure 3.15: The variation of the Comb-Drive displacement vs. the overlap distance (L) between the Comb Fingers 54

Figure 3.16: The variation of the Comb-Drive electrostatic force vs. the overlap distance (L) between the Comb Fingers 54

Figure 3.17: The variation of the Comb Drive displacement vs. the driving voltage at different finger thickness, with n = 20 fingers, g = 2 µm, L = 11 µm and b = 2 µm 55

Figure 3.18: The variation of the Comb Drive electrostatic force vs. the driving voltage at different finger thickness, with n = 20 fingers, g = 2 μm, L = 11 μm and b = 2 μm 55

Figure 3.19: The variation of the Comb-Drive Displacement versus driving voltage for several folded-flexure spring designs. All designs have a folded-beam width 1 μm and beam thickness 2 μm 56

Figure 3.20: The variation of the Comb-Drive generated electrostatic force versus driving voltage for several folded-flexure spring designs. All designs have a folded-beam width 1 μm and beam thickness 2 μm 56

Figure 3.21: The variation of the system overall stiffness of Comb-Drive versus the length of the folded-flexure spring, (L). All designs have a folded-beam width 1 μm and beam thickness 2 μm 57

Figure 3.22: The qualitative effect of all studied parameters on the system overall stiffness 57

Figure 4.1: Flow chart for the coupled-field electrostatic structural analysis using (VRM) method 74

Figure 4.2: Elements description used in the (VRM) method: (a) SOLID123 and (b) SOLID92. 75

Figure 4.3: Flow chart for the coupled-field electrostatic structural analysis using (EFM) method 76

Figure 4.4: Electrostatic mesh refinements for Comb Drive Actuator 77

Figure 4.5: Mechanical Mesh sensitivity analysis for Comb Drive Actuator 77

Figure 4.6: Electrostatic Mesh sensitivity analysis for Comb Drive Actuator 78

Figure 4.7: The variation of Comb Drive displacement vs. the applied driving voltage, (V): Comparison between analytical and simulation results 79

Figure 4.8: The variation of the Comb Drive displacement vs. the number of moving fingers (n) 80

Figure 4.9: The variation of the Comb Drive stresses vs. the number of moving fingers (n) 80

Figure 4.10: The variation of the Comb Drive displacement vs. the applied driving voltage (V) 81

Figure 4.11: The variation of Comb Drive stresses vs. the applied driving voltage(V) 81

Figure 4.12: The variation of the Comb Drive displacement vs. the gap (g) between Comb fingers 82

Figure 4.13: The variation of the Comb Drive stresses vs. the gap (g) between Comb fingers 82

Figure 4.14: The variation of the Comb Drive displacement vs. the driving voltage at different finger thickness 83

Figure 4.15: The variation of the Comb Drive stresses vs. the driving voltage at different finger thickness 83

Figure 4.16: Comb Drive displacement vs. the driving voltage for different folded flexure spring design 84

Figure 4.17: Comb Drive stresses vs. the driving voltage for different folded flexure spring design 84

Figure 4.18: Comb Drive displacement vs. the number of moving fingers (n) in dimensionless 85

Figure 4.19: Comb Drive displacement vs. the applied driving voltage (V) in dimensionless 85

Figure 4.20: Comb Drive stresses vs. gap (g) between Comb fingers in dimensionless 86

Figure 4.21: Comb Drive displacement vs. the driving voltage for different finger thickness in dimensionless 86

Figure 4.22: Comb Drive displacement vs. the driving voltage for different folded flexure spring design in dimensionless 87

Figure 5.1: General model of neuron 104

Figure 5.2: Common Transfer Functions for Neural Networks 104

Figure 5.3: Different architectures of networks include single-layer and multi-layers networks 105

Figure 5.4: Typical Supervised Learning Scheme 106

Figure 5.5: General architecture of Feedforward Backpropagation multi-layer neural network 106

Figure 5. 6: Effect of number of neurons on network performance as function of mean absolute error 107

Figure 5.7: Effect of number of neurons on network performance as function of correlation coefficient 107

Figure 5.8: Effect of number of training cycles on network performance as function of mean absolute error 108

Figure 5.9: Effect of number of training cycles on network performance as function of correlation coefficient 108

Figure 5.10: Mean absolute errors for the new 2-hidden layers network architecture 109

Figure 5.11: Final network performance vs. number of neurons for first hidden layer 110

Figure 5.12: Final network performance vs. number of neurons for second hidden layer 110

Figure 5.13: Final network output prediction vs. target data for displacement ratio network 110

Figure 5.14: Final network output prediction vs. target data for Von-Mises stress ratio network 111

Figure 6.1: pdf of the normal distribution. 131

Figure 6.2: Typical SN curve for a ductile material. 132

Figure 6.3a: SEM picture of released Comb 132

Figure 6.3b: SEM picture of a stiction Comb 132

Figure 6.4: Von mises stress distribution for Comb Drive at 30 DC Volts load 133

Figure 6.5: Von mises stress distribution for Comb Drive at maximum actuation range 133

Figure 6.6: Comb Drive failure when two fingers come into contact and short out the device 134

Figure 6.7: Normal distribution of the Quality factor for Comb Drives 134

Figure 6.8: Effect of damping on Comb Drive performance at quality factor 15 during resonance 135

Figure 6.9: Effect of damping on Comb Drive performance at quality factor 30 during resonance 135

Figure 6.10: Effect of damping on Comb Drive performance at damping ratio 0.03 136

Figure 6.11: Effect of damping on Comb Drive performance at damping ratio 0.125 136

Figure 6.12: Effect of damping on Comb Drive performance at damping ratio 0.5 137

Figure 6.13: The variation of Comb Drive Displacement vs. Damping ratio at 30 Volts DC pulse 137

Figure 6.14: The variation of X-Displacement vs. the Quality factor for Comb Drives 138

Figure 6.15: Normal distribution of X-Displacement for the Comb Drives determining Reliability rate 139

Figure 6.16: Goodman's curve for Comb life estimation 139

LIST OF TABLES

Table 3.1: Design parameters for Comb Drive Actuator 48

Table 3.2: Calculated A_{nm} values for Equations (3.5.9.1-5) 58

Table 4.1: Design parameters for Comb Drive Actuator 75

Table 4.2: Comparison of simulation process time for different meshing methods 78

Table 4.3: Comparison between meshing methods 79

Table 5.1: Design parameters for Comb-Drive actuator as an input to neural network 105

Table 6.1: Common MEMS failure mechanisms 131

Table 6.2: Dynamic analysis results (Effect of Quality factor on system response) 138

Chapter 1

Introduction

1.1 Motivation

Making small machines that are almost invisible has been one of the dreams of scientists and engineers for a long time. Such a dream started becoming true nearly a decade ago with the introduction of microelectromechical systems (MEMS). MEMS devices are composed of both mechanical and electrical devices. Those devices are sufficiently small that they can be integrated on-chip. Researchers have achieved a remarkable progress in the design and fabrication of MEMS devices. MEMS devices are used in many application and disciplines such as aerospace industries, optics and telecommunication, automotive industry, biomedical technologies, chemical analysis systems, and industrial control applications. MEMS greatest asset lies in the ability to produce mechanical motion in a small scale. Such devices typically have low power and produce fast motions, which are generated by microscale phenomena such as strong electrostatic forces and electromagnetic forces. A good example of the electrostatic forces is the actuation mechanism in the Comb Drive actuators.

Comb Drive actuators are the main source of mechanical motion in many MEMS devices including optical switches and relays, optical scanners, micro mirrors, and optical shutters. Comb Drive actuators also have enormous applications like resonators, microgrippers, micromotors, and x-y microstages. Due to the popularity of usage of Comb Drive actuators and the advantages associated with the electrostatic actuation, many researchers and MEMS designers are motivated to concentrate their research efforts on designing more powerful and cost effective Comb Drives. However, one of the fundamental problems associated with the MEMS design process is the time and cost of the fabrication process. Modeling of MEMS devices is a good solution for these issues. Before any MEMS design is submitted to fabrication, prior modeling and analysis will provide valuable information about the expected device's performance. Subsequently, the designer can modify the device specification to meet the required function. Previously generated accurate models of MEMS devices, for example are assisting in enhancing the integrity of the system level design. This motivates many MEMS designers, including the author of this thesis to focus their research efforts on developing accurate models for MEMS devices. In this thesis, effort is directed to develop an accurate model that is used for simulation and analysis of Comb Drive actuators.

1.2 Thesis overview

The objective of this thesis is to develop a design framework and optimization methodology that can be applied to a wide variety of MEMS devices, in order to investigate the device actuation performance. The current work, focuses on developing this process with particular interest to lateral electrostatic comb drive actuators. In this process, the design parameters of lateral Electrostatic Comb Drive actuators and their effect on the actuation performance were explored using Finite Element Analysis (FEA). To establish this framework a robust and accurate 2D and 3D FE models were developed. The 3D model utilized the application of two different meshing techniques commonly known as the Volume Refining Meshing (VRM) method, and the Exposed Face Meshing method (EFM). The finite element models were created in a parametric manner, so they can be used to simulate any required Comb Drive dimensions. The results of these models were used to develop an optimization tool that can be effectively used to come up with an optimized Comb Drive design. This tool can assist and speed up the design process of the MEMS devices. Artificial intelligence technique such as artificial neural network was used to develop this tool using the FE results.

The main contribution of this work to the design and analysis process of MEMS devices is not only the development of fast and accurate parametric FE models that can be used effectively to simulate any Comb Drive design, but also the development of a neural network optimization tool. This tool is capable of calibrating and correcting the FE results of the VRM method using the accurate FE results produced by the EFM method. The accuracy of the EFM method results qualifies it to be the closest results that could be achieved to match the accuracy of the experimental results. Thus, the designer is no longer required to worry about the accuracy of his FE analysis results anymore. Since, using this tool will upgrade the VRM results to closely match the actual experimental analysis results without the need to fabricate the device, especially in the early design phases where the cost of the fabrication process is important issue. This tool will produce a calibration factor based on the network inputs, which are the device design parameters. This factor will rectify the VRM results and provide the designer with a clear vision of how the device works as if it was already fabricated. The following outlines the different steps that were followed to achieve the thesis objective and lists the different techniques that were implemented in each chapter.

Chapter two discusses the different types of Microactuators and their applications. This chapter also classifies the Microactuators according to their principles of actuation.

Finally, it describes some of the most critical design limitations, which are normally associated with lateral electrostatic Comb Drive actuators. Furthermore, it explains the suggested solutions available in the literature to overcome these limitations during the design phase.

Chapter three documents the development of a 2D finite element model for the Comb Drive. This model was constructed utilizing the Direct Coupled-Field Analysis method in the commercial finite element package ANSYS. In this method, the device is reduced to a number of lumped elements, which capture the device behavior through Reduced Order Modeling (ROM) principles. The equivalent system value for each element was extracted through a series of FEA. This model was built in a parametric fashion in order to be flexible enough to analyze and simulate any required Comb Drive geometry. Simulation results were validated using an analytical model obtained from the literature and showed a good agreement with a discrepancy of less than 5%.

In Chapter four, a full 3D FE model for the lateral electrostatic Comb Drive was developed in order to overcome some limitations in the 2D model. This 3D model utilized the application of two different meshing techniques commonly known as the Volume Refining Meshing (VRM) method, and the Exposed Face Meshing method (EFM). On one hand, the EFM method permits the independent refinement of the electrostatic and the mechanical meshes while keeping full compatibility between the two meshed domains. On the other hand, the VRM method requires both the electrostatic and the mechanical meshes to be refined together at the same time; which result in a large problem size for complex structures with high aspect ratio. While the VRM method requires meshing of air gaps between the conductors, the EFM method uses the boundary element technique to map and calculate the electrostatic forces on the surfaces of the structure conductors, which eliminates the need to mesh the air gaps between the conductors. This model was used to perform a parametric study that was carried out to optimize the design parameters of the Comb Drive. The EFM method showed a significant reduction in the computation time over the VRM method with better agreement with the analytical results within a range of 10%.

Based on the numerical results obtained from chapter four, a tool that can be used to calibrate and optimize the FE results produced by the VRM method was developed in chapter five. In this process, the results obtained from both meshing techniques of the parametrically studied Comb Drive were used as the training data to train Feedforward Backpropagation Neural Networks. The inputs to the networks were the Comb Drive design parameters; and the desired network target was the displacement ratio of both FE results for network number one and Von-Misses stress ratio for network number two. Network validation and a measure of network accuracy in terms of mean absolute error and coefficient of correlation were presented.

Chapter six addresses some of the reliability issues related to the design and operation of electrostatic Comb Drive actuators such as, mechanical failure, stiction, wear…etc. Based on the results obtained from a time domain dynamic analysis where the studied Comb Drive was excited at the resonance frequency, the different possible failure modes of the Comb Drive are explained. Using the S-N curve results of the Polysilicon material and the applied operational stresses from the dynamic analysis results, fatigue life of this device is calculated.

Lastly, chapter 7 concludes this thesis and the key findings are highlighted.

Chapter 2

Background and Literature Review

2.1 Introduction

In this chapter, a brief background about the MEMS technology is presented and the literature is reviewed for research work conducted in the area of lateral electrostatic Comb Drive actuators. Design considerations and limitations related to operation of Comb Drive actuators are also included and the precautions required to follow in order to avoid those limitations during design phase are also explained.

2.2 MEMS Background

Introducing the technology of integrated circuit (IC) fabrication in early 1960 was a major step toward the ability to make objects smaller and open the gate to develop further future technologies that can be used to fabricate MEMS devices. These microfabrication technologies are based on silicon processes like photolithography, etching, and thin film deposition etc. They enable the miniaturization of electrical devices as well as micromechanisms and Microactuators. Those miniature devices can be batch fabricated on large area silicon substrates. The three main fabrication technologies are; bulk micromachining, surface micromachining and molding. Those fabrication technologies have the following features that enable MEMS devices to function well in the world of Microsystems:

- Definition of small geometries
- Precise dimensional control
- Design flexibility
- Interfacing with control electronics
- Repeatability, reliability, and high yield
- Low cost per device

MEMS is the acronym for Microelectromechanical Systems. Microelectromechanical Systems (MEMS) as they referred to in North America and Microsystems Technology (MST) in Europe and Japan, are composed of both mechanical and electrical devices. From the physical point view, MEMS is the integration of mechanical elements and electronics on a common silicon wafer using microfabrication technologies. This form of integration enables the whole system to do a certain tasks such as sensing, control, reacting to a specific input, and driving another system to establish a required function [1]. More generally speaking, MEMS is simultaneously a toolbox, a physical product and a methodology all in one. As the name implies, "Micro" establishes the size definition, "Electro" refers to the intimate involvement of electricity or electronics and "mechanical" infers that some moving parts are included.

The term, "MEMS", was coined around 1987, when a series of three workshops on microdynamics and MEMS was held in July 1987 in Salt Lake City, Utah; in November 1987 in Hyannis, Massachusetts; and in January 1988 Princeton, New Jersey. MEMS is application driven and a technology that has emerged as an interdisciplinary field that involves many areas of science and engineering. Miniaturization of mechanical systems promises unique opportunities for new directions in the progress of science and technology. Microelectromechanical systems are inherently smaller, lighter, and faster, they can be batch fabricated and are cost effective and usually more precise than their macroscopic counterparts.

Another advantage for those systems arises due to scaling effect. The same physical laws and material constants govern the micro as well as the macro world. Scaling macrosystems down the micro size shifts the influence of individual parameters on the total system dramatically. Compared to macro or mini-systems, microsystems allow completely novel mechanical designs. Volumes and masses for example decrease super-proportionally (cubically) compared to lengths. Scaling down mechanical systems leads to stiff and comparatively lightweight structures with high shock resistance [2].

MEMS actuators are made of mechanical elements, and signal processing and control units that can be built by using electronics circuits. So, the whole system can be integrated on a single chip without any extra assembly process. The motivation for integrating the whole system on a single chip is miniaturization and parallel processing which leads to inexpensive fabrication in large quantities. Miniaturization has the ability to make devices with functions that cannot be realized with traditional technologies.

The most developed MEMS (micro electro-mechanical systems) are found in microfluidic systems (Inkjet print heads [3], microvalves [4] and micropumps [5]) and micro-optical systems (micromirrors [6], microscanners [7], microshutters [8] and microswitches [9]). They can be combined with microelectronics and microsensors to form an integrated on-chip or hybrid-assembled system. Other MEMS-actuators like microgrippers [10], microrelays [11] , AFM heads or data storage devices, are promising devices for future medical, biological and technical applications like minimally invasive surgery or the vast field of information storage and distribution. Data storage systems as well as AFM and STM tools use Microactuators in their head carriers to achieve ultra high density recording / scanning [12-14]. Due to the continuous efforts of technology development in the field of MEMS, new branches of MEMS technologies have appeared such as microoptoelectromechanical systems (MOEMS) [15], micrototal analysis systems (μTAS), and nano-litre dosing systems [16].

One example of MEMS applications summarize the definitions of the above mentioned components of Microsystem is the airbag deployment system in an automobile, in which the impact of the car in a serious collision is felt or sensed by a micro inertia sensor built on the principle of a microaccelerometer. The sensor generates an appropriate signal, which is processed by the transduction unit, which actuates an air inflation system that deploys the airbag to protect the passengers and the driver from serious injuries. The following paragraphs focus on discussing the different actuation mechanisms for the MEMS Microactuators with a particular interest to the electrostatic Comb Drive actuators.

2.3 MEMS Microactuators

Microactuators are the backbone of many MEMS devices. Their functions are to provide mechanical motions that perform certain physical task. They are used as transducing elements in a wide variety of MEMS sensors. These devices utilize the high sensitivity of the frequency of a mechanical resonator to physical or chemical parameters that affect its potential or kinetic vibrational energy. Those structures are used for a wide variety of sensing applications such as sensing pressure, acceleration and vapor concentration. Also, they are used to drive other microsystems, such as micromirrors, to function as a scanner or a switch. They also could actuate micropumps for microfluidics systems. Microactuators can be excited in several ways, including piezoelectric films, thermal expansion, shape memory alloy principle, electrostatic forces, and electromagnetic forces. Microactuators can also be classified according to their output motion, where either linear motion or angular motions are produced.

Rotational and linear micromotors are often found to be a key part of micromechanical systems allowing them to perform physical functions. They can be used in x-y microstages, for aperture control in microphotonics, driving forces for microrelays, micromirrors and microgrippers. They also initialize mechanical systems, carry out on-chip assembling and raise pop-up structures. The most commonly used activation principle for micromotors is the electrostatic field between the plates of capacitors including comb drives [17].

Electrostatic actuation is the most applied actuation principle combining versatility and simple technology. It does not require additional elements like coils or cores, or special materials like shape-memory-alloys or piezoelectric ceramics. Above that, the electrostatic actuation draws its force from the relation of surface to spacing and not from relation of volume to spacing like electromagnetic actuation, i.e. it is less affected by scaling and more favorable for VLSI actuators. Scaling analysis suggest that size reduction makes electrostatic designs more advantageous over the electromagnetic versions which dominate at macro dimensions [18]. A brief discussion is given to the microactuators according to their actuation principles.

2.3.1 *Electrostatic actuators*

Most of the electrostatic actuators operation principles are based on the simple parallel plate capacitor actuation theory. Electrostatic force is created between two plates (electrodes) when a potential difference is applied across the two plates. Usually the two plates are separated by dielectric material such as air. Figure 2.1 at page 24 illustrates a schematic diagram for the parallel plate capacitor. The electrostatic force F generated between the two plates can be defined as:

$$F = \frac{1}{2}\frac{\partial U}{\partial g}V^2 \qquad (2.3.1.1)$$

Where V is the applied voltage, g is the gap between the two plates, and U is the energy stored in the parallel plate capacitor. This energy can be obtained from:

$$U = \frac{1}{2}CV^2 \qquad (2.3.1.2)$$

Where C is the capacitance, which is function of the plate's geometry and can be calculated from equation (2.3.1.3) and A is defined as the plate's cross-section area.

$$C = \epsilon_r \epsilon_o \frac{A}{g} \qquad (2.3.1.3)$$

Where ϵ_r is the relative permittivity of the dielectric material between the two electrodes and ϵ_o is the permittivity in the free space and equal to 8.85 pF/m. Electrostatic actuators are the most popular microactuators among their counterparts. They are used in a wide variety of MEMS applications including electrostatic motors (both linear and angular), comb drive actuators, and gyroscopes etc. Figure 2.2 at page 24 illustrates some scanning electron microscope (SEM) images for a group of electrostatic actuators.

2.3.2 Piezoelectric actuators

Piezoelectricity is phenomenon in which a mechanical stress on a material (single crystal of quartz) produces an electrical polarization and reciprocally, an applied electric field produces a mechanical strain. Pierre Curie and his brother discovered this effect in 1880. This effect can be used to sense mechanical stresses and as an actuation mechanism. Figure 2.3 at page 24 shows a schematic for the components of a typical thin film piezoelectric material used in piezoelectric actuators. The film consists of a piezo-material layer surrounded by metallization layers from both sides. The piezoelectric effect is reversible, such that the application of a voltage ΔV gives rise to a corresponding force, ΔF, this force is given by equation (2.3.2.4).

$$\Delta V = \frac{d\,L}{\varepsilon_o \varepsilon_r A} \Delta F \tag{2.3.2.4}$$

Where, d is the piezoelectric coefficient, L is the thickness of the film, A is the film cross-section area, and ε_o and ε_r are the relative permittivity for air and the piezoelectric material respectively. Normally the resulted displacement is very small if a single piezo-film is used. Typical values for displacement vary between 10^{-10} and 10^{-7} cm/V. Thus, to obtain displacements on the order of micrometers (μm), voltages exceeding 1000 volts are often required, unless stacked actuators or mechanical motion amplification methods are used [19]. The required high voltages make piezoelectric materials poor actuators for displacements in the micron regime, but they are very precise actuators on the subnanometer scale. Piezoelectric actuation is ideal, however, for scanning tunneling microscopes (STM) tip [20], where small, precise displacements are required. Piezoelectric materials are also very useful in micromachined transducers such as surface acoustic wave (SAW), accelerometers, and microphones.

2.3.3 Thermal actuators

Thermal actuators are a popular category of actuators. Four different thermal actuation mechanisms are employed in MEMS; thermopneumatic, bimetallic, mechanical thermal expansion, and shape memory alloy. Thermal pneumatic actuators use the expansion of a gas or a liquid to create a mechanical force resulting in the actuation of the device. As shown in Figure 2.4 at page 25, a thermal pneumatic actuator consists of trapped volume of gas or liquid in a sealed cavity containing a thin film-heating resistor along one side of the cavity, with a flexible diaphragm wall forming the opposite side of the cavity. Upon heating, the fluid in the chamber expands and evaporates, raising the pressure in the sealed cavity and causing the flexible diaphragm to expand [21].

The term Shape Memory Alloys (SMA) is applied to group of metallic materials that demonstrate the ability to return to some previously defined shape or size when subjected to the appropriate thermal procedure. Generally, these materials can be plastically deformed at some relatively low temperature, and upon exposure to some higher temperature will return to their shape prior to the deformation, exerting a substantial force that can be used as source of actuation. Materials that exhibit shape memory only upon heating are referred to as having a *one-way shape memory*. Some materials also undergo a change in shape upon recooling. These materials have a *two-way shape memory*. Nickel-titanium (NiTi) alloys are the most commonly used material for shape memory alloy actuators. The properties of the NiTi alloys, particularly, indicate their probable greater use in biomedical applications. The material is extremely corrosion resistant and demonstrates excellent biocompatibility. Thermal bimetallic actuators consist of two different materials with different thermal expansion coefficients. The two metals are combined together to form a bimetal strip that will bend when heated or cooled from the initial reference temperature due to incompatible thermal expansions of the materials that are bonded together. Figure 2.5 at page 25 shows a cantilever bimetallic structure that can be used as a microvalve in MEMS devices [22].

The actuation principle of mechanical thermal expansion is similar to bimetallic microactuators. The only difference is that mechanical thermal expansion microactuators are made of the same material. Figure 2.6 at page 26 shows scanning electron microscope (SEM) picture of a cascade of thermal actuators. In the thermal actuators, actuation is due to thermal expansion of the actuator arm. When electric current passes through the actuator arm, the heat generated in the arm due to electrical resistance causes arm deflection.

2.4 Comb Drive actuators

The Comb Drive actuator consists of two interdigitated finger structures, where one Comb is fixed and the other is connected to a compliant suspension, this suspension can have different shapes and different designs. Those designs could be found in the work published by Rob et al. [23]. Applying a potential difference across the Comb structure will result in a deflection of the movable Comb structure, this deflection is due to the generated electrostatic forces in the system, generated by the parallel plate capacitor effect described before. When a voltage is applied, the moving Comb fingers move into the stationary Comb causing the desired system actuation. A detailed explanation for the theory of the electrostatic forces operating in a micromechanical comb drive actuator is presented in the work published by Johnson et al. [24]. Because the main driving force in the Comb is an electrostatic force which is everywhere around the Comb, it is a good common practice to locate a ground plane under the Comb fingers which is normally connected to the same potential as the movable Comb in order to prevent electrostatic pull-down forces to the substrate. The Comb Drive can be fabricated via a surface-micromachining fabrication technology such as the Multi-User MEMS Process service (MUMPs). In this process, the Comb components are made entirely from a deposited polysilicon film. Figure 2.7 at page 26 shows a typical layout of the Comb Drive structure with the corresponding system components. Comb drive motion is sensed capacitively, by measuring the change in the capacitance between the comb fingers at the sensing pad of the device.

In 1982, Petersen et al. [25] helped launch a new field by authoring a truly visionary publication, in which he advocates the notion of using micro-electronics processing techniques and microelectronics materials to build microscopic parts with a mechanical function, using silicon as mechanical material. In less than a year, University of California at Berkeley was the first to demonstrate that micromechanical structures can be built using polycrystalline silicon through their MEMS research. Howe et al. [26] demonstrated techniques to fabricate microbeams from polycrystalline silicon (polysilicon) films. The first freestanding polysilicon structure in a microsensor was a doubly supported microbeam, 1.2 μm thick and offset from the single-crystal surface by 1 μm. The beam was 20 μm wide and 115 μm long and positioned over a drive electrode utilizing the electrostatic force as actuation mechanism, which caused it to resonate, and sense electrodes to detect its motion. This beam was incorporated into a vapor-sensor to detect a mass-loading change due to vapor absorption. Research on this sensor by R T Howe at BSAC demonstrated that polysilicon is a durable material for micromechanics capable of many flexures without changing its mechanical properties [27].

In further work with electrostatic forcing, Howe and student W. Tang first constructed a poly-silicon comb drive resonant actuator which employs Electrostatic force in a flexure structure to cause it to move parallel to the substrate surface [28] . Since that time, the comb drive has become a very frequently used microactuator both for resonant and non-resonant systems. Because the actuated part is a flexing structure, there is no surface friction in its motion, and it can be driven in resonance with a very high mechanical quality factor (Q) value (100,000 in vacuum). Much work is continuing on comb drive resonators and their applications and they have been made by bulk micromachining and surface micromachining. Vibrating micromechanical structures are useful for a variety of sensors and actuators. For sensing, one can make use of the dependence of the frequency of a mechanical resonator on physical or chemical parameters that affect the vibrational energy. Microfabricated resonant structures for sensing pressure, acceleration, and vapor concentration have been demonstrated. An elegant example of resonant drive for actuators is provided by the successful Bulova Accutron® wristwatch movement in which an electronic tuning fork is coupled mechanically to a rotating mechanism. Recently, some very spectacular mechanisms have been made using polysilicon surface micromachining at the Sandia Laboratories in New Mexico, USA. Sandia was able to develop a microengine that utilized an array of electrostatic comb-drive actuators to provide output in the form of a continuously rotating output gear approximately 50 μm in diameter that is capable of delivering torque to a micromechanisms. The microengine can be operated at varying speeds and its motion can be reversed [29].

Another impressive application of the electrostatic actuation and comb drive actuators is the AD-XL50 microaccelerometer produced by Analog Devices Inc. It is a fully integrated accelerometer device that is used for automobile airbag deployment systems [30]. A large actuation stroke (displacement) comb drive actuator with low driving voltage is the ultimate design goal for MEMS engineers. A suspension that is compliant and flexible enough in the direction of displacement and stiff in the orthogonal directions is required to achieve high displacement with lower driving voltage and avoid many unfavorable operation problems. Several studies have been conducted to investigate this key factor to achieve that objective. For example, Jaecklin et al. [31] have designed and fabricated comb drive actuators with sub-micrometer-wide suspensions.

This design consists of a 16-finger actuator with 300 μm long flexure suspension beams. The beam profile is 0.8 μm wide and 2 μm in height. Experimental work showed that due to the very flexible suspension (low spring constant 9.1 mN m^{-1}) only low voltage around 15 volts was required to achieve a 7.3 μm displacement. The conclusion of this work was highlighted that comb drive displacement is a function of its suspension spring constant and the maximum displacement is bounded by electromechanical side instability (sticking phenomenon), this phenomenon is explained in details in the comb drive design limitation section of this thesis.

Rob et al. [23] published another study that addresses the different possible designs for the comb drive suspension and compared two different designed referred to as crab-leg flexure and folded-flexure respectively. The comb drive consists of 30 fingers with gap spacing of 1.6 and 2.6 μm for two crab-leg flexure designs consisting of a thigh segment of length of 500 μm and a shin of length of 50 μm and a beam width of 4.7 μm and the beam thickness was 1.4 μm. The comb drive displacement was found to be 5 and 6.5 μm for driving voltage of 15 volts. On the other hand, for the folded-flexure designs, comb structures with, respectively, 136 and 88 fingers were employed. The gap spacing equals 2.2 μm and the length of the beams in the folded flexure is 500 μm. The beam width b is 4.8 μm and the beam thickness h is 1.5 μm. The comb drive displacement was found to be 29 and 12 μm for driving voltage of 15 volts. This study showed that the folded-flexure design strongly reduces the suspension spring constant and exhibits a much larger linear deflection range. Therefore, this design is very suitable for large deflection actuators.

A further investigation of the folded-flexure spring design was proposed by Chihchung et al. [17]. This group proposed the development of a lateral comb-drive actuator with a thinned three-folded spring. The three-folded spring design consists of two clamped-guided beams. Each clamped-guided beam consists of three serial parallel beams. The spring constant of this new design is two thirds of the commonly used two folded-flexure spring design. Therefore, for the same deflection, this design can utilize a driving voltage $\sqrt{2/3}$ times less than the two-folded spring design. The net effect is this new actuator structure enables a large displacement under the same applied voltage as that for a traditional comb-drive actuator with a two folded-flexure spring. Guangya et al. [32]

proposed an improved version of the two folded-flexure spring design. In their work, the suspension beam segments are slightly tilted. Using such suspension, the stability of the comb drive actuator is improved and the stable travel range is enhanced. Experimental results showed that the maximum stable displacement of the comb drive actuator was improved from 33 μm (conventional folded beam with no tilting) to 40 μm with 10 μm tilting, 52 μm at 20 μm tilting and 61 μm at 30 μm tilting. Results also showed that, using this design enables an additional reduction in the finger gap spacing while the stable travel range of the comb drive can be the same as the conventional folded-beam suspension design. Therefore, a lower driving voltage can be achieved.

2.5 Comb Drive design limitations

Sticking phenomenon and the Levitation effect are the two major design limitations associated with the electrostatic Comb Drive actuator and a proper course of action has to be followed during the design phase to overcome those problems. The movable Comb finger will stick on the side of the fixed fingers (Side Instability or Side Sticking) or on the front ends of the fixed fingers (Front Sticking) at a critical voltage. The front sticking normally happens for a very rigid suspension of the movable Comb fingers. The Levitation effect results in an additional displacement in the vertical direction (Z-direction) as the moving fingers are elevated away from the surface of the substrate. This could be very undesirable situation in some applications such as micromirrors actuated by the Comb Drive, as this will lead to misdirection of the light or laser beam reflected by the micromirror. In the following few paragraphs a detailed discussion about the cause of those phenomena and how to avoid them during the design is introduced.

2.5.1 Side Sticking

A movable finger placed between two fixed fingers is in an inherently unstable position, when a voltage is applied, not only an electrostatic force is generated in the actuation direction (x-direction) but also another electrostatic force is generated in the y-direction, this force will produce another displacement in the y-direction, trying to minimize the gap between the Comb fingers pulling the fingers toward each other in the y-direction, this force can be calculated as:

$$F_y = \frac{n \in t l V^2}{2}\left[\frac{1}{(g-y)^2} - \frac{1}{(g+y)^2}\right] \qquad (2.5.1.5)$$

Where *y* is the displacement in the y-direction and *l* is the initial overlap length between the fingers. At high voltages the electrostatic force is high enough that the mechanical force created in the suspension beams cannot compensate it. Normally this force is on both sides of the Comb finger and cancels each other's. However when the first derivative of the electrostatic force with respect to y becomes larger than the restoring spring constant in y-direction, Side Instability (i.e. side sticking) will happen in the Comb Drive. Hence a stable Comb operation is bounded by $K_y > K_{cr}$ where K_y is the spring stiffness in y-direction and K_{cr} is the critical spring stiffness where sticking occurs and can be calculated as:

$$K_y > K_{cr} = \left[\frac{\partial F_y}{\partial y}\right]_{y \to 0} = \frac{2n \in t l V^2}{g^3} \qquad (2.5.1.6)$$

The corresponding operation voltage is called side-instability voltage V_{si} and can be expressed as:

$$V_{si}^2 = \frac{g^2 K_x}{2 \epsilon n t}\left(\sqrt{\frac{2K_y}{K_x} + \frac{l^2}{g^2}} - \frac{l}{g}\right) \qquad (2.5.1.7)$$

This equation gives the sticking voltage and K_y in the equation refers to the spring stiffness in the deflected state, since side sticking occurs only when the Comb is actuated, as it equals to:

$$K_y = \frac{200 E I}{3 L \delta_x^2} \qquad (2.5.1.8)$$

Where L is the length of one beam and δ_x is the deflection in x-direction (i.e. actuation direction), and the maximum deflection X_{si} that can be obtained before side sticking (pull-in) occurs is [31]:

$$X_{si} = g\sqrt{\frac{K_y}{2K_x}} - \frac{l}{2} \qquad (2.5.1.9)$$

Equations (2.5.1.7) and (2.5.1.9) indicate that side-instability voltage and maximum deflection are directly proportional to the gap spacing and increase with the spring stiffness ratio K_y/K_x. This indicates that Comb Drive actuators with small gap spacing are more subjected to side instability and that spring designs with large stiffness ratio are preferred for large-deflection and avoiding the side instability also.

2.5.2 Front Sticking

In addition to the actuation force generated between the fingers in the x-direction another electrostatic force is generated according to the parallel plate capacitor effect between the front ends of the movable fingers and the parallel part of the fixed fingers in front of it. This force can be approximated as:

$$F_p = \frac{n \in t b V^2}{(d - x)} \qquad (2.5.2.10)$$

Where d is the initial distance of the front ends of the movable fingers with the fixed ones, b is the width of the finger, and x is the displacement in x-direction. For equilibrium the spring force has to compensate the electrostatic forces. If the spring stiffness in the y-direction is large enough to prevent side sticking and the driving voltage was high enough to pull the fingers to make them completely engaged with the fixed fingers, front sticking will happen. As the length of the suspension beams increase, the spring stiffness decreases so a small driving voltage will be required to achieve the desired actuation (i.e. displacement), but in the same time a weak spring may lead to higher displacement, which may cause side sticking. To achieve equilibrium as condition must be satisfied as:

$$\frac{\partial F_s}{\partial x} \geq \frac{\partial F_p}{\partial x} \qquad (2.5.2.11)$$

2.5.3 Levitation Phenomenon

This phenomena results in an additional displacement in the vertical direction (Z-direction) as the moving fingers are elevated away from the surface of the substrate. A successful electrostatic actuation of micromechanical structures requires a ground plane under the structure in order to shield it from the relatively large vertical field [33]. It has been observed that if the underlying substrate is not covered with a grounded polysilicon shield, the application of the dc bias voltage will cause the structure to be stuck down to the substrate. For this reason a heavily doped polysilicon film underlies the Comb structure. However, this ground plane contributes to an unbalanced electrostatic field distribution as illustrated by Figure 2.8 at page 27. The imbalance in the field distribution results in a net vertical force induced on the movable Comb fingers causing levitation of the structure away from the substrate. Several methods are reported to solve the problem of the dc levitation:

- Eliminating the ground plane and also removing the substrate beneath the structure to balance the field distribution.
- Placing a top ground-plane suspended above the Comb Drive achieves a balanced vertical force on the Comb. But both methods are very difficult to implement, as they require much more complicated fabrication processes.
- A Simpler solution is to modify the Comb Drive itself by reversing the polarity on alternating drive fingers, this result in a field distribution where the vertical electric fields are eliminated on the top surface of the movable finger and consequently the vertical levitation force is eliminated as shown in Figure 2.9 at page 27.

Figure 2.10 at page 28 shows another method for suppressing levitation. The Ground plane is modified such that underneath each Comb finger there is a strip of conductor biased at the same potential of its corresponding finger.

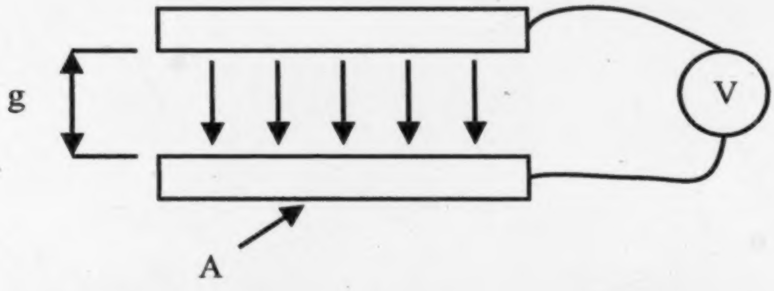

Figure 2.1: Schematic diagram of Parallel plate capacitor actuator

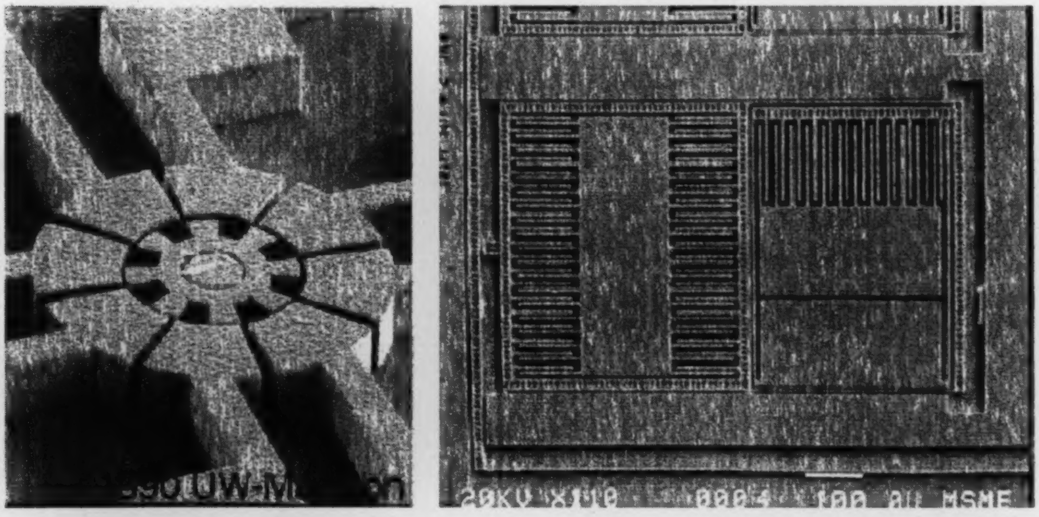
20KV X110 0004 100 μm MSME

(a) (b) Pister, UCB

Figure 2.2: (a) Rotary electrostatic micromotor (b) Silicon inchworm motor

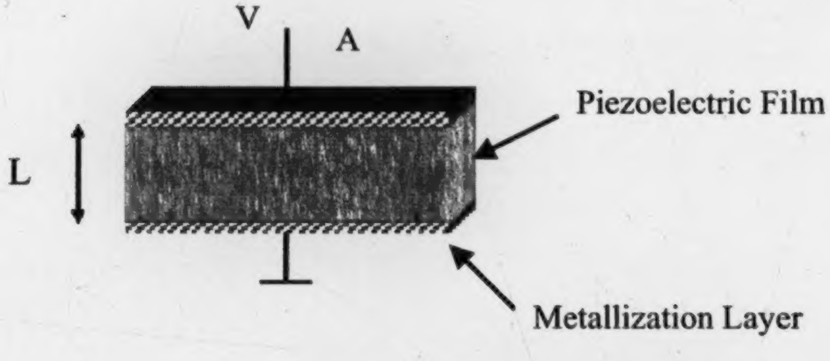
V
A
Piezoelectric Film
L
Metallization Layer

Figure 2.3: Thin film piezoelectric material

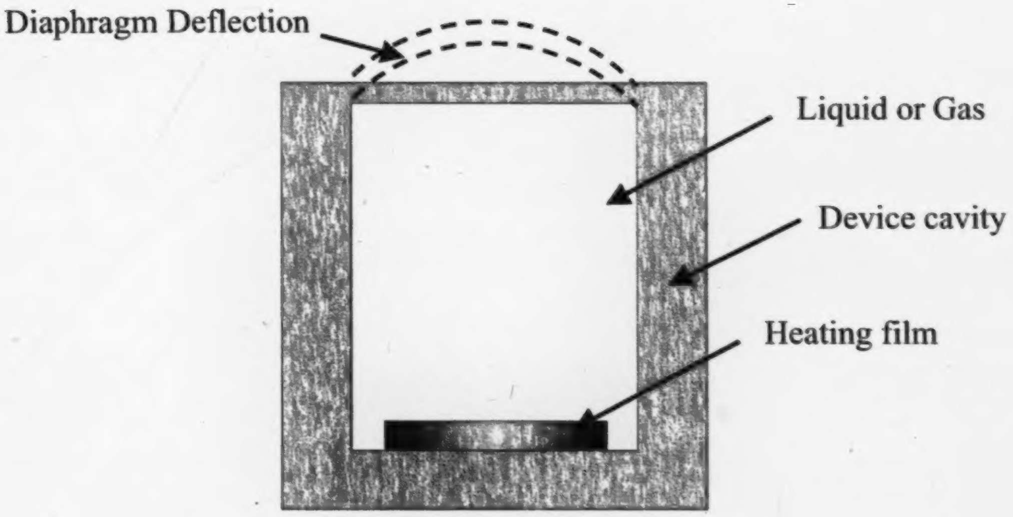
Diaphragm Deflection
Liquid or Gas
Device cavity
Heating film

Figure 2.4: Schematic diagram for thermal pneumatic microactuator

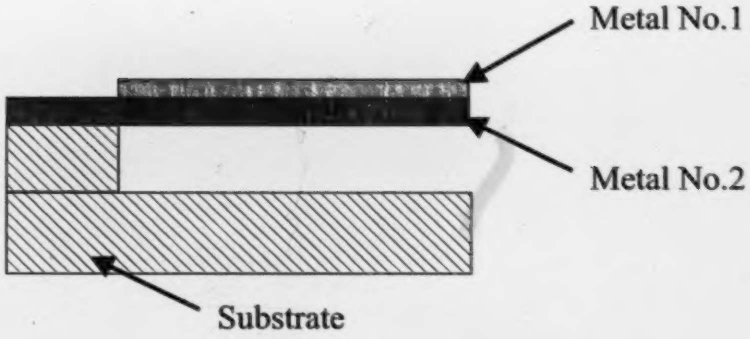
Metal No.1
Metal No.2
Substrate

Figure 2.5: Schematic diagram for Bimetallic microactuator

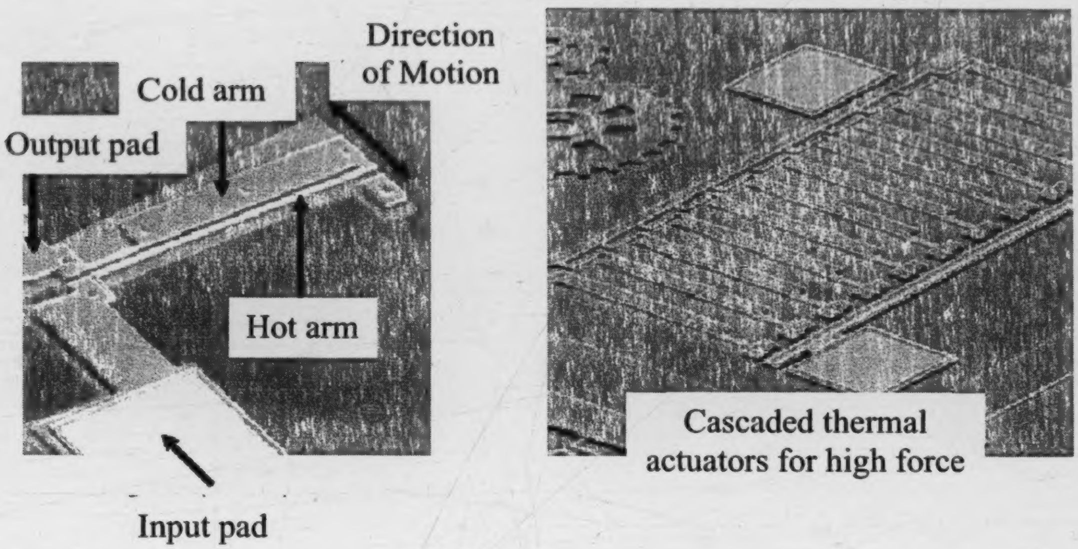
Direction of Motion
Cold arm
Output pad
Hot arm
Input pad
Cascaded thermal actuators for high force

Figure 2.6: Schematic diagram for array of thermal actuators

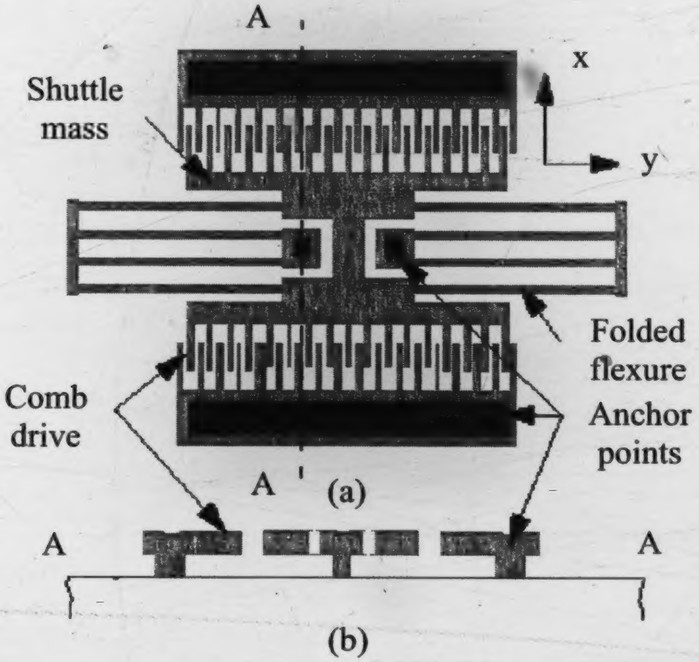
A
x
Shuttle mass
y
Folded flexure
Comb drive
Anchor points
A
(a)
A
A
(b)

Figure 2.7: Folded-flexure Comb Drive microactuator fabricated in the MUMPs process. (a) Layout. (b) Cross-section A-A

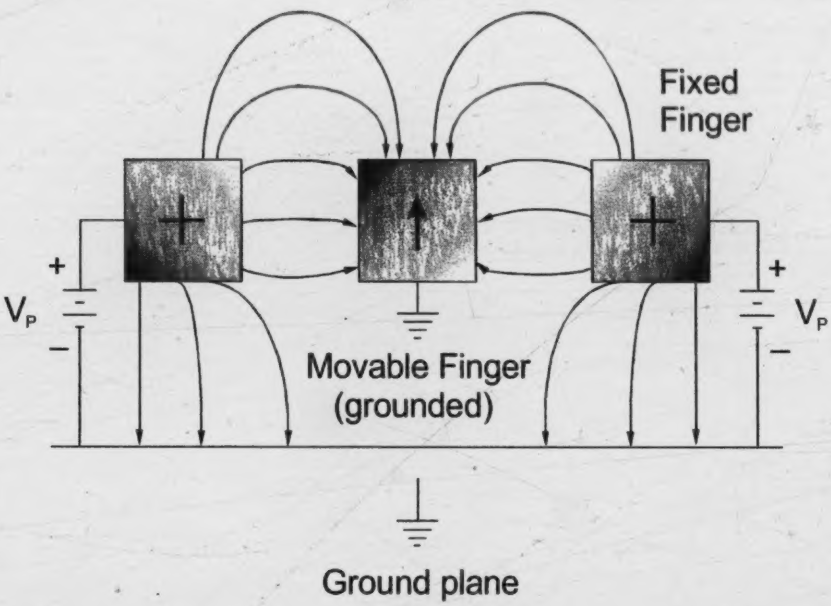
Fixed
Finger
+
V_P
−
+
V_P
−
Movable Finger
(grounded)
Ground plane

Figure 2.8: Comb finger under levitation force induced by two adjacent fingers biased at positive potential

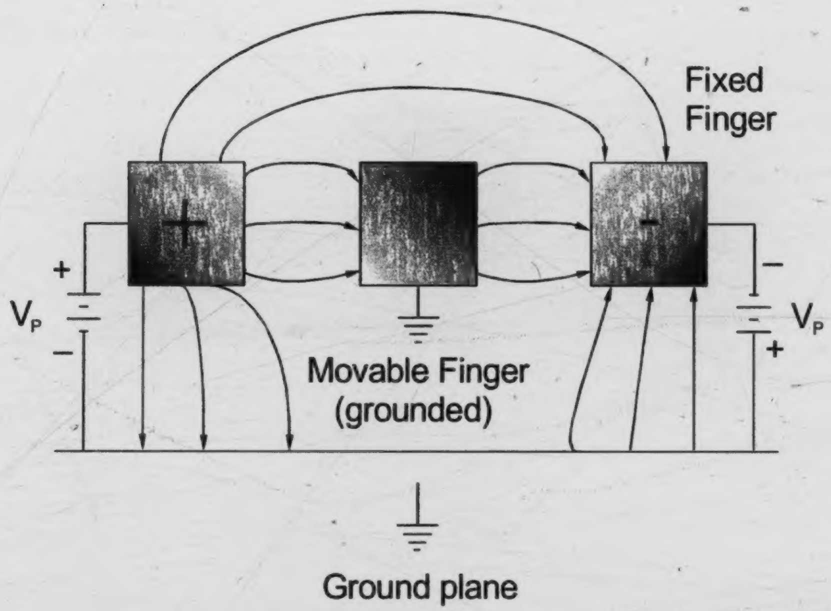
Fixed
Finger
+
V_P
−
−
V_P
+
Movable Finger
(grounded)
Ground plane

Figure 2.9: Comb finger when differential dc bias is applied to two adjacent fingers

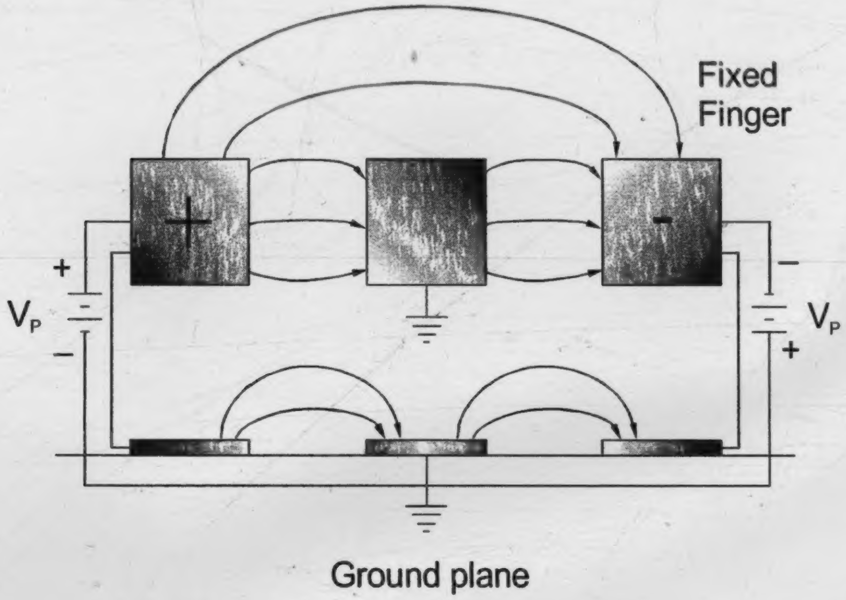
Fixed
Finger
+
-
+
V_P
-
-
V_P
+
Ground plane

Figure 2.10: Comb finger when differential dc bias is also applied to the striped ground conductors

Chapter 3

Reduced Order Modeling

3.1 Introduction

In this chapter, modeling of lateral electrostatic Comb Drive actuator is presented. A 2D FE model is developed using reduced order modeling (ROM) principles. This technique reduces the Comb Drive to a group of equivalent lumped parameters FE. These elements are assembled in an electromechanical circuit to capture the Comb Drive behavior. The concept of circuit simulation is explained through this chapter. Finally Simulation results are validated using an analytical model obtained from the literature and a good agreement between both results is achieved.

3.2 MEMS top-down design

Modeling and simulation for microelectromechanical systems MEMS is a technology area that is gaining in popularity. Due to the high interest in the commercial applications of MEMS related technology, the need for the proper simulation tools arises. The successful simulation tools are required to be capable of addressing coupled energy domains at the microscale level, which is a formidable task.

The design process for Microsystems can be classified as either a top-down [34] or a bottom-up approach as illustrated in Figure 3.1 at page 46. In the top-down approach, one first explores the system design space to determine critical system parameters. In this study, those parameters are the Comb Drive design parameters, which will be discussed later in this chapter. Once the critical system parameters have been established, more focus can be placed on examining implementation options and specific technologies through the use of reduced-order models.

Techniques associated with reduced-order modeling or subsystem level modeling are essentially the same as macro-modeling. The term reduced-order modeling is also referred to as subsystem modeling in some literature. Modeling at this level involves MEMS structure geometry in the form of lumped elements [35]. These elements would also include the power and control circuitry for the device. Reduced-order modeling allows the designer to determine what boundary and load conditions will be placed on individual components. The last level of modeling involves more detailed modeling analysis commonly referred to as three-dimensional simulation. This level of simulation allows the designer to examine a structure's response to a particular physical environment in great detail. This type of modeling is addressed in detail in chapter 4.

Reduced order modeling is used to represent static and dynamic behavior of MEMS devices to an acceptable level of fidelity and accuracy [36]. One of its major advantages is the ability to represent multiple mixed energy domains. It requires fewer components or fewer equations than the detailed system modeling; therefore using it gives the advantages of faster computation times and small storage requirements. This enables the effective simulation of large systems and reduces the design cycle time. Several studies reported in the literature showed the possibility of using Reduced order modeling to model MEMS devices. For example, a study by Hung et al. [37] showed that the reduced order model decreases simulation time by at least a factor of 37 with less than a margin of 2% error for a MEMS pressure sensor device. In addition, Guangya et al. [38] proposed a reduced-order model for the double-gimballed electrostatic torsional micromirror. This model permits extremely fast simulation while providing nearly FEM accuracy. The analysis results obtained by this reduced-order model are in good agreement with the finite element analysis results obtained from the commercial finite element package CoventorWare^{TM}. In the current study, the reduced-order modeling technique is used to simulate the lateral electrostatic Comb Drive actuator.

Microactuator structures such as Comb-Drive are used as transducing elements in a wide variety of MEMS structures. In general, Microactuators can be excited in several ways, including piezoelectric films, thermal expansion, magnetostatic forces and electrostatic forces. Accurate calculation of these electrostatic forces is an essential part of the design process of any microactuator. In Comb-Drives, the electrostatic force and the resulting Comb displacement can be controlled via changing the driving voltage. Recently, several studies have been carried out to obtain an efficient Comb-Drive design with high displacement and low driving voltage requirements [31]. Voltage controlled Comb-Drive actuators exert lateral electrostatic forces making them attractive for micropositioning applications, such as, xy-microstages [39], Micro mirrors used in the optical switches [40] and fluidic pump in on-a-chip drug delivery systems [41]. Comb Drive theory and electrostatic actuation techniques are explained in the following section.

3.3 Comb Drive Theory

The driving principle of electrostatic Comb-Drive actuator is based on electrostatic characteristics [28]. As shown in Figure 3.2 at page 46, when voltage is applied to the fixed electrode (or fingers) while the movable electrodes (or fingers) are potential grounded, a potential difference results across the electrodes and they become electrically charged. This action will induce a certain capacitance in the charged electrodes; Figure 3.3 at page 47 shows schematic details for this induced capacitance.

Where t is the finger thickness, b is the finger width, g is the gap between fingers, L is the overlap between fingers, and d is the distance between moving fingertip and the fixed finger anchor face. Thus, an electrostatic force is generated causing a displacement in the x direction. The total capacitance between the Comb Drive fingers and the driving force F created in the Comb can be expressed as:

$$U = \frac{1}{2} C V^2 \tag{3.3.1}$$

$$C = \frac{2 n t \epsilon_o \epsilon_r (L + x)}{g} + [n C_p] \tag{3.3.2}$$

$$F = \frac{\partial U}{\partial x} = \frac{1}{2} \frac{\partial C}{\partial x} V^2 = \frac{n t \epsilon_o \epsilon_r V^2}{g} \tag{3.3.3}$$

Where U is the energy associated with the applied electric potential V, ϵ_r is the relative permittivity of the dielectric material between the two fingers, ϵ_o is the permittivity in the free space and equal to 8.85 pF/m, n is the number of the pairs of fingers, C is the total capacitance of the Comb Drive fingers, C_p is the parasitic capacitance. The parasitic capacitance can be approximated to zero which yields the above equations [42].

If the movable electrode is displaced following Hooke's law, the reaction force F_S induced in the suspension beam holding the movable electrodes (or fingers), which represents a spring suspension system, will be related to the stiffness of the beam and the displacement and can be calculated from the following equation:

$$F_S = K_x x \tag{3.3.4}$$

Where, K_x is the spring stiffness in the x-direction (i.e. actuation direction) and x is the displacement. The suspension beams must be flexible enough in the direction of actuation, increasing the beam stiffness will require larger electrostatic force to cause the deflection and consequently requires a higher driving voltage. Equations used to drive the spring stiffness are shown in Jaecklin et al. [31] and Rob et al. [23]. Furthermore, a suspension that is compliant in the direction of displacement and stiff in the orthogonal directions is required to achieve high displacement with lower driving voltage and can avoid many unfavorable operation problems. Therefore, different types of spring design have been applied in Comb-Drive actuators. Some of these designs include clamped-clamped beams, crab-leg flexure, and folded-beam flexure. Rob et al. [23] explain those designs in details. In equilibrium position, the forces F_S and F have to be equal, where the displacement x can then be expressed as a function of the driving voltage (V), the gap (g), the thickness (t), the number of electrodes (n) and the stiffness (K_x) as:

$$x = \frac{n t \in_o \in_r V^2}{g K_x} \tag{3.3.5}$$

Equation (3.3.5) shows that the relation between the actuator displacement and the applied driving voltage is not quite linear and as the applied voltage increases the displacement increases, normally this relation is known as the voltage-stroke relation of the Comb-Drive. The achievement of a smart design of the Comb-Drive, i.e. large displacement at low driving voltage, is an essential requirement that needs to be fulfilled.

Equations (3.3.1) to (3.3.5) summarize the design parameters of the Comb-Drive. These parameters are (i) the spring design and stiffness K_x, (ii) the driving voltage V, (iii) the electrode's gap g, (iv) initial overlap L, (v) number of fingers n, and (vi) thickness of finger t. Table 3.1 at page 47 shows the values of those parameters. Although the term L does not appear in equation (3.3.3) or (3.3.5), the Comb Drive performance in terms of displacement and generated electrostatic force are investigated as a function of it. The term L is used to calculate the distance between the two fingers facing each other (d). This distance represents the gap between a two plates when considering the two fingers as a two parallel plates capacitor. This concept is used in the definition of the initial gap between the two plates of the electromechanical transducer element (TRANS126) that will be used later to represent the Comb Drive. The following sections represent the concepts of reduced order modeling and their implementation in the commercial FE package ANSYS^{TM}.

3.4 Reduced order modeling (ROM)

To calculate the driving forces and displacements of different Comb-Drive designs, a robust FE model has been constructed and solved within the Multiphysics environment in the commercial FE package ANSYS [43, 44]. The construction of this model is automated to account for the variation of all the design parameters discussed in the previous section. To solve this Multiphysics interaction problem, a direct FE coupled-field analysis was applied [45] .

Full dynamic FE simulation of coupled electrostatic structural problems is prohibitively expensive for complex models. It requires powerful computational hardware and huge simulation process time. Therefore, it is necessary to simplify the Multiphysics modeling and provide accurate, high fidelity harmonic and time-domain solutions in a fast and efficient manner. This simplification is applied in the current work using the Reduced Order Modeling technique (ROM) [46, 47], which consists of using equivalent lumped parameters elements (springs, masses, dampers, electromechanical transducers, capacitors, inductors, resistors, etc.) and substructuring of large linear systems. A complete reduced order model can be constructed using the electromechanical circuit builder [48], which simulate the entire system through an electromechanical circuit. This circuit combines both of the mechanical and electrical components of the system. It represents these components by equivalent lumped parameter elements. Those lumped parameter elements are used to capture the device behavior and its characteristics. Substructuring is used to calculate the effective stiffness of the system. Another analysis commonly known as modal analysis is used to calculate the effective mass of the system (moving Comb mass and the mass of folded flexure beams). A detail description of the lumped parameter elements characteristics, their implementation in the FE modeling of the Comb Drive actuator, Substructuring methodology, and circuit builder are described in the following sections.

3.4.1 Electromechanical Transducer (TRANS126)

The central element of many MEMS devices is a Comb Drive structure. It is essentially a capacitor with variable geometry. The capacitor plates can deform and move relative to each other due to electrostatic, inertia or mechanical forces, resulting in a measurable capacitance change. This change transduces electrical energy into mechanical energy. By applying a specific voltage to the plates, the gap between the plates can be controlled.

Therefore, in order to capture this transduction process into an element that is equivalent to the Comb Drive, an electromechanical transducer element is required. This step will reduce the Comb Drive to an element in a circuit. This element must be able to convert the electrical energy into mechanical energy and vise versa. Also, it must be able to store the change in the capacitance due to mechanical deformation. To achieve this goal, (TRANS126) is used. TRANS126 is a "reduced-order" Electromechanical transducer element that is capable of full coupling between electrical energy and mechanical energy. Coupling between electrostatic forces and mechanical forces can be characterized by mapping the capacitance of the system (capacitance between Comb Drive fingers) as a function of the motion of the device (range of device displacements). The transducer element converts electrostatic energy to mechanical energy and vice versa as well as store electrostatic energy, thus completely modeling the coupled field system.

TRANS126 [49], is a lumped element with voltage and structural degrees of freedoms (DOFs) as cross variables and current and force as through variables. Input for the element consists of a capacitance-stroke relationship that can be derived from electrostatic field solutions. Figure 3.4 at page 47 shows a schematic of the TRANS126 element. TRANS126 is a 2 noded element each node has structural (UX, UY or UZ) and electrical (VOLT) DOFs. The variable (GAP) represents the initial gap between the conducting walls of the electromechanical device. In the current study, two facing fingers of the Comb Drive are representing the plates of a parallel plate capacitor. The two nodes of the element represent the plates. Normally node (I) is fixed, which represents the fixed part of the Comb Drive fingers and node (J) is movable, which represents the movable part of the Comb Drive fingers. Comb Drive generated displacement is represented by the element displacement (stroke) between its nodes.

3.4.2 Capacitance Extraction (CMATRIX)

In order to construct the electromechanical transducer element, the capacitance-stroke relationship has to be computed. This relationship is derived from the change of both self-capacitance and mutual capacitance between conductors (Comb Drive fingers) and the Comb displacement (stroke). To calculate the capacitance between the Comb fingers, a 3D electrostatic analysis has to be performed. This analysis has to be made in a parametric manner so that it can accommodate for different designs of the Comb Drive. This type of analysis requires definition of two FE domains. The first is the structural domain including conductors (Comb Drive fingers) and the second is the electrostatic domain, which is the surrounding dielectric material (air).

To do that, a FE code has to be written to extract a one-tooth symmetry model of the Comb Drive. Then, a large "air" volume should be extruded around the tooth model. After subtracting the tooth model from the air volume using a Boolean operation, the resultant volume of air is the electrostatic "domain" which is meshed with electrostatic elements. Conductors (Comb Drive Fingers) are assumed to be perfect conductors and hence do not require a FE mesh within the conductor domain. Only the surrounding dielectric regions and air regions require a mesh. Figure 3.5 at page 48 shows the meshed model that is used to extract capacitance showing the meshed "air" domain. The whole process is automated in a command macro known as (CMATRIX) [50], available in the commercial FE package ANSYS. It is used to extract the lumped capacitance values of the system. This macro groups the surface nodes of the required conductors into node components. The command macro will then use the components to systematically compute a series of simulations and extract the capacitance. By running a series of electrostatic simulations for different strokes, or deflections a complete characterization of system capacitance is achieved. The system capacitance as a function of the device stroke is computed and these data is used as input to the transducer element. Only uniaxial motion is considered at the resonator to calculate the change in the capacitance against the stroke. Figure 3.6 at page 49 shows a flow chart for the system capacitance extraction procedure.

3.4.3 Lumped parameter elements

Complete characterization of MEMS devices in terms of lumped parameter is required to establish a successful reduced order model (ROM). On the mechanical side of the device, this would include spring, mass, damper. On the electrical side, it might include circuit elements such as resistors, capacitors, inductors, and voltage sources, as well as current sources. For example, an electrostatic Comb Drive can be reduced to one or more electromechanical transducer elements and the mechanical structure to equivalent springs dampers, and equivalent mass. In order to extract the effective stiffness, damping ratio, and effective mass of the mechanical system, these main analysis steps have to be performed.

First, a static structural analysis associated with the substructure generation solver is used. In this analysis, a master node is defined at the center of the model with a DOF in the direction of excitation and a static load applied in the direction of excitation. The stiffness matrix of the system is computed and the effective stiffness of the suspension system is then obtained from these results. This effective stiffness is used as an input to the spring element.

Second, a Modal Analysis is performed to extract the effective mass of the movable Comb-Drive. For most MEMS devices, there is a dominant response mode of vibration. This mode can be identified from the modal analysis by examining the largest value of the participation factor in the direction of excitation. This factor is a measure of how much a mode is contributing to the deflections in the direction of excitation; and the mass associated with it represents the effective mass at that mode in the excitation direction, which can be obtained easily from the analysis results. The extracted mass value represents the system mass in the form of the mass element.

Third, the damping factor is preset to correspond to a quality factor (Q) of 100, which is often associated with Comb drives packed in atmospheric air pressure [51]. The quality factor is used to calculate the damping ratio of the system; this damping ratio is an input to the damper element, which is used in circuit simulations. To include the damping effect in the analysis of the Comb Drive, an assumption of packing in the atmospheric air pressure is used. Assuming operating at a low frequency, a linear velocity profile for the damping fluid is established [52]. Thus, the approach of Couette flow between the Comb fingers is the dominant energy dissipation mechanism. The damping ratio ζ can be calculated from the following equations [53].

$$\zeta = \frac{\sqrt{MK_x}}{Q} \tag{3.4.3.6}$$

$$K_x = 2Eh(W/L_s)^3 \tag{3.4.3.7}$$

Where K_x is the spring stiffness of the folded beam flexure structure in the x-direction, M is the mass of the structure, E is Young's modulus, W is the beam width, h is the beam thickness, and L_S is the length of the beam of the folded beam flexure structure (spring structure). Elements (COMBIN14), (COMBIN39), and (MASS21) are used in ANSYS to represent the spring stiffness, damping, and system mass respectively.

3.4.4 Circuit Simulation

The previous sections defined the required procedure to reduce the Comb drive into several equivalent elements. These elements have to be connected to each other in one circuit to fully model the Comb Drive. To do that, Circuit simulator has to be used. Circuit simulator is a tool that is used to build a circuit that combines the mechanical elements, transducer elements, and electrical elements. The circuit simulator provides a convenient method to create a lumped model of a coupled system to represent the MEMS devices. Figure 3.7 at page 50 shows a circuit representing the Comb Drive actuator using the circuit simulation building capabilities.

The analysis procedure of the Comb-Drive actuator starts with modeling the Comb Drive several times with different geometries. In all analyzed cases, the Comb-Drive is replaced with the TRANS126 transducer. This single transducer is then used for the drive and pick-up Combs. The transducer elements are attached to the spring element, mass element, and damper element where those lumped parameter elements capture the characteristic behavior of the global 3-D finite element model. In this circuit the input to the transducer element will be the excitation voltage at node no.3 and the output will be the structural DOF of the element end in the actuation direction at node no.2.

Voltage can be applied directly to the node of the transducer element or through the use of a general electric circuit element (CIRCU124), which is one of the lumped elements used to simulate the electrical systems. Element CIRCU124 includes sub-models of resistors, capacitors, inductors, current and voltage sources. The displacement in the movable Comb fingers is measured from the structural DOF of the element end in the actuation direction as the electrostatic energy is converted into mechanical energy via the transducer element.

3.5 Results and Discussion

In the current study, Direct Coupled-Field FE Analysis is applied to the robust electrostatic Comb-Drive model discussed earlier using the Reduced Order Model (ROM) principles. The effects of these Comb Drive design parameters on the actuation performance are explored through a parametric study. Figure 3.8 at page 50 shows a comparison between the simulation results and the analytical results of comb drive. The simulation for the displacement response is in good agreement with analytical method over a typical range of operational voltage. The error of the maximum displacement between both results is less than 5%. This proves, that the reduced order modeling technique is a reliable and accurate numerical method that can be used effectively to predict the response of the Microelectromechanical Systems (MEMS) [54, 55].

Figures 3.9 and 3.10 at page 51 show the variation of the Comb Drive displacement and generated electrostatic force with the number of fingers at a driving voltage of 40 volts. In these figures, the calculated Comb Drive displacement and generated electrostatic force are shown to be linearly proportional to the number of Comb Drive fingers. For constant operating voltage, Equation (3.3.3) shows that the electrostatic force should also vary linearly with the number of fingers in the studied Comb-Drive, for the same finger thickness and gap. In addition, when the driving voltage is increased, the Comb Drive displacement is shown in Figure 3.11 at page 52 is nonlinearly increased for a Comb Drive design that has 20 fingers. In this figure, the displacement rate of variation is shown to increase with the driving voltage. This is also valid for Figure 3.12 at page 52 where the variation of the electrostatic force is shown.

The results in Figure 3.13 at page 53 indicate that for a driving voltage of 45 volts, as the gap (g) between the Comb Drive finger decreases, the induced capacitance nonlinearly increases and so does the induced Comb displacement. The effect of the gap on the system's capacitance can be explained by Equation (3.3.2). This effect of the Comb Drive gap on the displacement is also expected based on Equation (3.3.5). In this case, the displacement variation rate is shown to decrease with the increase of the gap (g). This effect is also illustrated in Figure 3.14 at page 53 for the electrostatic force. On the other hand, an increase in the value of the overlap distance (L) is shown to increase the Comb Drive displacement. This non-linear proportional relation between the Comb Drive displacement and the offset or overlap distance (L) is shown in Figure 3.15 at page 54 for a driving voltage of 40 volts and a comb gap (g) of 2 μm as it is shown also for the electrostatic force as indicated in Figure 3.16 at page 54. In addition, the effect of the Comb Drive finger thickness on its displacement value is shown in Figure 3.17 at page 55. In this case, the finger thickness (t) is varied between 1, 2 or 3 μm. The driving voltage is then increased and the displacement is calculated. Figure 3.17 shows the increase in the Comb Drive displacement is nonlinearly proportional with the increase in the finger thickness, where the rate of displacement variation decreases for higher finger thickness. This effect on the electrostatic force is also seen at Figure 3.18 at page 55. Finally, Figure 3.19 at page 56 shows the displacement variation with the driving voltage at different spring designs. As the Comb-Drive folded-flexure length increases the spring stiffness in the actuation direction decreases, which increase the displacement of the Comb Drive. Therefore, increasing the length of the folded-flexure beams is desirable to increase the Comb Drive displacement. This effect on the electrostatic force is also seen at Figure 3.20 at page 56. Taking into perspective all the above results, the overall system stiffness is calculated by dividing the comb driving forces over its displacement in each case. Figure 3.22 at page 57 shows that the dominant parameter that affects the system total stiffness is the folded flexure spring length (Ls). The effect is investigated further in Figure 3.21 at page 57, which shows that the overall system stiffness decreases at a nonlinear rate with the increase of the folded flexure spring length (Ls).

To facilitate the use of the current study results in optimizing the design of linear comb drives, an effort is made here to condense these results into a compact non-dimensional form that correlates the studied geometric parameters of the modeled comb drive with its displacement. Using the method of least squares, it is found that the displacement values presented in Figures 3.9, 3.13, 3.15, 3.17, and 3.19 are well described by the following equations:

$$Displacement = \sum_{n=0}^{4}\sum_{m=0}^{4} A_{nm}(V)^{n}(n)^{m} \tag{3.5.8}$$

$$Displacement = \sum_{n=0}^{4}\sum_{m=0}^{4} A_{nm}(V)^{n}(g)^{m} \tag{3.5.9}$$

$$Displacement = \sum_{n=0}^{4}\sum_{m=0}^{4} A_{nm}(V)^{n}(L)^{m} \tag{3.5.10}$$

$$Displacement = \sum_{n=0}^{4}\sum_{m=0}^{4} A_{nm}(V)^{n}(t)^{m} \qquad (3.5.11)$$

$$Displacement = \sum_{n=0}^{4}\sum_{m=0}^{4} A_{nm}(V)^{n}(K_X)^{m} \qquad (3.5.12)$$

Where, the values of A_{nm} for the parameters, n, g, L, t and K_X are presented in Table 3.2 at page 58. Equations (3.5.8-12) are in good agreement with the present FE results, to within less than 6 percent deviation.

3.6 Conclusion

During the course of this work, Reduced Order Modeling (ROM) principles were used to create a two-dimensional FE model of lateral electrostatic comb drive actuators. The effect of the design parameters of lateral Electrostatic Comb Drive actuators on the actuation performance was explored through a parametric study. In this model, the thickness, gap and overlap between the Comb fingers were varied. The design of this model was also modulated to account for the change in the number of Comb fingers and the applied driving voltage. The analytical model available from literature validated numerical simulation results. Good agreement with the analytical method over a typical range of operational voltage has been achieved. The error of the maximum displacement between both results is less than 5%. The Reduced Order Modeling technique proved to be an accurate and reliable method to simulate lateral electrostatic Comb Drive actuators. However, this technique has a few drawbacks. For example, it gives the Comb response in terms of displacement in only one major actuation direction. In addition to that it is not possible to calculate the maximum stresses developed in the system as the system is represented by lumped elements not a real finite element domain. Also, this model is not capable of predicting the out of plane displacement described earlier in chapter two. This undesirable displacement is not favorable in applications like micromirrors actuation. To overcome these limitations, 3D FE model is developed in chapter four.

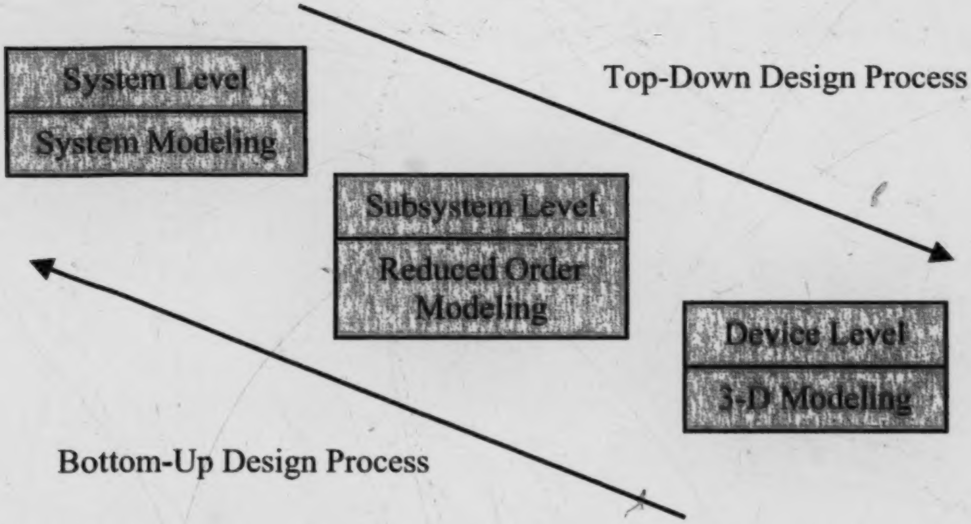
System Level
System Modeling
Top-Down Design Process
Subsystem Level
Reduced Order Modeling
Device Level
3-D Modeling
Bottom-Up Design Process

Figure 3.1: Design processes for MEMS with the various levels of design and typical modelling approach used at each level.

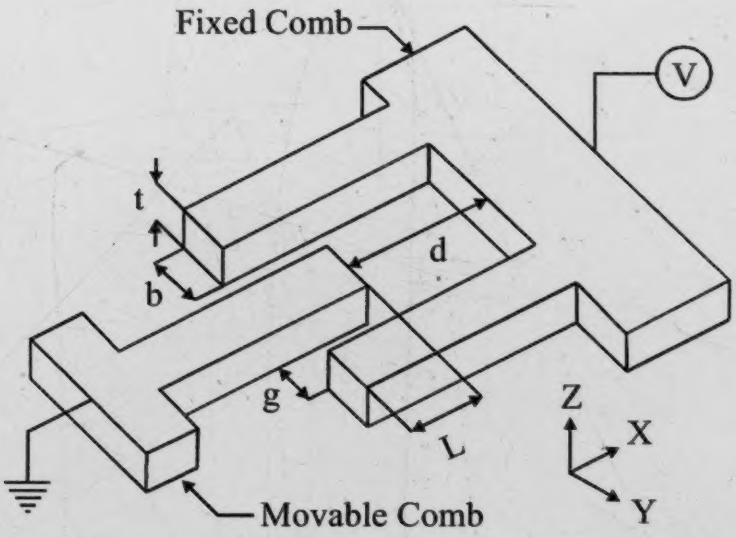
Fixed Comb
V
t
b
d
g
L
Z
X
Y
Movable Comb

Figure 3.2: Schematic details for one movable finger between two fixed fingers.

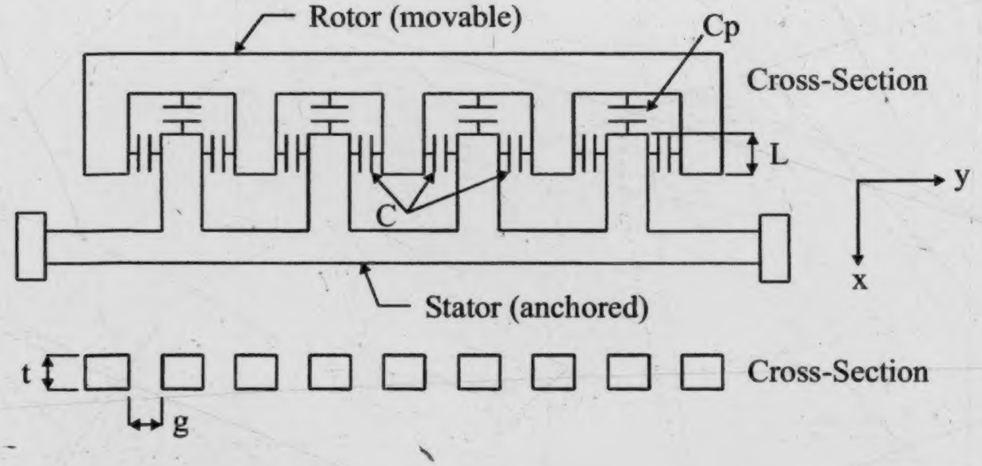
Rotor (movable)
Cp
Cross-Section
L
y
x
C
Stator (anchored)
t
Cross-Section
g

Figure 3.3: Schematic details for the mutual capacitance between Comb fingers

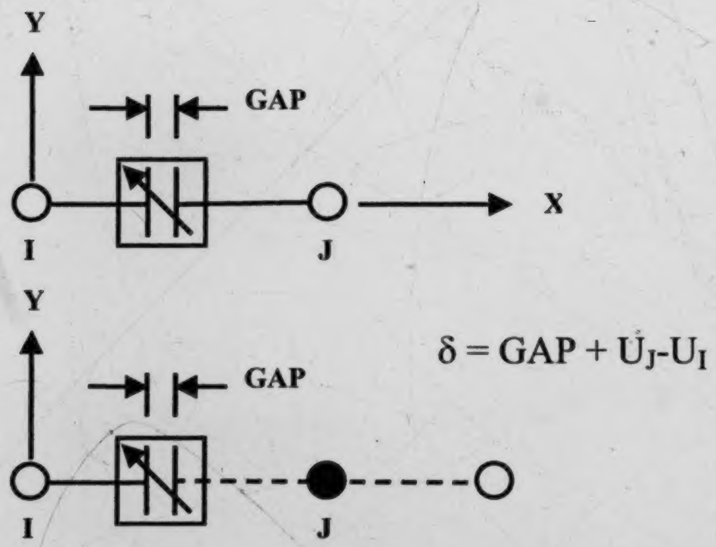
Y
GAP
X
I
J
Y
GAP
δ = GAP + U_J-U_I
I
J

Figure 3.4: Schematic for the electromechanical transducer element (TRANS126)

Table 3.1: Design parameters for Comb Drive Actuator

Design Parameter	Value range
Number of Comb Fingers (n)	10 ~ 30
Finger thickness (t)	1.0 ~ 3.0 μm
Gap between Comb Fingers (g)	1.0 ~ 6.0 μm
Folded flexure spring length (Ls)	75 ~ 325 μm
DC driving Voltage (V)	0 ~ 50 Volts
Overlap between Fingers (L)	3 ~ 10 μm

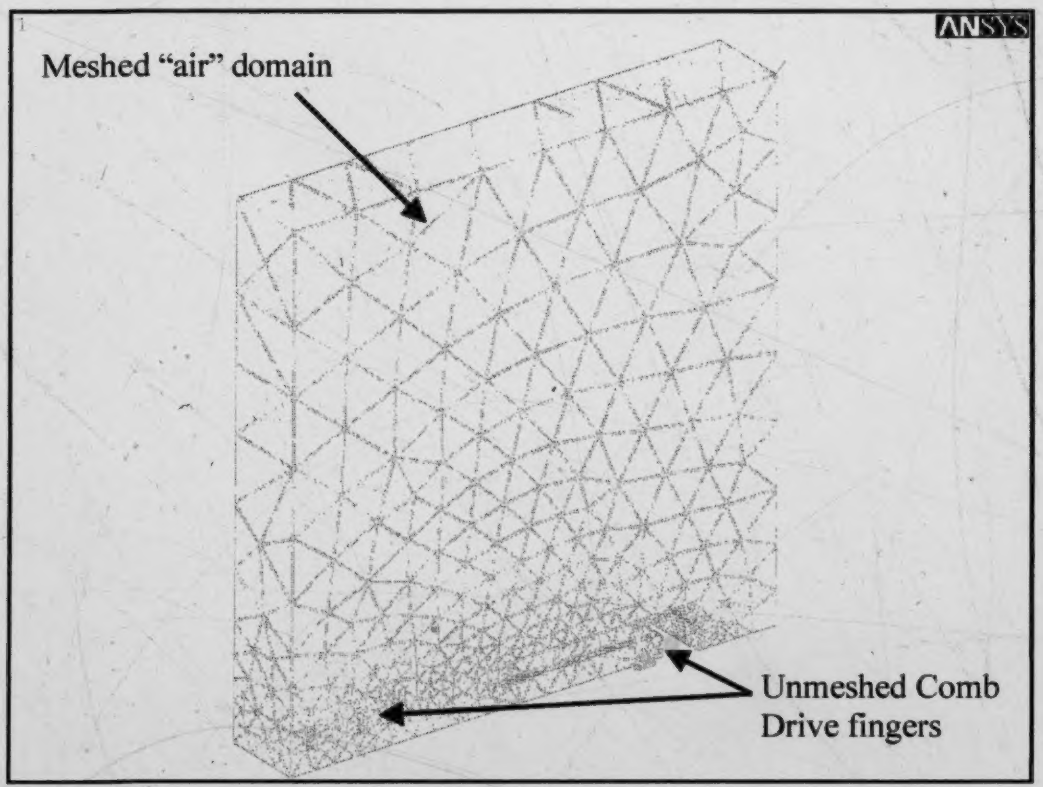
1
ANSYS
Meshed "air" domain
Unmeshed Comb Drive fingers

Figure 3.5: Finite element mesh-only air domain shown

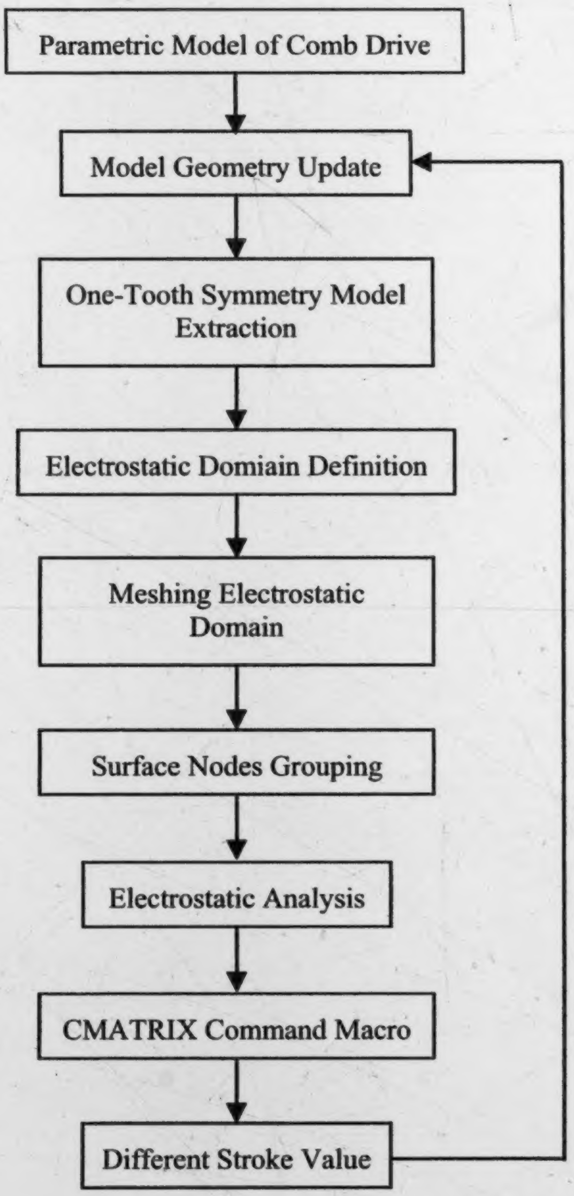
Parametric Model of Comb Drive
Model Geometry Update
One-Tooth Symmetry Model Extraction
Electrostatic Domiain Definition
Meshing Electrostatic Domain
Surface Nodes Grouping
Electrostatic Analysis
CMATRIX Command Macro
Different Stroke Value

Figure 3.6: System Capacitance Extraction Procedure

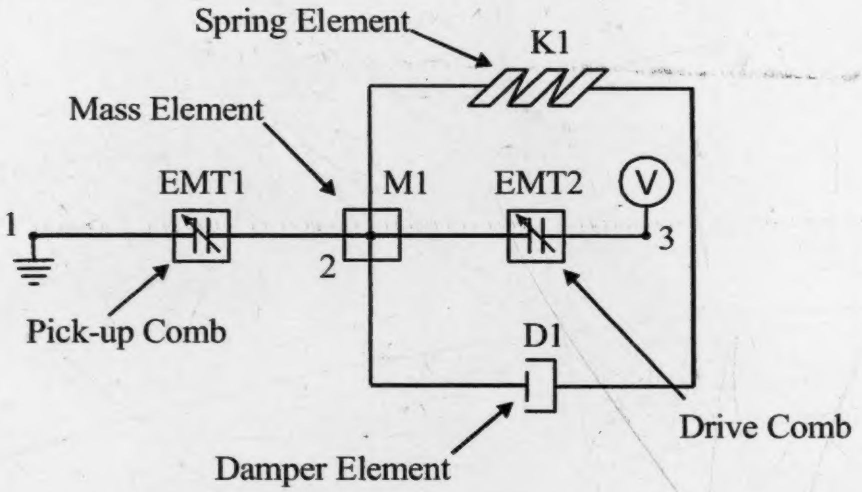
Spring Element
K1
Mass Element
EMT1
M1
EMT2
V
1
2
3
Pick-up Comb
D1
Drive Comb
Damper Element

Figure 3.7: Reduced Order Model (ROM) for Comb Drive actuator

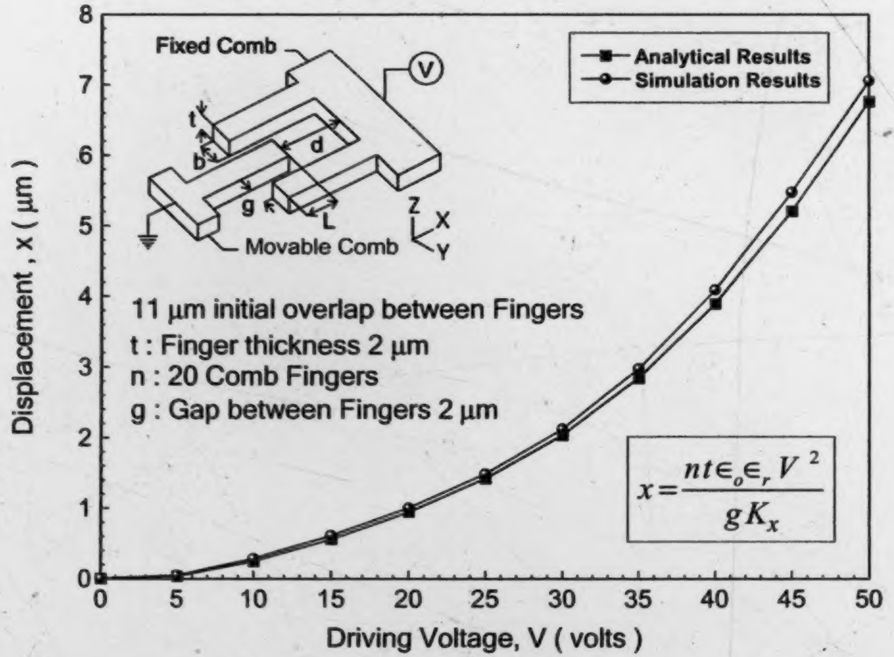

Figure 3.8: The variation of Comb Drive displacement vs. the applied driving voltage, (V): Comparison between analytical and simulation results

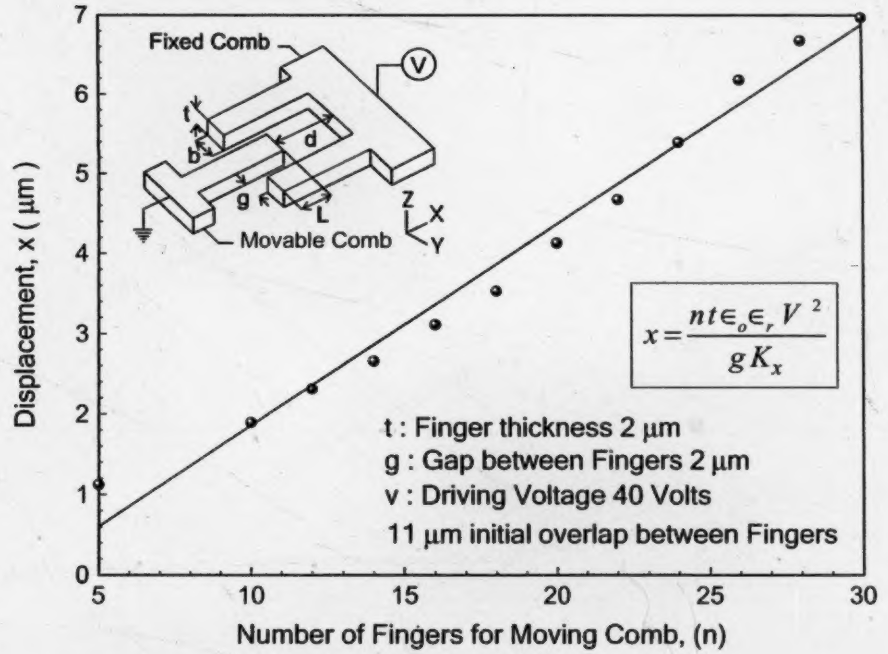

Figure 3.9: The variation of the Comb Drive displacement vs. the number of moving fingers, (n)

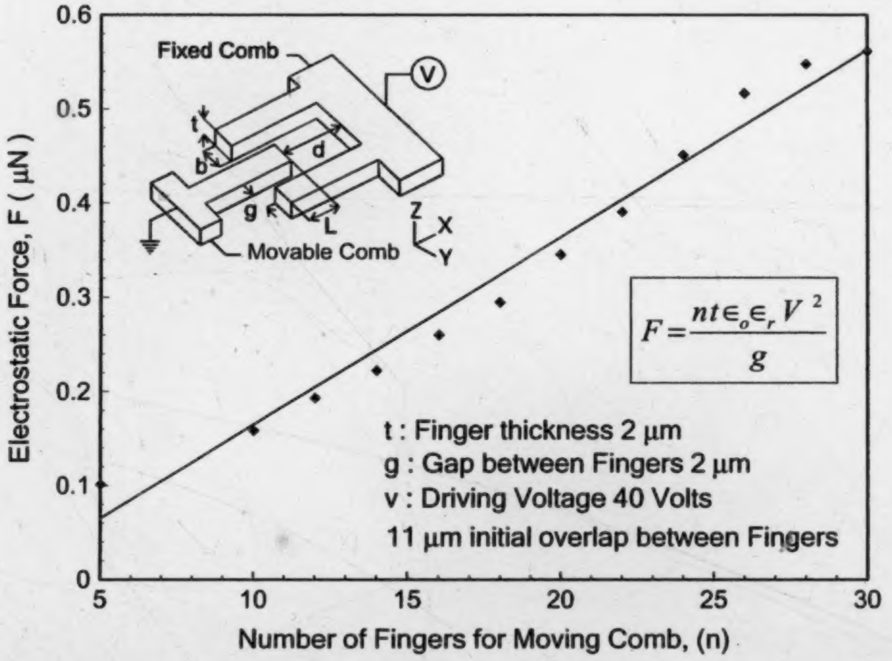

Figure 3.10: The variation of the Comb Drive electrostatic force vs. the number of moving fingers, (n)

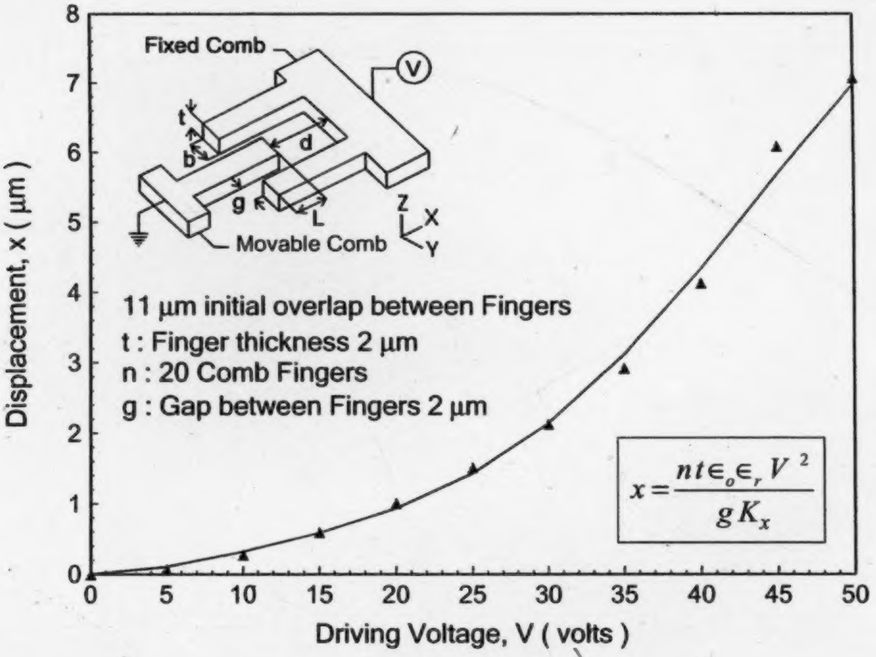

Figure 3.11: The variation of Comb Drive displacement vs. the applied driving voltage, (V)

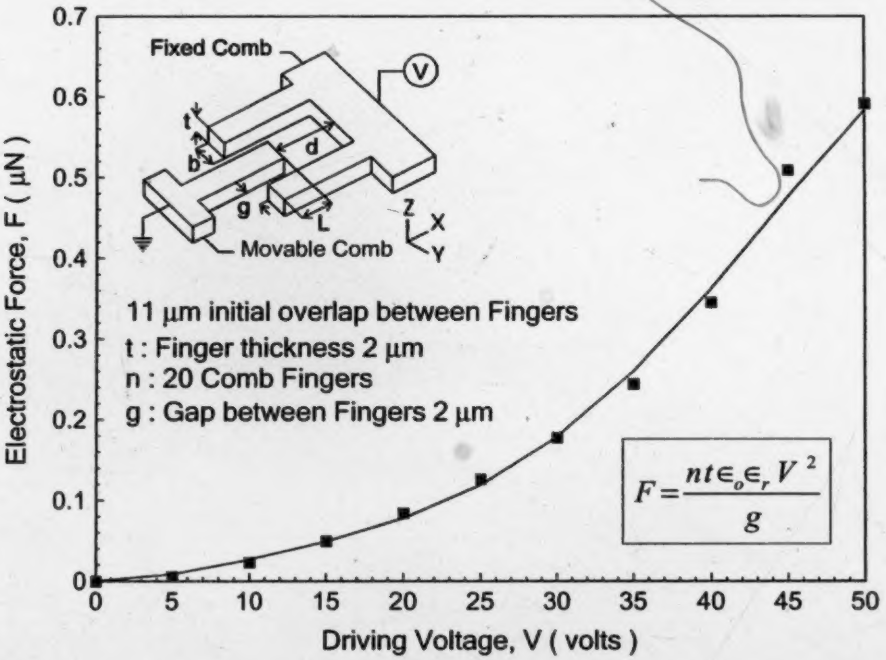

Figure 3.12: The variation of Comb Drive electrostatic force vs. the applied driving voltage, (V)

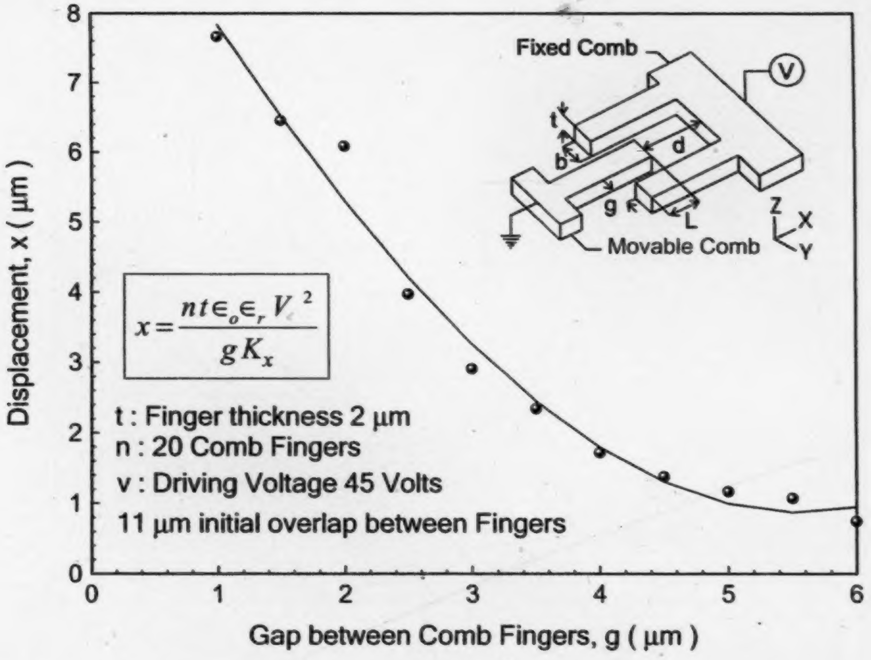

Figure 3.13: The variation of the Comb Drive displacement vs. the gap between Comb fingers, (g)

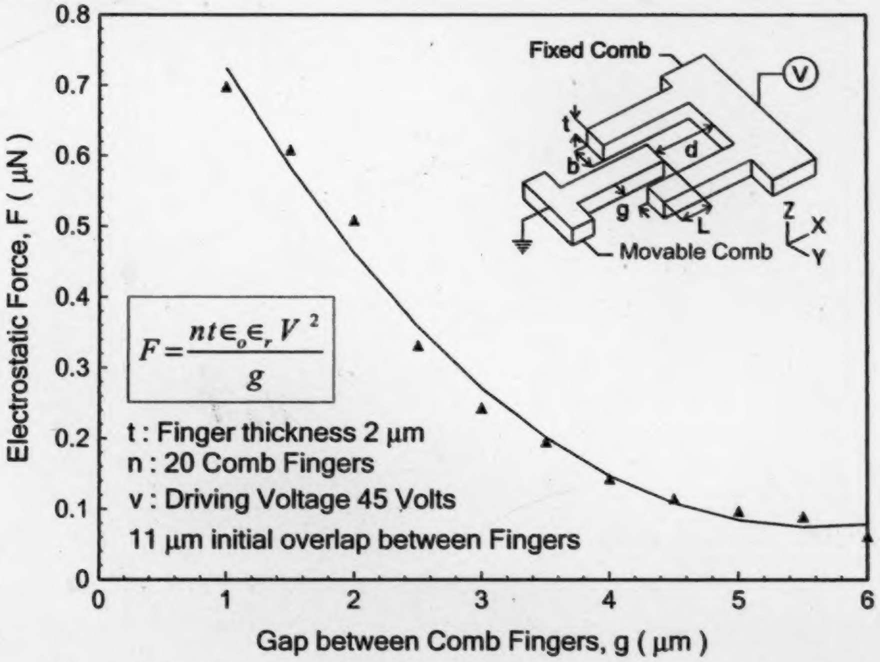

Figure 3.14: The variation of the Comb Drive electrostatic force vs. the gap between Comb fingers, (g)

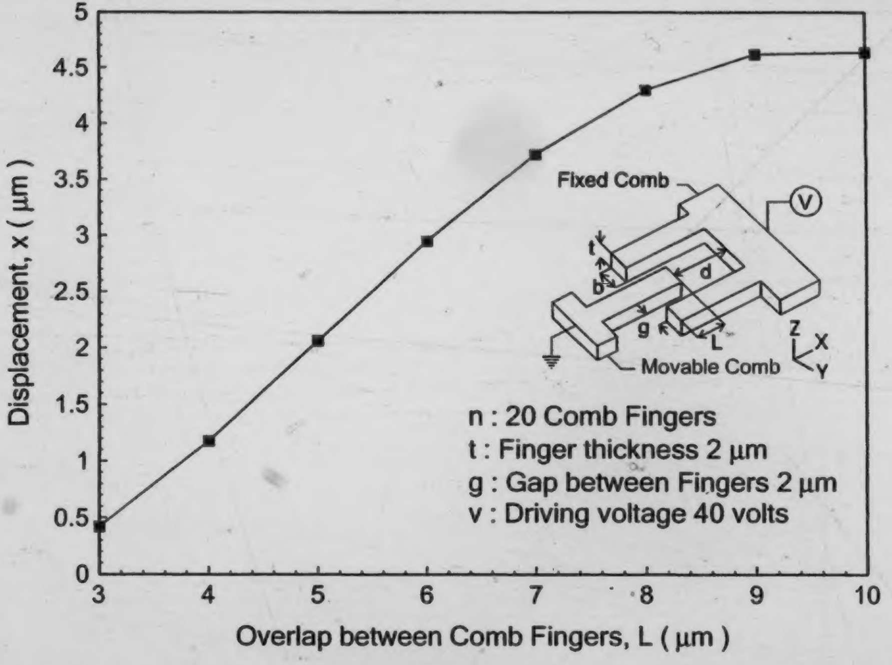

Figure 3.15: The variation of the Comb-Drive displacement vs. the overlap distance (L) between the Comb Fingers

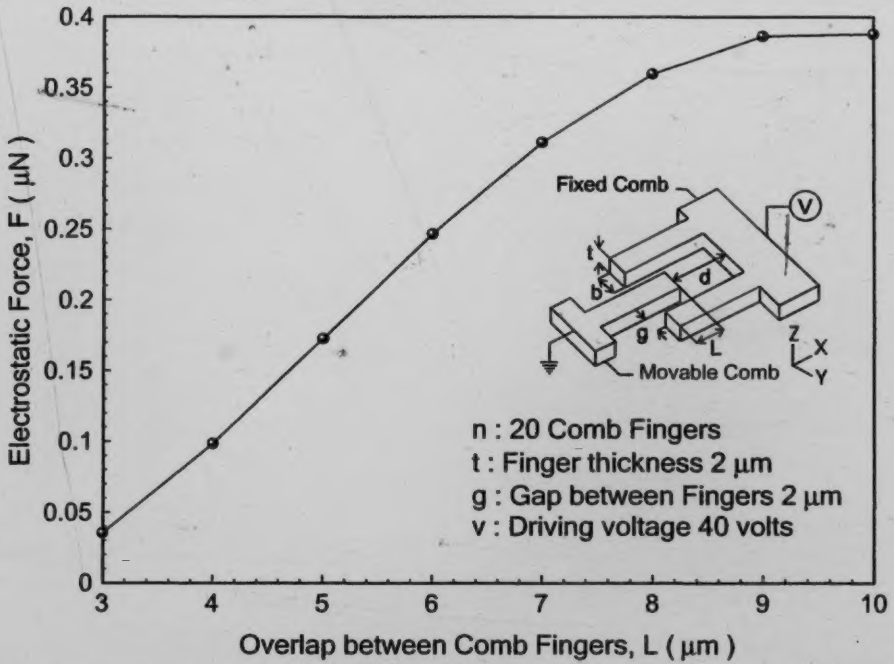

Figure 3.16: The variation of the Comb-Drive electrostatic force vs. the overlap distance (L) between the Comb Fingers

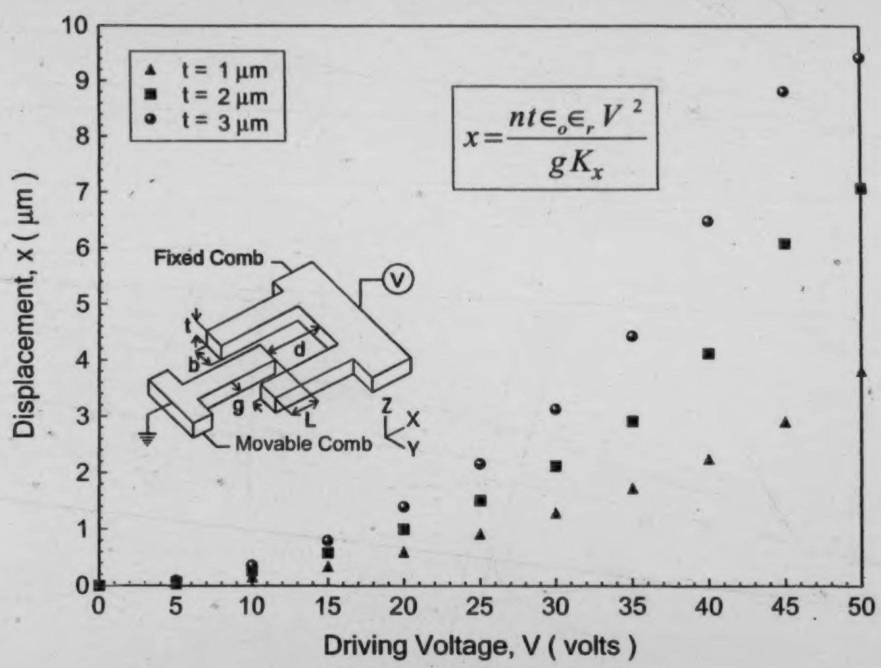

Figure 3.17: The variation of the Comb Drive displacement vs. the driving voltage at different finger thickness, with n = 20 fingers, g = 2 µm, L = 11 µm and b = 2 µm

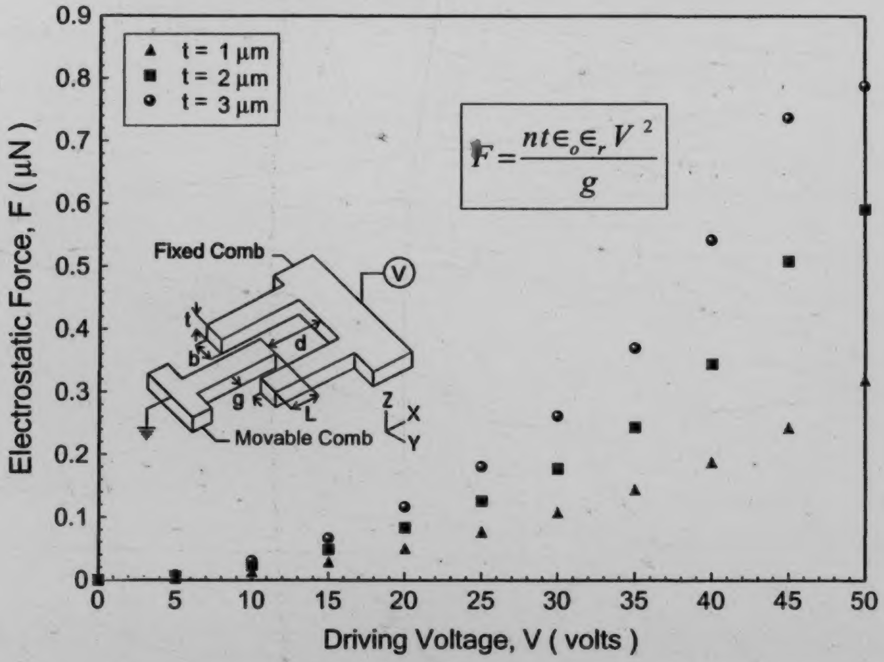

Figure 3.18: The variation of the Comb Drive electrostatic force vs. the driving voltage at different finger thickness, with n = 20 fingers, g = 2 µm, L = 11 µm and b = 2 µm

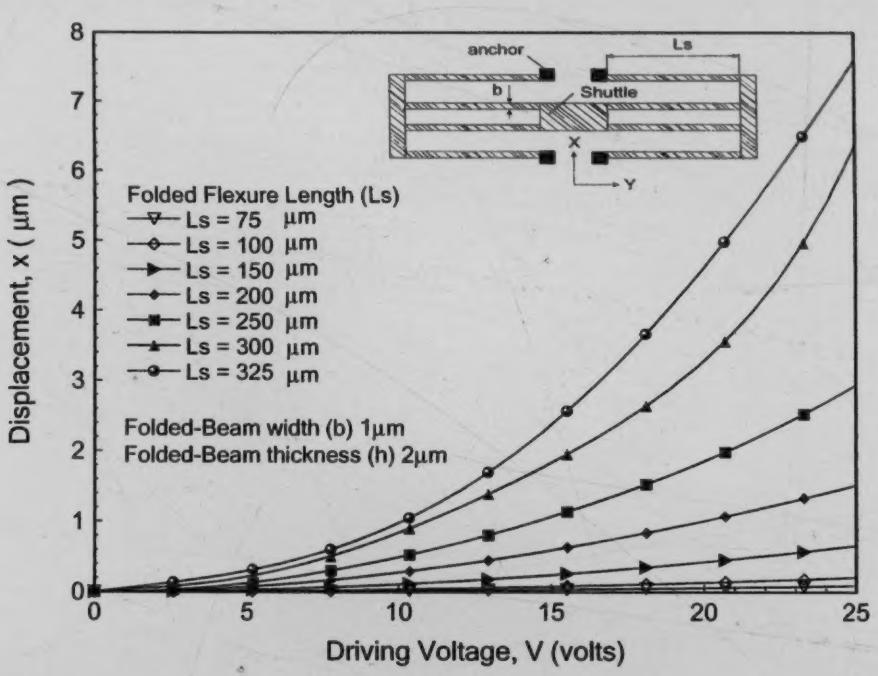

Figure 3.19: The variation of the Comb-Drive Displacement versus driving voltage for several folded-flexure spring designs. All designs have a folded-beam width 1 µm and beam thickness 2 µm

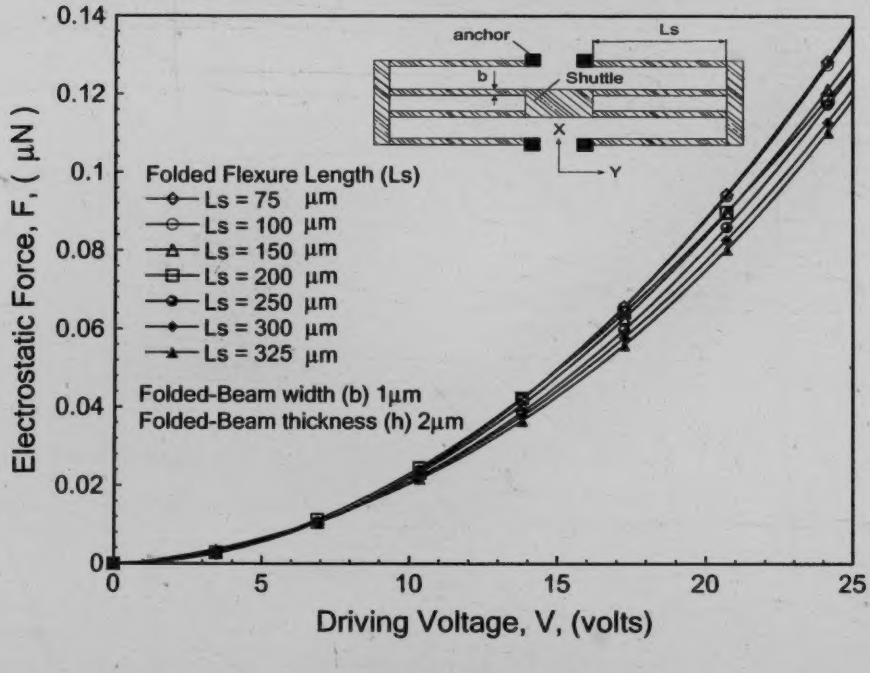

Figure 3.20: The variation of the Comb-Drive generated electrostatic force versus driving voltage for several folded-flexure spring designs. All designs have a folded-beam width 1 µm and beam thickness 2 µm

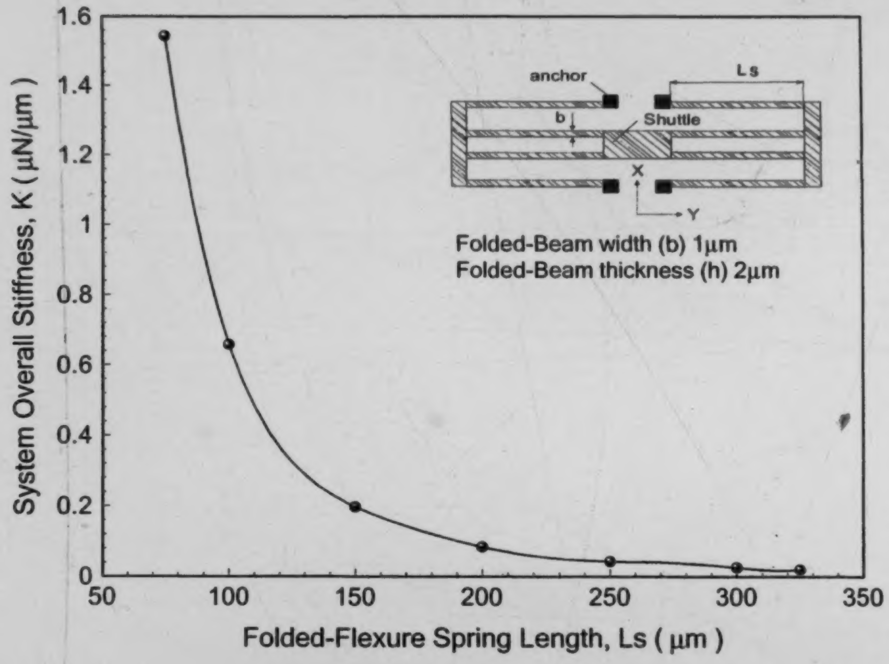

Figure 3.21: The variation of the system overall stiffness of Comb-Drive versus the length of the folded-flexure spring, (L_S). All designs have a folded-beam width 1 μm and beam thickness 2 μm

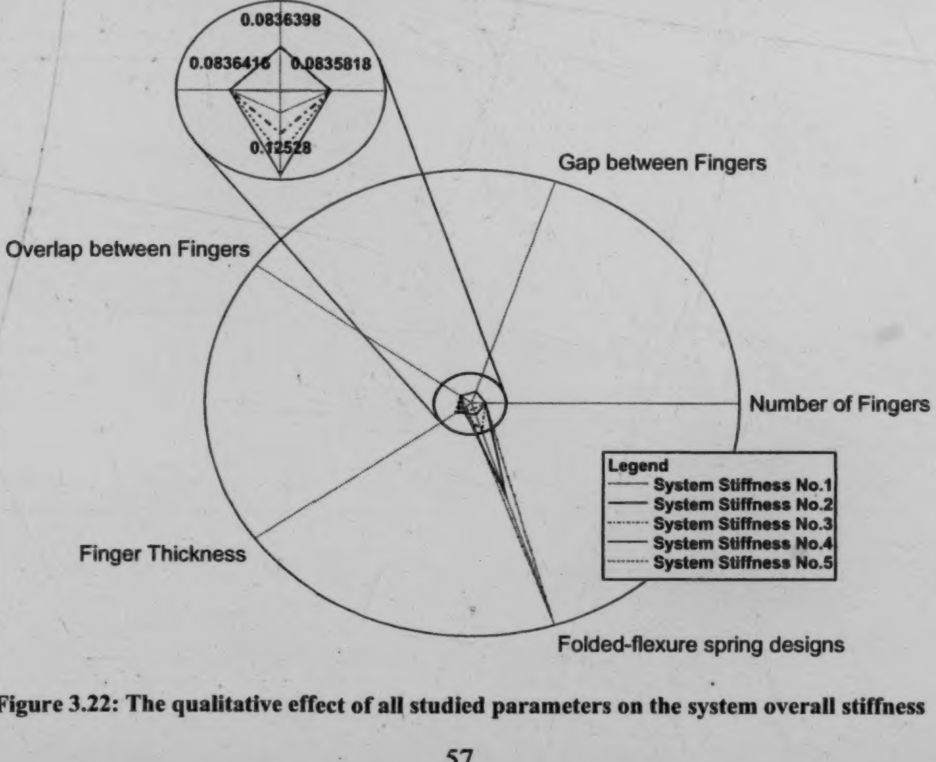

Figure 3.22: The qualitative effect of all studied parameters on the system overall stiffness

Table 3.2: Calculated A_{nm} values for Equations (3.5.8-12)

Coefficient	n	g	K_x	t	L
A_{00}	-3.433E-01	1.473E+00	2.850E-01	2.779E-01	9.433E-01
A_{01}	5.225E-02	-1.852E+00	-5.823E+00	-3.174E-01	-4.364E-01
A_{02}	-1.405E-03	7.992E-01	3.025E+01	4.145E-02	2.384E-02
A_{03}	-6.257E-05	-1.426E-01	-4.564E+01	1.757E-02	-4.629E-04
A_{04}	1.994E-06	9.016E-03	1.840E+01	-3.480E-03	2.90E-06
A_{10}	2.092E-01	-1.259E+00	-4.239E-01	-1.132E-01	-8.083E-01
A_{11}	-1.687E-02	1.641E+00	9.852E+00	1.421E-01	4.355E-01
A_{12}	-1.891E-03	-7.277E-01	-5.413E+01	2.189E-02	-2.605E-02
A_{13}	1.885E-04	1.330E-01	8.325E+01	-2.833E-02	5.459E-04
A_{14}	-3.666E-06	-8.593E-03	-3.382E+01	4.245E-03	-3.71E-06
A_{20}	-1.379E-02	1.435E-01	6.907E-02	1.454E-02	2.252E-01
A_{21}	-8.519E-04	-1.849E-01	-1.558E+00	-2.099E-02	-1.374E-01
A_{22}	5.047E-04	8.214E-02	8.551E+00	3.544E-03	9.764E-03
A_{23}	-3.295E-05	-1.506E-02	-1.315E+01	1.109E-03	-2.244E-04
A_{24}	5.723E-07	9.751E-04	5.345E+00	-2.505E-04	1.64E-06
A_{30}	-5.775E-05	-3.925E-03	-1.914E-03	-2.182E-04	-2.395E-02
A_{31}	1.735E-04	5.425E-03	4.778E-02	6.176E-04	1.593E-02
A_{32}	-3.034E-05	-2.494E-03	-2.696E-01	-1.727E-04	-1.255E-03
A_{33}	1.622E-06	4.664E-04	4.182E-01	-4.096E-06	3.10E-05
A_{34}	-2.606E-08	-3.058E-05	-1.704E-01	4.014E-06	-2.39E-07
A_{40}	6.159E-06	3.169E-05	1.530E-05	7.851E-07	8.445E-01
A_{41}	-3.248E-06	-4.637E-05	-4.077E-04	-5.488E-06	-5.988E-04
A_{42}	4.467E-07	2.206E-05	2.345E-03	2.155E-06	5.04E-05
A_{43}	-2.170E-08	-4.214E-06	-3.660E-03	-2.350E-07	-1.30E-06
A_{44}	3.326E-10	2.803E-07	1.495E-03	-2.574E-09	1.04E-08

Chapter 4

Three-dimensional FE Modeling

4.1 Introduction

In this chapter, 3D finite element modeling of a lateral electrostatic Comb Drive actuator is presented. The 3D FE model was developed to overcome the limitations of the 2D FE model described earlier in chapter three. In chapter three, an accurate, robust, and efficient model for the Comb drive actuator was developed; this model was designed in a parametric fashion. It was used to simulate various geometries of the Comb Drive. In addition to that, different values of voltage loads can be applied to it. Voltage load values ranging from 10 to 50 volts with a step of 10 volts were applied. Although this model was good enough to simulate the Comb Drive and retrieve fast analysis results, it has a few drawbacks. For example, it gives the Comb response in terms of displacement in only one major actuation direction. In addition to that it is not possible to calculate the maximum stresses developed in the system as the system is represented by lumped elements not a real finite element domain.

Also, this model is not capable of predicting the out of plane displacement, which is generated in the Z-direction. This undesirable displacement is due to a phenomenon known as levitation effect, which was described earlier in chapter 2. This phenomenon results from the asymmetry of the applied electric field. For the application of a Comb Drive as a prime source of actuation in a micromirror, this undesired displacement might shift the micromirror from its required position. This position shift could lead to incorrect operation of the entire device. So, it is very important in such MEMS application to study and try to eliminate this displacement component. Therefore, any accurate model for Comb Drive actuators should include characterization of this displacement component.

4.2 Motivation and Chapter Overview

Full 3D simulation for any MEMS device is a vital issue for the design process. It should be done as accurate as possible to have a full understanding of the system response. Accurate prediction of a system's behavior in the real world is important when subjected to the designated loads. Simulations are required prior to fabrication in order to save the invested time and money and make sure that the system behaves according to the design specifications. This motivates the author of this thesis to develop a robust and accurate 3D FE model that can predict and explain the different values of the displacements and stresses developed in the Comb in the 3D.

In this chapter, 3D modeling and analysis of Comb Drive actuator was investigated using two different meshing techniques, which are often used in the three dimensional finite element analysis of Microelectromechanical systems. To start with, a mesh sensitivity analysis was developed for each technique, to determine the best element size that guarantees a consistent and converged analysis results. Then, parametric analysis was conducted to investigate the effect of the design parameters variation on Comb Drive performance. Those design parameters include, the finger thickness, gap size between Comb fingers, length of folded flexure spring beams, and number of Comb fingers. Also, the current study has taken into consideration the variation of the applied driving voltage through a range from 10 to 40 DC Volts. Table 4.1 at page 75 shows the range of the parameters covered in this study. The two meshing techniques were used in the finite element modeling of the Comb Drive and the parametric study was conducted utilizing each one. These applied meshing techniques are commonly referred to in the literature as the Exposed Face Meshing method (EFM), and the Volume Refining Meshing (VRM) method [56]. Finally, at the end of this chapter a comparison between the results of the two meshing techniques will be introduced, showing a significant reduction in simulation process time by the (EFM) method over the (VRM) method. The simulation results were validated by the analytical model results available from the literature.

4.3 Volume Refining Meshing (VRM) method

The volume refining meshing method is the commonly used meshing technique for MEMS devices. This technique is based on meshing the device volumes with discrete size volume elements such as the 10-nodes tetrahedral element or the 20-nodes brick elements. The Volume Refining Meshing (VRM) method is investigated using the commercial finite element analysis software ANSYS™ [44]. In this method, the mesh is refined either locally or globally. The accuracy of the analysis results depends greatly on the mesh density at the comb fingers and the surrounding dielectric material, which leads to a large size problem for complex devices. In addition, a large volume of dielectric material (air) has to be modeled away from the device (e.g. 100 to 200 microns) in order to capture most of the electric field, which is generated due to the applied voltage. This assures a reasonable accuracy in the electrostatic forces calculations. In general the electrostatic force calculation using this method is less efficient and it is computational very expensive for complex and large size devices [57, 58].

Normally the displacement of the electrostatically actuated MEMS devices is calculated through an iterative method or algorithm. This algorithm couples the electrostatic field analysis and the mechanical structural field analysis. Figure 4.1 at page 74 shows a flow chart for the algorithm procedure. First, the algorithm calculates the electric field and electric scalar potential (voltage) distribution caused by the charge distribution. Normally, a standard electrostatic analysis procedure is used for that process. Due to a change in the capacitance between the comb fingers, electrostatic forces are developed on the Comb Drive fingers. The same standard electrostatic analysis procedure is used to calculate these forces. Second, those electrostatic forces, which are normally stored in the air elements, are applied to the corresponding structure elements, which are adjacent to the air elements. These forces cause deformation in the structure. The deformation affects the electrostatic fields due to change in geometry and the electrostatic mesh is updated based on the structure displacement; also the mechanical mesh coordinates are updated as well to match the new structure geometry resulting from the generated forces. An iterative algorithm is required to update both the structure field and the electrostatic field to assure convergence for the displacement. Normally the algorithm convergence is based on a predetermined value for the maximum structural deflection or the stored electrostatic energy change by less than 1% between the current and previous iterative loop. This tolerance value can be customized but the smaller the value is, the longer the time required for the algorithm to converge.

4.4 Finite element procedure for VRM

A *coupled-field analysis* is an analysis that takes into account the interaction (coupling) between two or more disciplines (fields or physics) of engineering. For example, an electromechnical analysis deals with this kind of interaction between the structural and electric fields. It solves for the displacement distribution due to the applied voltage. Normally, microelectromechanical systems exhibit this kind of interaction and require the coupled-field analysis procedure. This type of analysis procedure is most suitable to simulate the studied Comb Drive, since the nature of the Comb Drive physics is an electrostatic-structural coupled-field problem. Many commercial codes applies this coupled-field analysis procedure to solve the microelectromechanical systems model using the (VRM) meshing technique. In order to apply this meshing technique several steps have to be considered.

First, for the current comb model, the studied Comb Drive geometry has to be defined. To do that, a special code was written to generate the Comb Drive geometry in a parametric manner. This is the same code that was used before to develop the 2D FE model in chapter three. Second, the fields or physics have to be defined prior to solution. Preparing an environment for each field did the task of field definition. In this case, the environment represents a file that contains all the operating parameters, characteristics, and the necessary information to define the studied field. For example, the environment for the structural field includes the material properties for polysilicon (Comb Drive beams and Shuttle mass), definition of the 3D solid element that is used to mesh the Comb Drive geometry, meshing information for Comb geometry such as the element size, and structure constraints, etc. The environment file for the electrostatic field contains the geometry definition and meshing of the dielectric material (Air), which is surrounding the Comb Drive. It also contains the definition of the electrostatic element used for the meshing of electrostatic domain, driving voltage load, and dielectric material properties, etc. Normally, the dielectric material (Air) geometry is defined by extruding a solid volume around the Comb Drive, and then this volume is extracted from the Comb Drive volume. The remainder is the air geometry surrounding the Comb Drive. To define the mesh in each environment proper elements have to be used. These elements are required to be capable of representing complex three-dimensional volumes. Also, they should be higher order elements to guarantee reasonable results accuracy. These specifications are available in the 10-node tetrahedral electrostatic element and the compatible 10-node tetrahedral structural element. These elements are referred to, as SOLID123 and SOLID92 respectively in the commercial code ANSYS^{TM}.

Figure 4.2 at page 75 shows a schematic for both elements and indicates the corresponding node numbering for each element. SOLID92 has a quadratic displacement behavior and is well suited to model irregular meshes such as those produced from various CAD/CAM systems. SOLID92 has three degrees of freedom at each node: translations in the nodal x, y, and z directions. SOLID123 has one degree of freedom, voltage, at each node and a flag that can be used at its nodes to store the calculated electrostatic forces. These forces will be transferred to the structure elements to produce system deflection. Third, an algorithm is required to solve both fields and iterate between them until convergence is achieved. This algorithm has to follow the (VRM) technique shown at figure 4.1. Fortunately, a predefined command macro referred to as electrostatic-structural solver **(ESSOLV)** is used in ANSYS to solve the (VRM) meshing for the current Comb Model. **ESSOLV** iterates between both fields and solve them. It calculate displacements and automatically updates the electrostatic field mesh to conform to the structural field based on the displacement using a special procedure referred to as morphing [59].

4.5 Exposed Face Meshing (EFM) method

Many electrostatically activated MEMS devices have specific faces or planes on which the electrostatic force is critical for determining the electro-mechanical behavior. The movable fingers surfaces and fixed fingers surfaces tips are examples of such surfaces, and they are referred to as exposed surfaces because of their exposure to fringe electric fields. The Exposed Face mesh (EFM) method refines only the electrostatic surface mesh on the required exposed faces using boundary element based electrostatic analysis. Exposed Face Meshing method (EFM) is investigated using the commercial finite element analysis software IntelliSense™ [60].

The advantage of this novel meshing method is that the surface mesh used for the electrostatic analysis is separated from the mechanical volume mesh while assuring full compatibility between the two. Each exposed face is refined to a number of electrostatic panels based on the formula, $2*N^2$ plane panels, where N is the refinement factor, so if this factor equals to one then each exposed face will be composed of two electrostatic panels and so on. For coupled electromechanical analysis, the governing system of equations for the electromechanical problem can implicitly be expressed as [56]:

$$S = Fm[(X0(M), Fe(S + X0, V)] \tag{4.5.1}$$

Where X0(M) is a vector representing the MEMS structure, S is the discretized structure surface displacement, M is the multi-material property information, and V is the applied voltage information. From (4.5.1) the numerical error of the structure surface displacement can be derived. The numerical error can be approximated as:

$$\delta S = \left(\frac{\delta F0}{\delta X0}\right)\delta X0 + \left(\frac{\delta Fm}{\delta Fe}\right)\delta Fe \qquad (4.5.2)$$

Assuming that the original structure X0 is correct, the first term on the right of (4.5.2) can be ignored. In (4.5.2), δFm/δFe is the surface displacement increment due to electrostatic pressure changes, which is inversely proportional to the Young's modulus. δFe is the numerical error of the electric force of total structure, which is proportional to the voltage, squared (V^2) and is dominated by the electrostatic pressure discretization error on the Exposed Faces. The numerical error will increase as the structure's flexibility increases. To reduce δFe and, therefore to suppress the numerical error, the Exposed Face Mesh method can be applied. The more flexible the structure is, the larger the refining factor should be set in the EFM algorithm to keep the numerical error within the given tolerance.

Figure 4.3 at page 76 shows a flow chart for the procedure used in the Exposed Face mesh (EFM) method. First, the algorithm calculates the Electric charges distributions over the exposed faces due to the scalar potential (voltage) distribution and performs standard electrostatic analysis. Electric charges distributions over the exposed faces are then mapped to the global surface mesh and the developed electrostatic forces due to a change in the capacitance between the comb fingers are calculated. Second, the global surface mesh, which has the electrostatic forces distribution, is attached to the 3-D volume mesh and the electrostatic forces distribution is transferred to the 3-D volume mesh as a standard mechanical loads. Third, a standard finite element mechanical analysis is performed on the entire structure volume and the structure mechanical deformation is calculated, finally the deformation tolerance criterion is checked via the predetermined value, if the criterion is reached the analysis ends, but if not the analysis loops again from the previous deformation state and continue on until we reach the deformation criteria. The (EFM) uses boundary layer element coupled with Relaxation/Multipole-accelerated iterative scheme to map and calculate the electrostatic forces, which reduce the problem size and complexity [61, 62].

EFM method uses boundary elements for electrostatic mesh. Unlike the 3D solid finite element mesh, boundary elements cover only the surface of the structure and they are used because charge density collects and accumulates on the surfaces and edges of the conductors, so there is no need to mesh air gaps between the different conductors, which leads to small size problems and efficient simulation of MEMS devices. Using the (EFM) method, the electrostatic surface mesh can be customized at the areas of high potential gradients such Comb Drive fingers to achieve high accuracy results for electrostatic analysis, while the finite element volume mesh can be refined independently at the areas of high mechanical deformation and high stress gradients such as the beams of the folded flexure spring in order to provide correct mechanical analysis results.

4.6 Finite element procedure for EFM

The term Relaxation in the EFM procedure refers to the nonlinear Gauss-Seidel relaxation algorithm that is used to combine the standard finite element method for mechanical analysis and the multi-accelerated boundary-element based electrostatic analysis solver, FASTCAP [63]. Therefore, commercial codes such as IntelliSense^{TM} use this algorithm to solve the coupled electromechanical systems. The relaxation analysis is used to predict the Comb Drive performance when subjected to DC voltage loads. The analysis uses the (EFM) algorithm as described in section (4.5), and the parametric study was conducted for the same design parameters mentioned before in the (VRM) section.

The (EFM) procedure uses a higher order quadratic displacement behavior 20-node brick element for its finite element analysis. This element is essential for accurate analysis of specific engineering applications which involve electrostatics. It is characterized by high quality and accuracy in addition to the ability to capture the internal geometry of a model with curves [64]. These elements can capture the device behavior without the requirement of fine discretization (especially through the thickness of the model), which leads to significantly smaller problem sizes with high accuracy results. The following steps were implemented to perform the relaxation analysis:

- Generating a finite element model for the Comb Drive geometry that utilizes the 20-node brick elements. Since, we are conducting a parametric study, it was very useful to customize a code that can build any geometry combination of the Comb Drive. This code was written in ASCII format as an input file using ANSYS^{TM} Parametric Design Language (PDL). This code is capable of creating the geometry and meshing it with 20-node brick element type, and then the solid Comb Drive model was imported and opened in the graphical user interface (GUI) of the Electromechnical Analysis module of IntelliSense^{TM} for further mesh refinement.

- The Electrostatic mesh was refined by a factor of two only at the chosen exposed faces, Figure 4.4 at page 77 shows the electrostatic mesh refinement as the Comb fingers have double the number of electrostatic panels than other parts of the comb- drive, while the ground plane was only refined at the upper surface facing the device to capture the levitation effect due to electric field asymmetry which leads to vertical Comb displacement away from the ground plane. Other areas that were not electrically important had been removed from the electrostatic mesh.
- Voltage loads were applied to the Comb Drive and fixed boundary conditions were applied to the anchors of both the moving Comb and the fixed Comb as well.
- Finally, Analysis parameters like the number of iterations during solution and convergence criteria were defined prior to starting the solution.

Figures 4.5 at page 77 and figure 4.6 at page 78 shows the mesh sensitivity analysis for both the mechanical mesh and the electrostatic mesh respectively. Mesh sensitivity analysis was performed to determine the optimum minimum number of electrostatic panels and mechanical finite elements to assure good accuracy with the minimum problem size possible.

4.7 Results and Discussion

In this work, the lateral electrostatic Comb Drive actuator is simulated using two different meshing techniques; the EFM method and the VRM method and the effects of the Comb Drive design parameters on the actuation performance are explored. A full 3D parametric model is developed for each method. Figure 4.7 at page 79 shows a comparison between the simulation results for both methods and the analytical results of the comb drive. On one hand, the simulation for the displacement response for the EFM method is in a good agreement with analytical method over a typical range of operational voltages from 10 to 40 volts. The error of the maximum displacement between both results is less than 10%. This proves, that EFM method is a good choice for an accurate and reliable approach that can be used effectively to predict the response of the Comb Drive. On the other hand, the VRM method results significantly deviate away from the analytical results and need to be fine-tuned. Table 4.2 at page 78 shows a comparison of simulation process time for different meshing methods. The EFM method showed a 46% reduction in simulation process time over the (VRM) method. In addition to that, an accuracy improvement of 38% over (VRM) was achieved when validated with the analytical results.

Yie et al. [56] shows that EFM method showed much more improvement in accuracy rather than the standard volume refining mesh method for a typical Comb Drive problem. Table 4.3 at page 79 compares the two methods and summarizes the features and limitations of each one. For example, the strong coupling between the physics in the EFM method and the usage of the efficient boundary elements to calculate the electrostatic pressure distribution is one of the most important factors that lead to accurate and reliable results. Method convergence also has an important role. For example, one of the problems associated with the VRM method is the gap closure between comb fingers at high driving voltage, where finite element size can reach a zero-volume condition and leads to algorithm failure and abortion of the numerical process. While, in (EFM) no meshing is required for the air gap, which prevents this problem.

Figures 4.8 and 4.9 at page 80 shows the variation of the Comb displacement and generated stresses with the number of fingers at a driving voltage of 40 volts. In these figures, the calculated Comb displacement and generated stresses are shown to be linearly proportional to the number of Comb fingers. For constant spring stiffness, since stresses are related to the displacement and the material's Young's modulus, it is expected that the stresses also vary linearly with the number of fingers in the studied Comb-Drive. In addition, when the driving voltage is increased, the comb displacement is shown in Figure 4.10 at page 81 is nonlinearly increased for a comb design with 20 fingers. In this figure, the displacement rate of the variation is shown to increase with the driving voltage. This is also valid for Figure 4.11 at page 81 where the variation of the stresses versus the voltage is shown.

The results in Figure 4.12 at page 82 indicate that for a driving voltage of 40 volts, as the gap (g) between the Comb finger decreases, the induced capacitance nonlinearly increases and so does the induced Comb displacement. This effect of the Comb gap is also expected based on equation (3.3.5). In this case, the displacement variation rate is shown to decrease with the increase of the gap (g). This effect is also calculated for stresses shown in Figure 4.13 at page 82. The effect of the Comb-Drive finger thickness on its displacement value is shown in Figure 4.14 at page 83. In this case, the finger thickness (t) is varied between 2.5, 2.0 and 1.5 μm. The driving voltage is then increased and the displacement is calculated. Figure 4.14 shows the increase in the Comb displacement is nonlinearly proportional with the increase in the finger thickness, where the rate of displacement variation decreases for higher finger thickness. This effect on stresses is also seen in Figure 4.15 at page 83. Finally, Figure 4.16 at page 84 [and figure

4.17 at page 84 for the stress case] shows the displacement variation with the driving voltage at different spring designs. As the Comb-Drive folded-flexure length increases the spring stiffness in the actuation direction decreases, which increases the displacement of the Comb. Figures 4.18 to 4.22 through page 85 to 87 show the same results in a dimensionless form.

Conclusion

During the course of this work, to overcome some limitations in the 2D model developed earlier in chapter three, a full 3D parametric model was constructed. This 3D model utilized the application of two different meshing techniques commonly known as the Volume Refining Meshing (VRM) method and the Exposed Face Meshing method (EFM). The latter, showed a significant reduction in the computation time over the VRM method with better agreement with the analytical results. On one hand, the simulation for the displacement response for the EFM method is in a good agreement with the analytical method over a typical range of operational voltages from 10 to 40 volts and the error of the maximum displacement between both results is less than 10%. On the other hand, the VRM method results are significantly deviated away from the analytical results and need to be fine-tuned. Simulation process time comparison for different meshing methods showed a 46% reduction in simulation process time over the VRM method. In addition to that, an accuracy improvement of 38% over VRM was achieved when validated with the analytical results. However, the VRM method is characterized by the ability to develop input files that can be easily used to create the model geometry and perform the analysis process without the need to use the GUI. This advantage is highly desirable for the parametric and optimization studies. Moreover, in the EFM method the simulation process steps such as load application and mesh refinement, etc has to be performed through a GUI, which is a cumbersome process. Therefore, if the VRM results could be calibrated to the accurate EFM results, then it can be used efficiently in the optimization process and could be used to speed up the simulation process. To do that, a calibration tool based on the Artificial Neural Network is developed in chapter five.

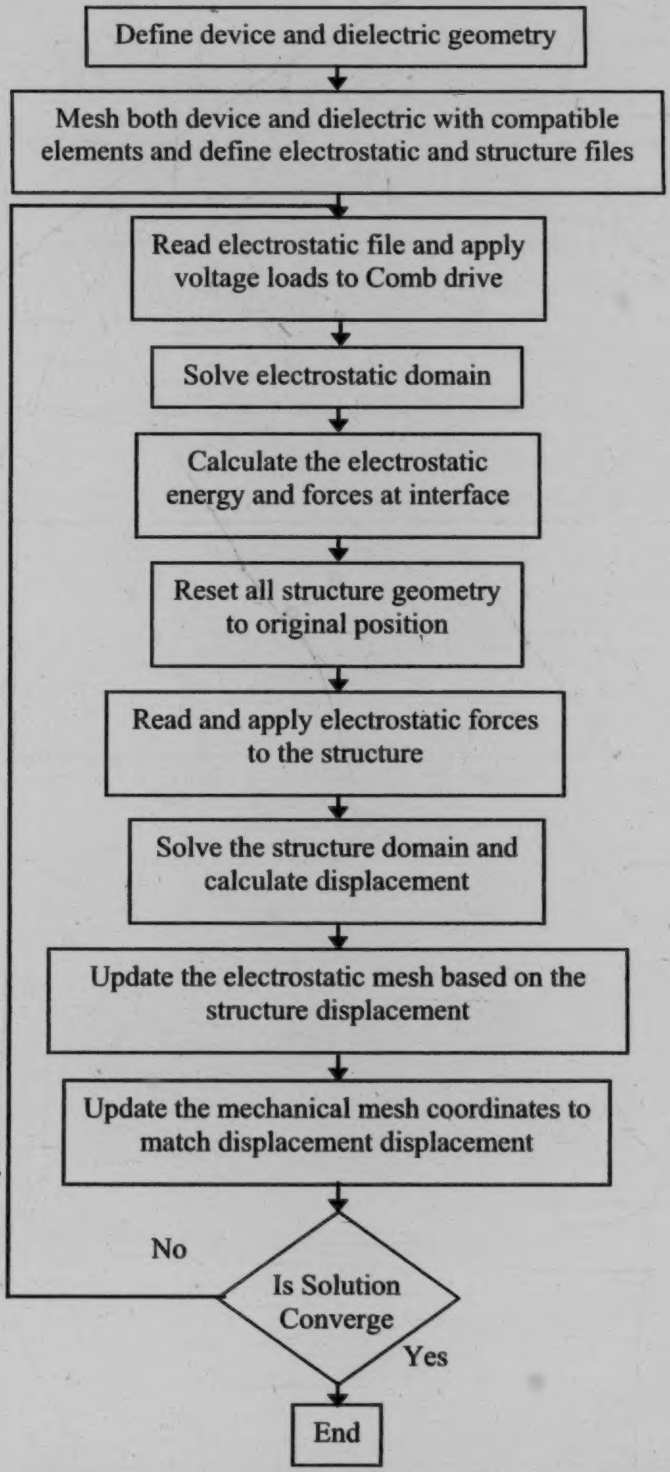
Define device and dielectric geometry
Mesh both device and dielectric with compatible elements and define electrostatic and structure files
Read electrostatic file and apply voltage loads to Comb drive
Solve electrostatic domain
Calculate the electrostatic energy and forces at interface
Reset all structure geometry to original position
Read and apply electrostatic forces to the structure
Solve the structure domain and calculate displacement
Update the electrostatic mesh based on the structure displacement
Update the mechanical mesh coordinates to match displacement displacement
No
Is Solution Converge
Yes
End

Figure 4.1: Flow chart for the coupled-field electrostatic structural analysis using (VRM) method

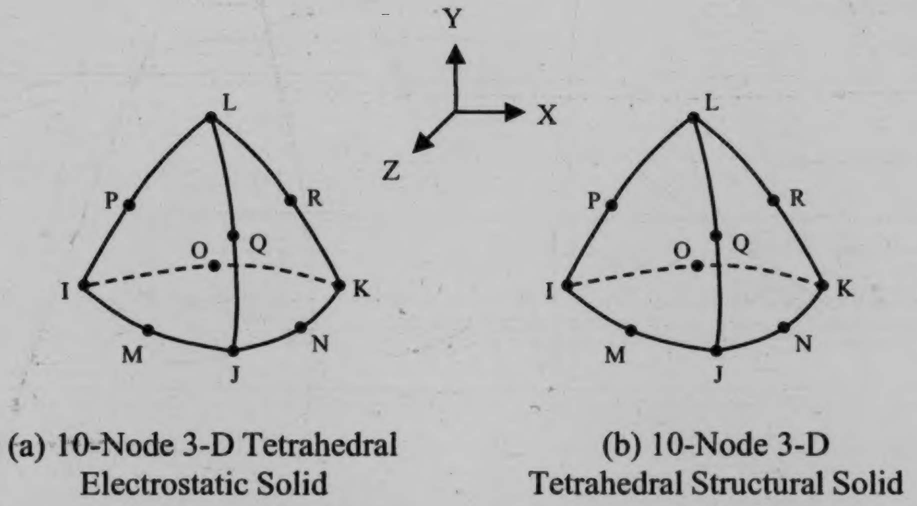
Y
X
Z
L
P
R
O
Q
I
K
M
J
N
(a) 10-Node 3-D Tetrahedral Electrostatic Solid
(b) 10-Node 3-D Tetrahedral Structural Solid

Figure 4.2: Elements description used in the (VRM) method: (a) SOLID123 and (b) Solid92

Table 4.1: Design parameters for Comb Drive Actuator

Design Parameter	Value range
Number of Comb Fingers (n)	10 ~ 20
Finger thickness (t)	1.5 ~ 2.5 μm
Gap between Comb Fingers (g)	1.5 ~ 2.5 μm
Folded flexure spring length (Ls)	75 ~ 200 μm
DC driving Voltage (V)	10 ~ 40 Volts

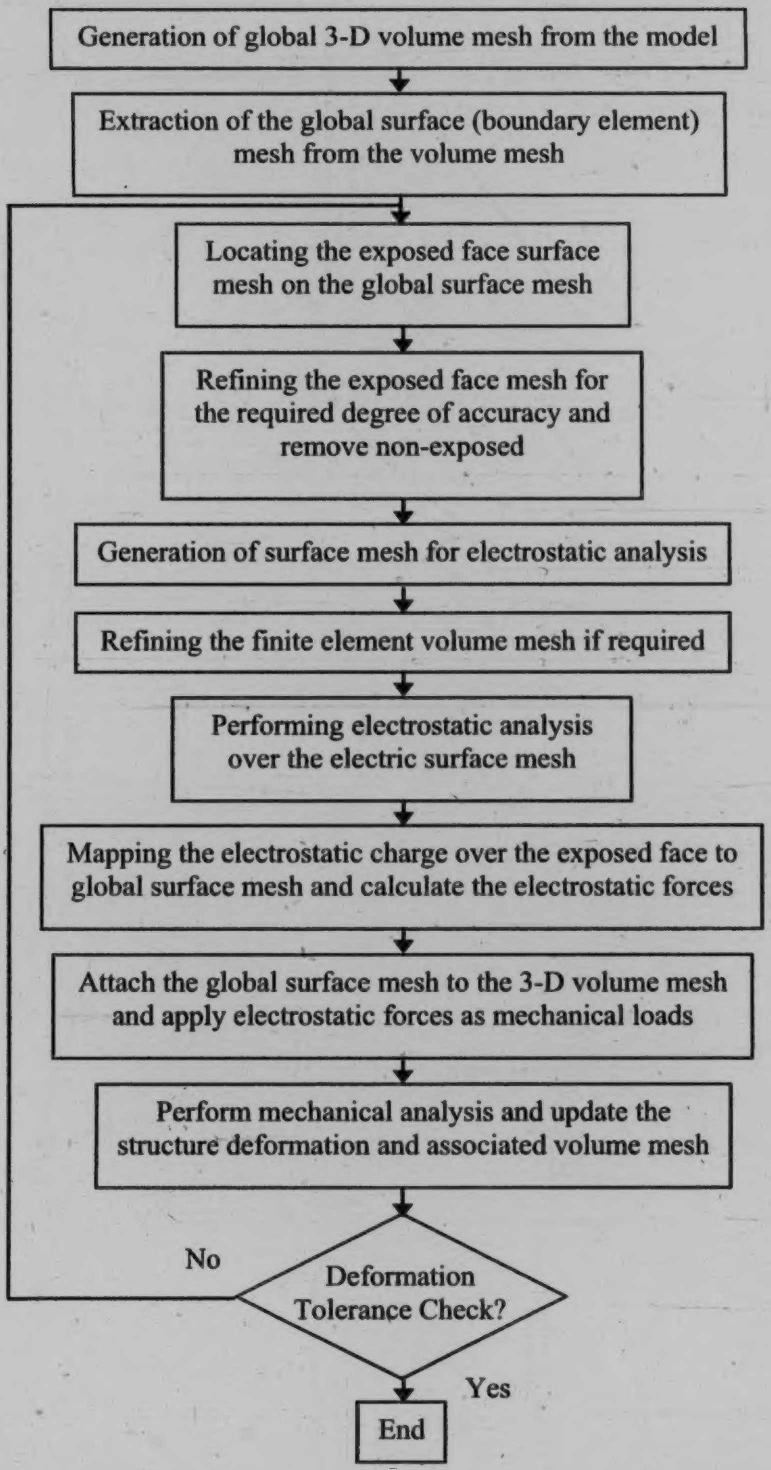
Generation of global 3-D volume mesh from the model
Extraction of the global surface (boundary element) mesh from the volume mesh
Locating the exposed face surface mesh on the global surface mesh
Refining the exposed face mesh for the required degree of accuracy and remove non-exposed
Generation of surface mesh for electrostatic analysis
Refining the finite element volume mesh if required
Performing electrostatic analysis over the electric surface mesh
Mapping the electrostatic charge over the exposed face to global surface mesh and calculate the electrostatic forces
Attach the global surface mesh to the 3-D volume mesh and apply electrostatic forces as mechanical loads
Perform mechanical analysis and update the structure deformation and associated volume mesh
No
Deformation Tolerance Check?
Yes
End

Figure 4.3: Flow chart for the coupled-field electrostatic structural analysis using (EFM) method

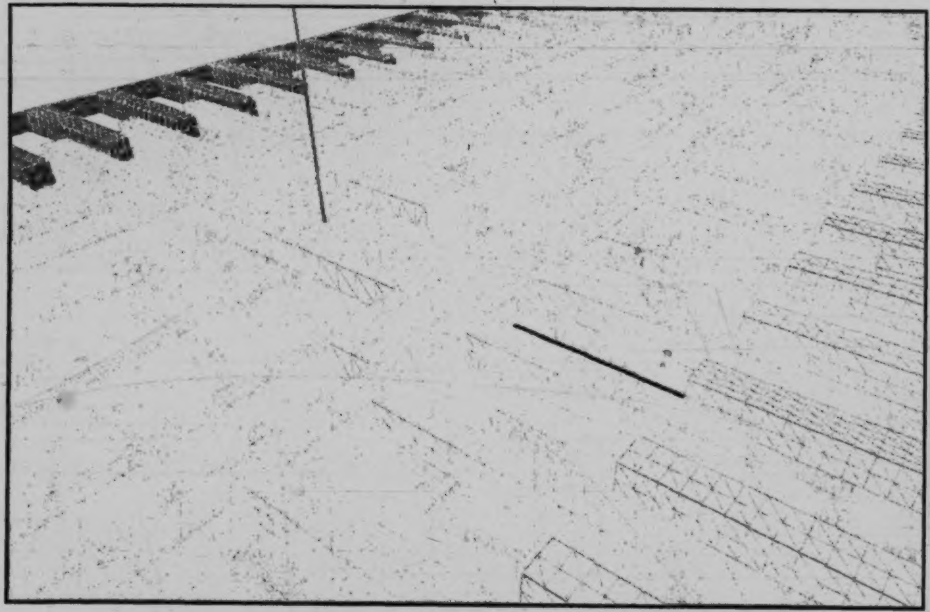

Figure 4.4: Electrostatic mesh refinements for Comb Drive Actuator

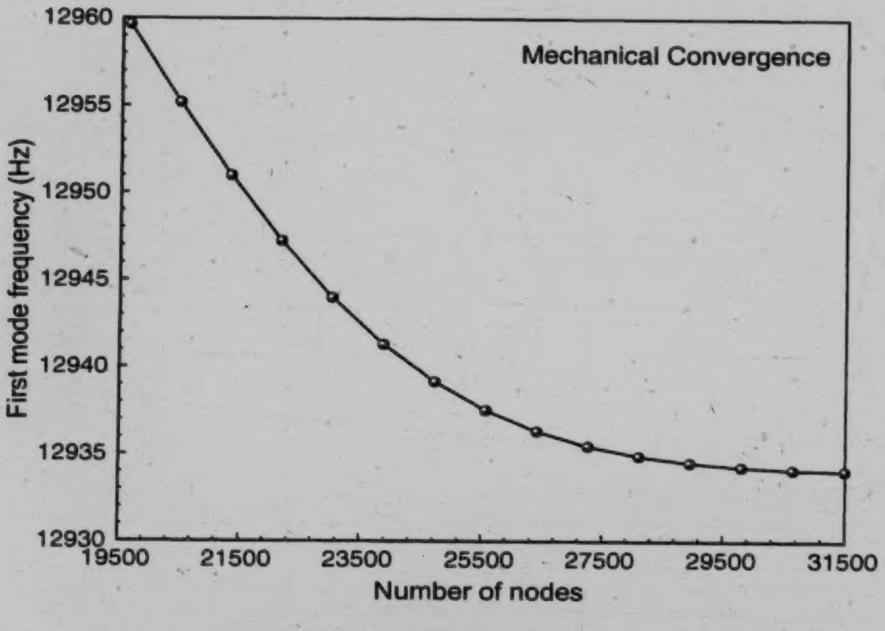

Figure 4.5: Mechanical Mesh sensitivity analysis for Comb Drive Actuator

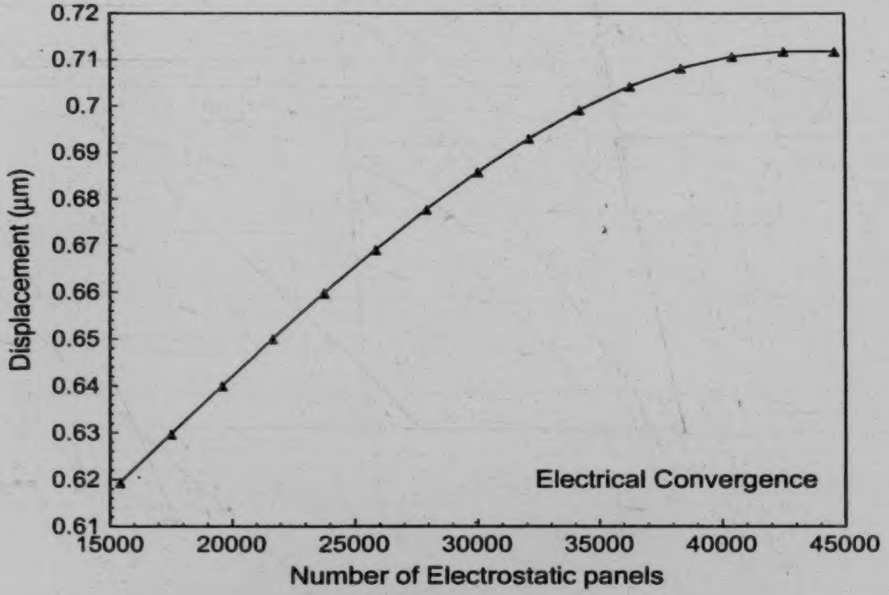

Figure 4.6: Electrostatic Mesh sensitivity analysis for Comb Drive Actuator

Table 4.2: Comparison of simulation process time for different meshing methods

Method	CPU Time (min)	Displacement. (μm)
EFM	175	1.852
VRM	330	1.185
Analytical	--------	2.055

Table 4.3: Comparison between meshing methods

Feature	(VRM Method)	(EFM Method)
Geometry	2-D, 3-D	3-D
Physics Coupling	Weak	Strong
Analysis Type	Static, Transient	Static, Transient, Harmonic
Convergence	Slow, Not robust	Fast, Robust
Mesh Updating	External	Internal
Air gaps Meshing	Required	Not Required
Electrostatic Force Calculation	Weak	Strong
Zero element size (Algorithm Failure)	Possible	Not Possible
Parametric study flexibility	Easy	Not Easy (requires external input files)
Geometry Building using input files	Available	Not Available
Mesh refinement	Dependent	Independent
Problem Size	Large	Small
CPU computational time	High	Low
Air Modeling	Volume elements	Boundary elements

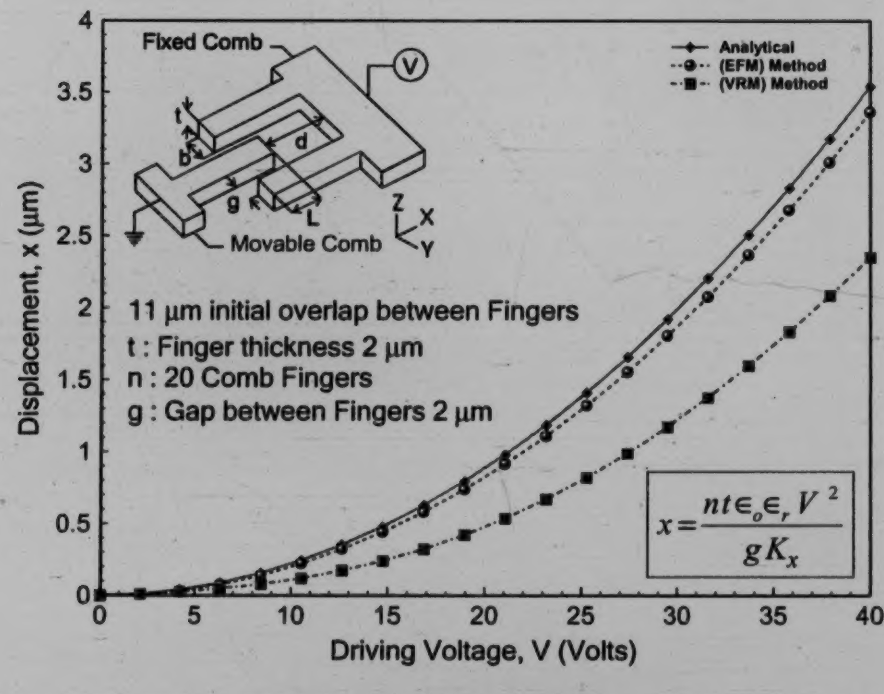

Figure 4.7: The variation of Comb Drive displacement vs. the applied driving voltage, (V): Comparison between analytical and simulation results

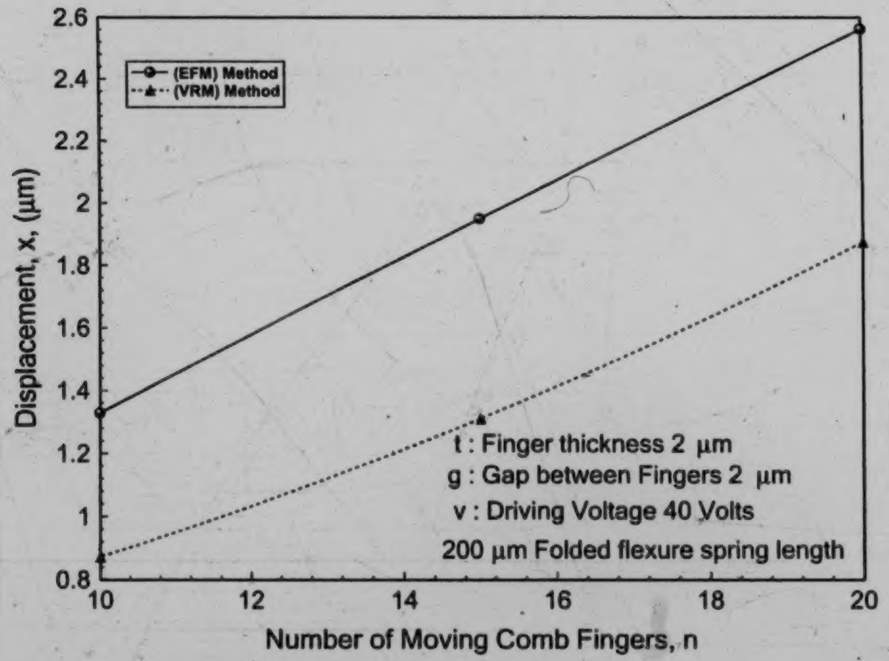

Figure 4.8: The variation of the Comb Drive displacement vs. the number of moving fingers (n)

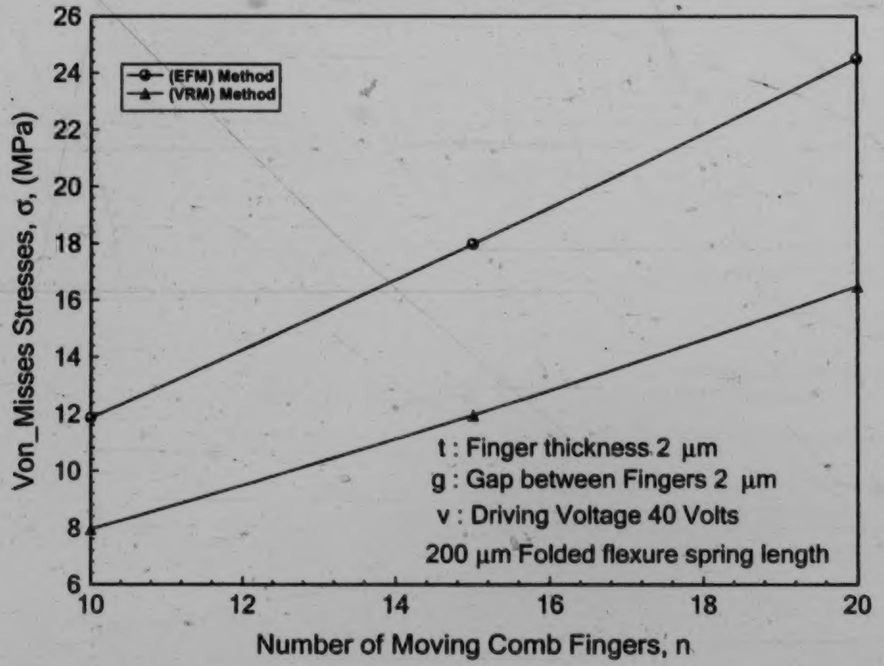

Figure 4.9: The variation of the Comb Drive stresses vs. the number of moving fingers (n)

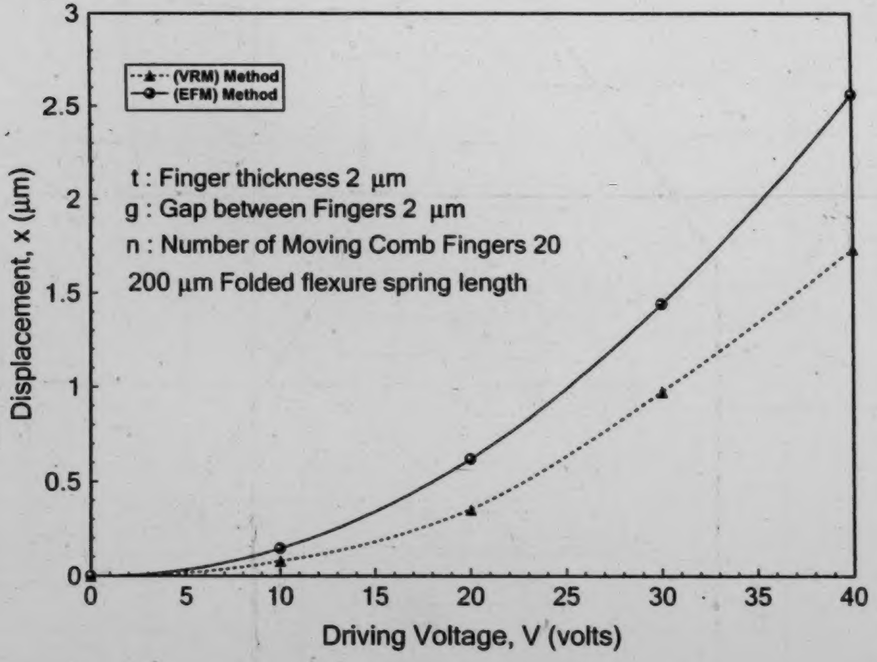

Figure 4.10: The variation of the Comb Drive displacement vs. the applied driving voltage (V)

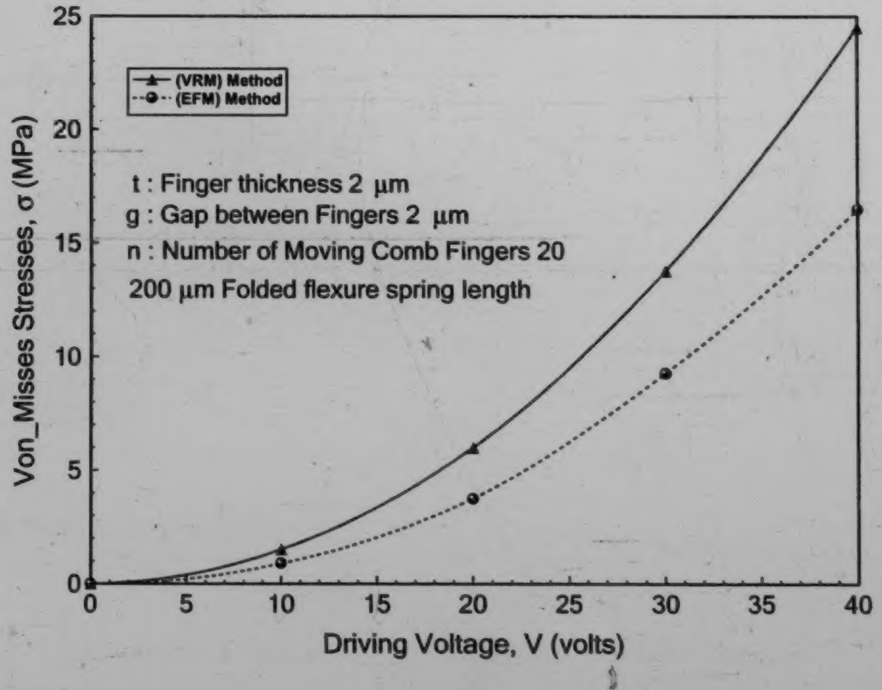

Figure 4.11: The variation of the Comb Drive stresses vs. the applied driving voltage (V)

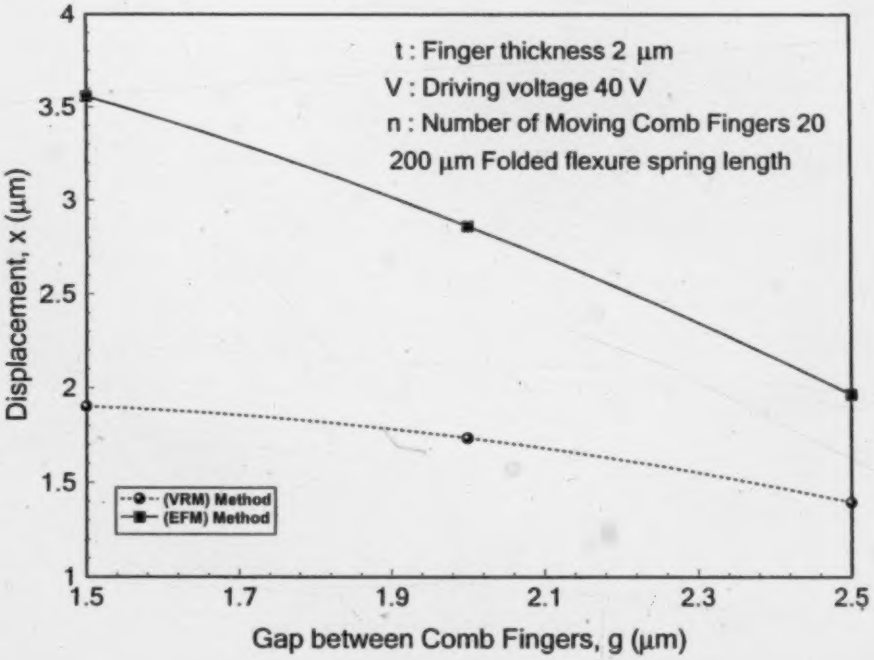

Figure 4.12: The variation of the Comb Drive displacement vs. the gap (g) between Comb fingers

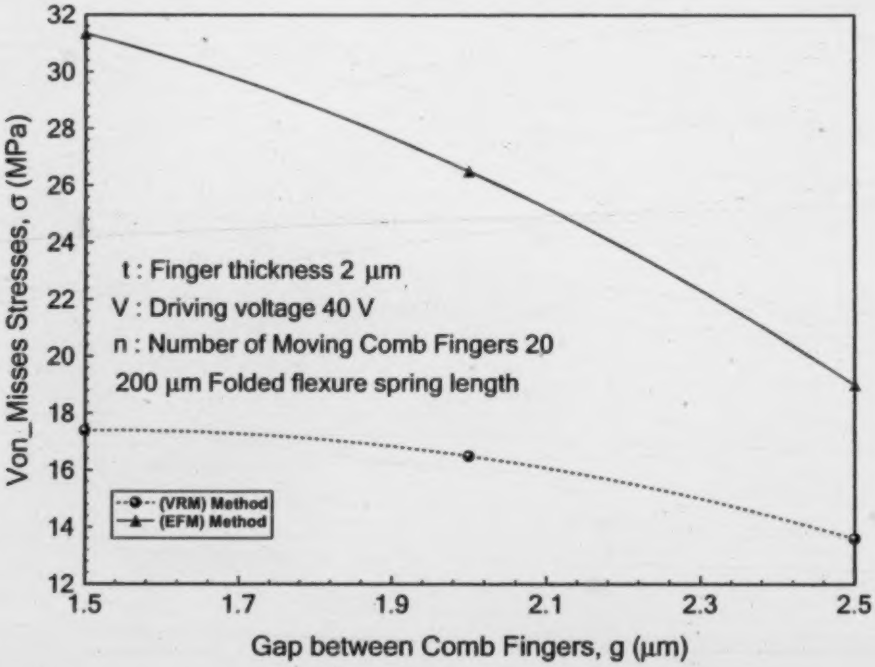

Figure 4.13: The variation of the Comb Drive stresses vs. the gap (g) between Comb fingers

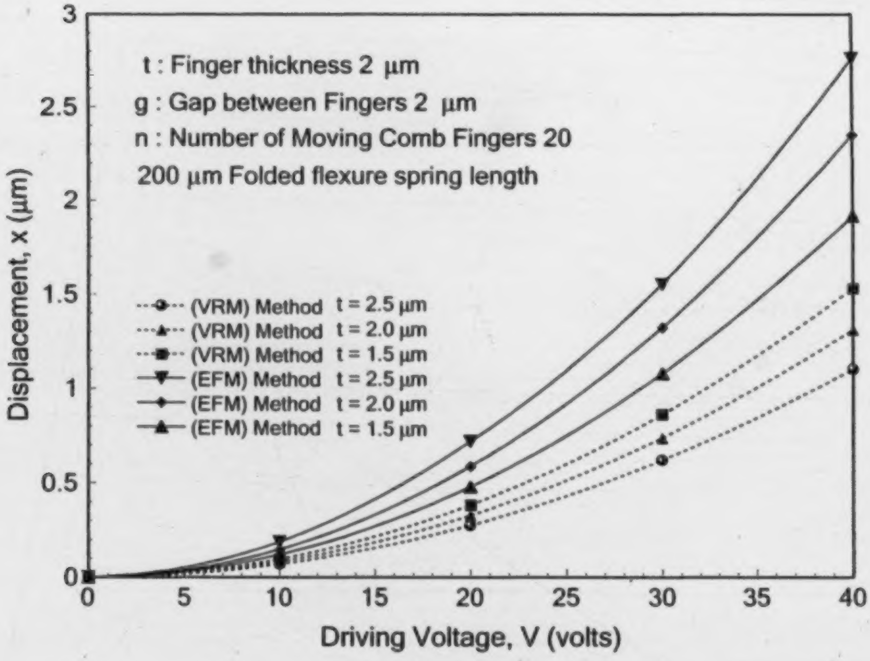

Figure 4.14: The variation of the Comb Drive displacement vs. the driving voltage at different finger thicknesses

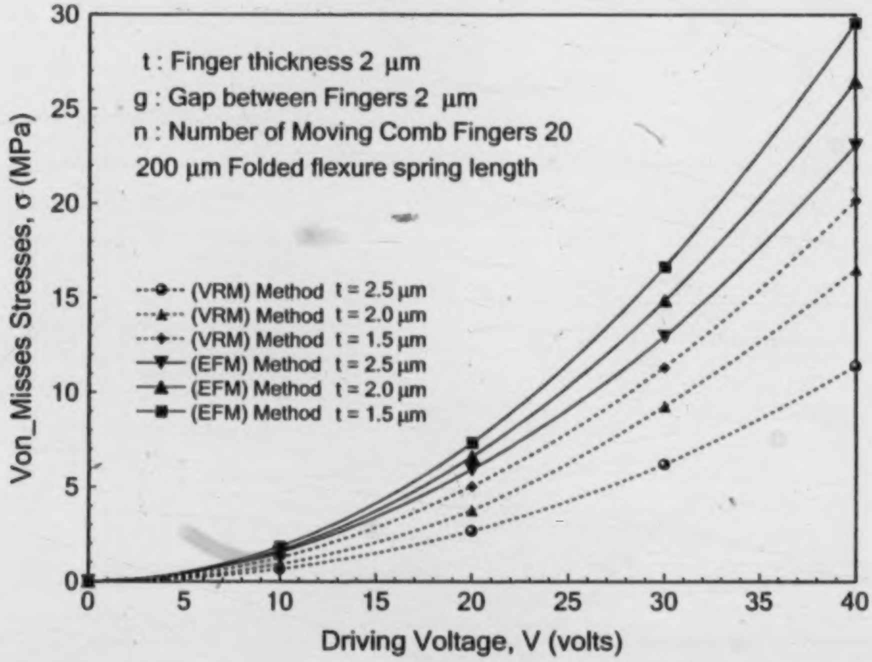

Figure 4.15: The variation of the Comb Drive stresses vs. the driving voltage at different finger thicknesses

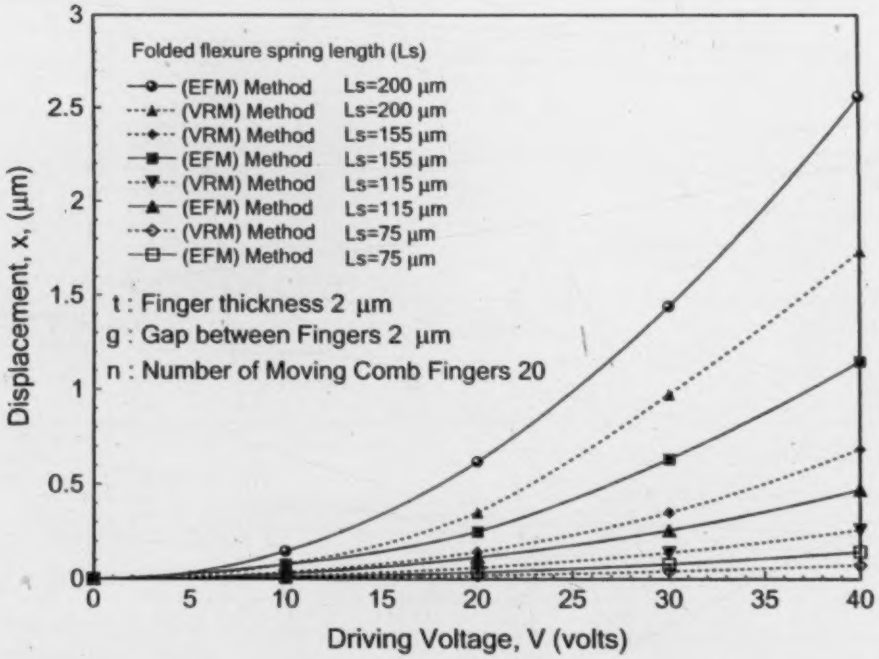

Figure 4.16: Comb Drive displacement vs. the driving voltage for different folded flexure spring design

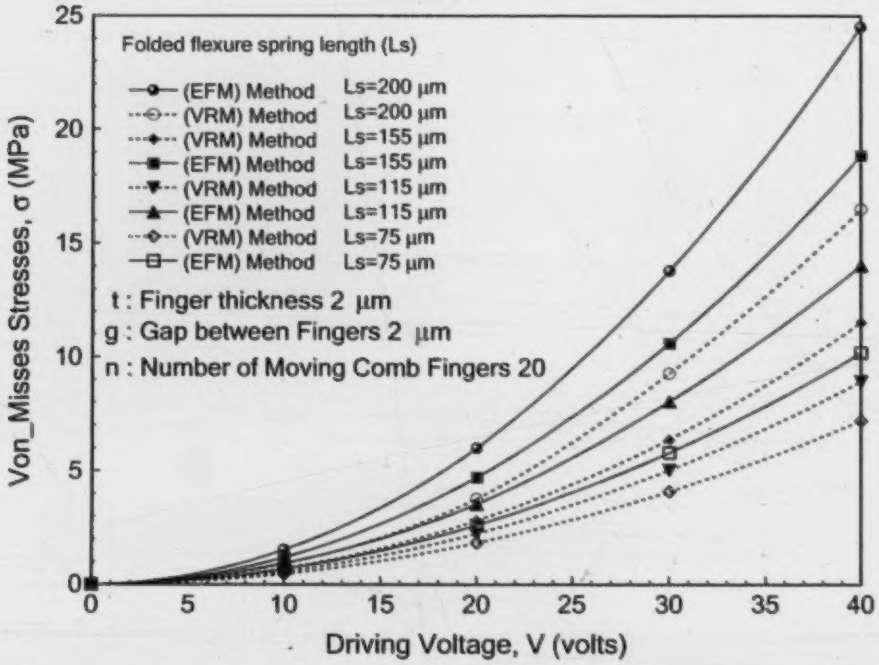

Figure 4.17: Comb Drive stresses vs. the driving voltage for different folded flexure spring design

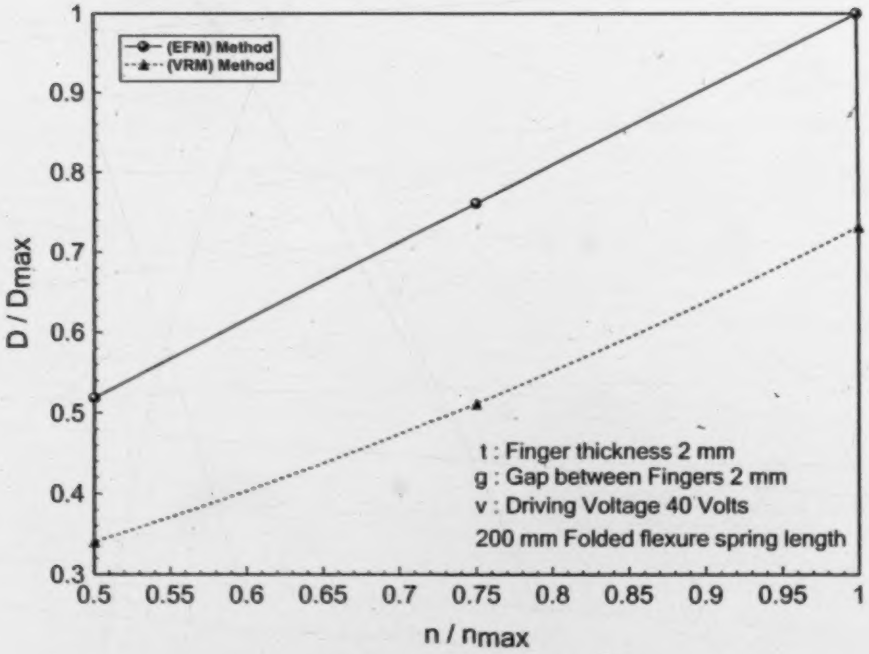

Figure 4.18: Comb Drive displacement vs. the number of moving fingers (n) in dimensionless

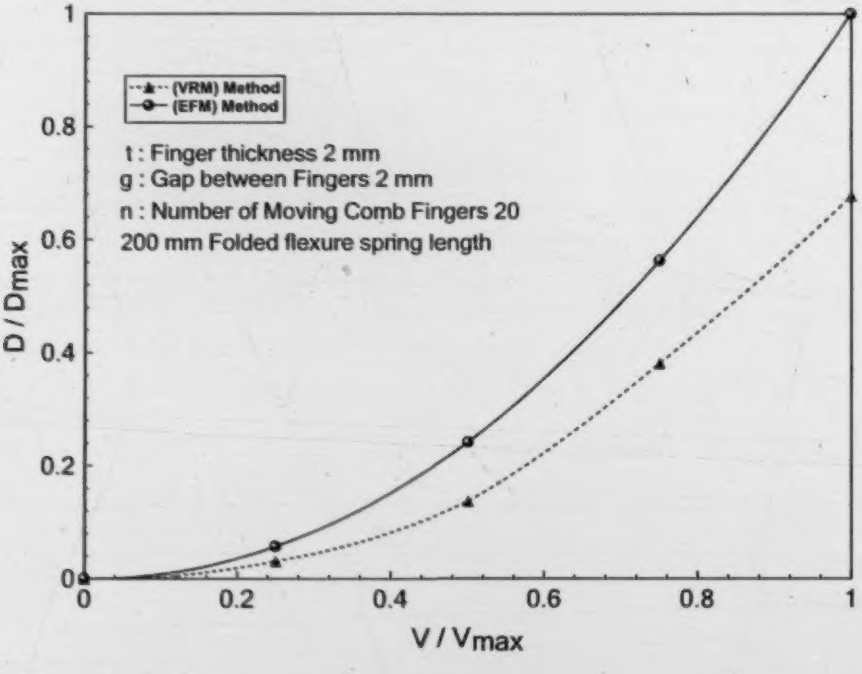

Figure 4.19: Comb Drive displacement vs. the applied driving voltage (V) in dimensionless

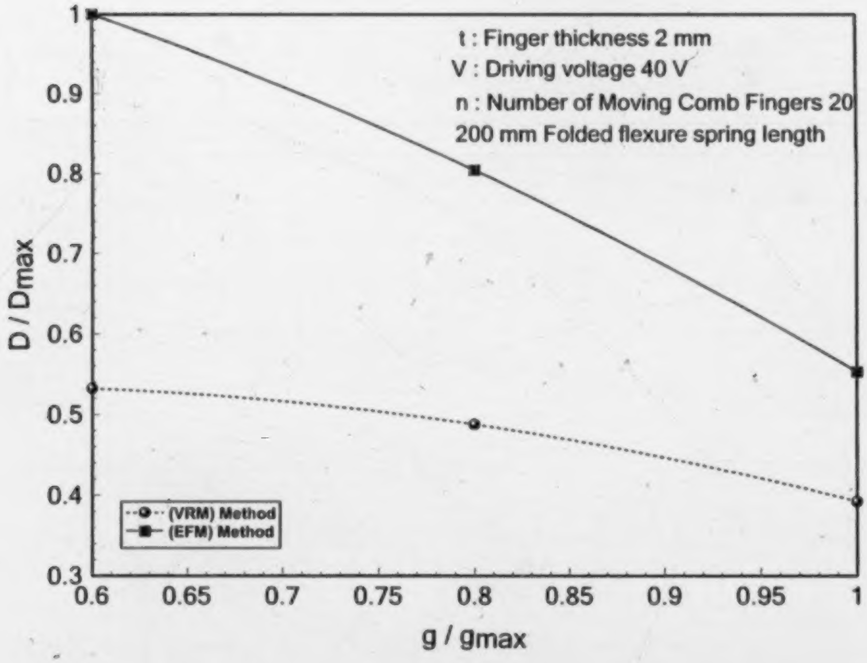

Figure 4.20: Comb Drive stresses vs. the gap (g) between Comb fingers in dimensionless

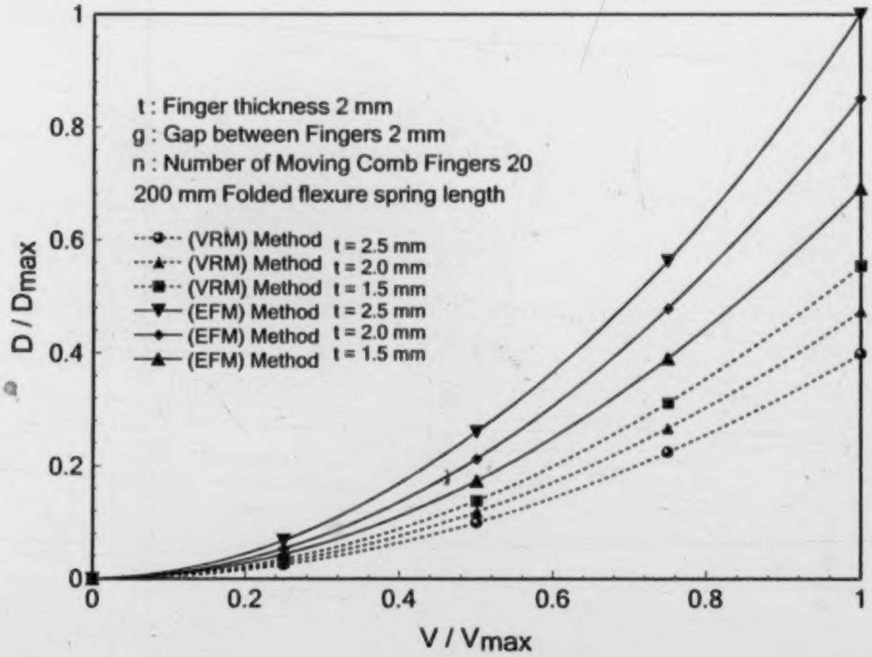

Figure 4.21: Comb Drive displacement vs. the driving voltage for different finger thickness in dimensionless

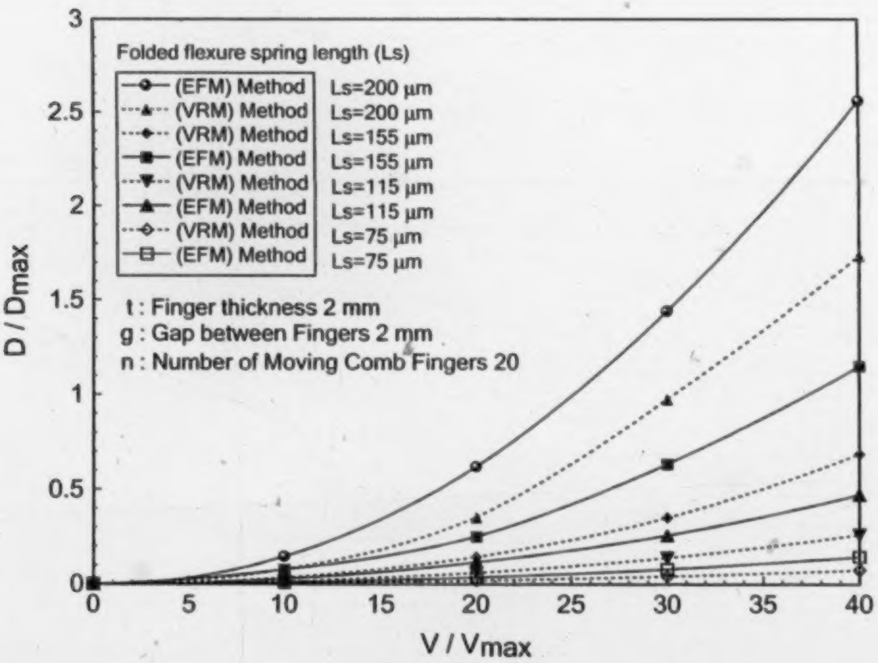

Figure 4.22: Comb Drive displacement vs. the driving voltage for different folded flexure spring design in dimensionless

Chapter 5

Application of Artificial Neural Network

5.1 Introduction

In this chapter, an artificial neural network (ANN) research is conducted in order to further understand and predict the performance of the comb-drive actuator. Feedforward Backpropagation neural networks were applied to calibrate the FE results of the VRM method based on the FE results produced by the EFM method. Neural networks were created using MATLAB and the Neural Network Toolbox. Parametric studies were carried out to determine the optimal networks architecture. The network's approximation accuracy in terms of mean absolute error and correlation coefficients is shown as well. These networks showed a good generalization performance and the values of the coefficients of multiple correlations, extracted from regression analysis were quite satisfactory.

5.2 ANN Literature Review

Artificial neural networks (ANN's) are inspired by processes present in biological nervous systems. Modern computers excel at well-defined computational tasks. Whereas Biological brains, can easily solve complex and poorly defined problems under wide range of conditions, such as speech and vision impairments. Modern computers cannot solve those complex tasks adequately. This inadequacy has prompted researchers to study biological neural systems in an attempt to design computational systems that mimic the computational capabilities of the human brain [65] .

Artificial neural networks offer several advantages. These include, but are not limited to learning from previous examples, the ability to generalize a certain function or task after learning, fault tolerant, and adaptivity. ANN's have been studied for more than 30 years. Recently, there has been a major revival of interest in neural networks, which stems from the development of improved learning algorithms, and the development of different neural networks that are capable of solving complex computational problems.

Neural networks have been applied successfully to many areas including sonar signal processing [66], speech recognition [67], image compression [68], and adaptive process control [69]. Artificial Neural Networks (ANN's) have been reported in the literature as a tool that can be used to predict and approximate the simulation and analysis of different MEMS devices. They have shown that after the learning process is applied, a significant time reduction in simulation is achieved over the finite element approach with less than 1.4% error. For example, a study published by Tay et al. [70] used a Feedforward Backpropagation neural network as an approximation based approach to macro modeling for the simulation of a lateral folded beam comb-drive resonator. Similarly, Mikulchenko et al. [71] used a neural network based Macromodel to simulate the micro-fluidic system of a micro-fluidic sensor, and they optimized the design of flow sensors. This neural network model simulates both the steady-state and dynamic operation of the flow sensor. The numerical solutions of the PDEs describing the micro-fluidic sensor are used as the training data for the neural network. These reports indicate the promising potential of using ANN's in the field of MEMS design and simulation. This is because ANN's have the following useful features [72]. They are:

- General: ANN's produce reasonable outputs for inputs not encountered during the training (learning).
- Robust: ANN's work well with noisy and incomplete data.
- Universal: ANN's can approximate any smooth function even with some discontinuities.

Neural networks as a nonlinear and adaptive computational tool provide interesting possibilities in many applications. These include the control and identification of smart structures and microelectromechanical systems (MEMS) [73-76]. A study published by Cheng et al. [77], for example, addressed the problem of stable tracking control of a flexible micro manipulator. They used a two layer neural network to approximate the nonlinear robot dynamic behavior of the system. From their study, they were able to develop a controller for the micro arms of the system without any need for prior knowledge of the dynamic model of the controlled system. Similarly, Liang et al. [78] proposed a neural-network-based method for model reduction that combines the generalized Hebbian algorithm (GHA) with the Galerkin procedure to perform the dynamic simulation and analysis of nonlinear microelectromechanical systems (MEMS). In their study, an unsupervised neural network is adopted to find the principal eigenvectors of a correlation matrix of snapshots. It has been shown that the extensive computer results of the principal component analysis using the neural network of GHA can extract an empirical basis from numerical or experimental data. This can be used to convert the original system into a lumped low-order Macromodel. The Macromodel can be employed to carry out the dynamic simulation of the original system resulting in a dramatic reduction of computation time while not losing flexibility and accuracy. The previous mentioned research showed how promising could be the neural networks in the areas of design, analysis, simulation, and control of MEMS devices. In the following paragraphs a brief description and classification of the different networks architecture and their principles of operation are explained.

5.3 Neural Network Principles

The basic building element of a neural network is referred to as neuron or processing element (PE). A general model for a neuron is shown in Figure 5.1 at page 104. The general neuron has a set of *p* scalar input and one fictitious or internal constant input called bias *b*, which has a constant input of 1. The input elements X_i of scalar input *p* are transmitted through connections that multiply their strength by the scalar weight *w* to form the dot product *wp*. This product is summed with the bias forming the net input *n*. This net input is then passed on to an activation function or sometimes called transfer function *f*, which produces the scalar output *a*. The transfer function net input *n* again is a scalar. The transfer function takes the argument *n* and produces the output *a*. This transfer function produces a scalar value of either zero or one. Another type can produce either minus one or one. One of the most common transfer functions is the sigmoid. Other common transfer functions include tan-sigmoid, linear, radial basis, and step (hard limiter) function. Figure 5.2 at page 104 shows description for those functions.

w and *b* are both adjustable scalar parameters of the neuron. The central idea of neural networks is that such parameters can be adjusted so that the network exhibits the desired interesting behavior. Thus, we can train the network to perform a particular task by adjusting both of the weight and bias parameters, or perhaps the network itself may adjust these parameters to achieve the desired results.

In general, neural network consists of many neurons repeated in the form of layers that construct the body of the network. Those neurons are interconnected in many possible topological ways. These topologies can include "single-layer" and "multi-layer" networks. The layer where the input vectors are presented is referred to as the input layer and the output layer is where the outputs are formed. A "single-layer" network actually has both the input and output layers, whereas "multi-layer" can have one or more hidden layers in between.

These hidden layers are so called because their inputs and outputs are only used for internal connections and are unavailable to the outside world. Figure 5.3 at page 105 shows different architectures of networks include "single-layer" and "multi-layer" networks. If the direction of transferring data between neurons is in one direction, the network is known as Feedforward network. On the other hand, if the neurons exchange data between them in both ways, the network is known as Feedforward/Feedback network. For each layer all neurons computations and operations can occur simultaneously. Every layer is fed with data generated previously from either a preceding layer, or from itself. ANN's can be designed to work either synchronously or asynchronously. When working synchronously all the neurons in a layer compute simultaneously and then pass on their outputs to the next layer at the same time. For asynchronous operation, each neuron passes its output to the next set of inputs after it has computed it.

5.4 Neural Networks Classification

Neural networks can be classified into three main types according to the learning algorithm or learning type; however, there are other types and numerous variants within these three. The following paragraphs describe briefly the different learning algorithms and give some examples from the literature.

5.4.1 Supervised learning type

In supervised learning, ANN's are trained to perform a task by a "teacher". It repeatedly showing them representative examples of the inputs they will receive paired with the desired outputs. During each learning or training iteration the magnitude of the error between the desired target and the actual network output is computed and propagated back through the network architecture. This process is done in order to make adjustment to the internal network parameters or weights and biases. according to the learning algorithm used. This course of action that is known as training cycle, or (epoch).

This cycle is repeated over and over until learning complete. As the learning proceeds the error is gradually reduced until it achieves a minimum or an acceptable preset small error value. Figure 5.4 at page 106 shows a schematic for the supervised learning scheme. Supervised learning type is applied to many networks architecture such as, multi-layer Feedforward Preceptron networks, Boltzman Machine, Radial Basis Function network, Probabilistic neural network, and General Regression neural network Also, used for Feedback networks such as, Brain-state-in-a-box and Fuzzy Cognitive Map.

5.4.2 Reinforcement learning type

Reinforcement Learning (RL) is learning through direct experimentation. It does not assume the existence of a teacher that provides examples upon which learning of a task takes place. Instead, in the RL experience is the only teacher [79-81].ANN's that learn by reinforcement do not need to compute the exact error between the desired target and the actual network output, rather for each training example the network is given a pass/fail signal. If a fail signal is assigned, the network continues to adjust its parameters until it achieves a pass. If does not fail, it continues for a predetermined number of tries, whichever comes first. One of the common applications for the RL algorithm is the use of Reinforcement Learning Algorithms (RLA) in ATM networks and in Traffic Control of High Speed Networks, such as Broadband ISDN [82].

5.4.3 Self-organising (Unsupervised learning) type

Self-organising ANN's takes example of the inputs and form automatic inter groupings or clusterings of the input data based on some measure of closeness or similarity. Because of this unique ability, these types of networks are used in classification problems [83], and categorization as well. Self-organising learning type [84] is applied to many networks architecture such as, Kohonen networks, Fuzzy Associative Memory, Counterpropagation network, Adaptive Resonance Theory [85], Hopefield neural network, and Bi-directional associative memory.

5.5 Creating the Neural Network

In the current study, a Feedforward Backpropagation neural network is applied to calibrate the FE results of the VRM method based on the FE results produced by the

EFM method. Using the advantages of ANN's mentioned above, after careful selection of the network architecture and training with the proper FE data, this network will be able to predict and approximate the relation between both FE results.

Selection of the proper network architecture is achieved through a parametric study. In this study, a preliminary architecture is suggested, and the key elements of this architecture include the number of hidden layers, size of those hidden layers, the transfer functions corresponding to hidden layers, the training algorithm, and number of training cycles (epochs). The inputs for this network are derived from the comb-drive design parameters, and the desired network target is the Von-Misses stress ratio of both FE results for network number one and displacement ratio for network number two.

Table 5.1 at page 105 shows the values of the network input for both networks. Figure 5.5 at page 106 illustrates the general Network architecture of multi-layer Feedforward Backpropagation neural network that was implemented in this study, featuring the network components as input layer, hidden layer/layers, and output layer. The neural network toolbox of the commercial package Matlab was used to create the network.

The proposed network for Von-Misses stresses is composed of one input layer with 5 inputs representing the varied comb-drive design parameters, two hidden layers with 8 and 5 neurons respectively, and finally the output layer with one neuron. In this case, a sigmoid transfer functions is used in the input layer and in the hidden layers and is followed by a linear transfer function in the output layer.

The sigmoid transfer function used is a tan-sigmoid function while the linear function is purelin. The architecture of the displacement network consists of one input layer with 5 inputs, two hidden layers with 9 and 5 neurons respectively, and finally the output layer with one neuron. The sigmoid transfer function used is tan-sigmoid while the linear function is purelin as in the case of Von-Misses stresses network. The available data set was divided into 3 equal components; one of the components was used for validation of the network, and the other two were used for training the network.

5.5.1 Network Model key elements

Multi-layered Feedforward neural networks represent a special form of connectionist model that performs a mapping from an input space to an output space. When the hidden layers have a nonlinear activation function such as sigmoid function, the mapping is nonlinear. The Backpropagation network is based on the Widrow-Hoff learning rule, which is based on an approximate steepest descent procedure. Specifically, the mean-squared error of the network approximation is calculated using the squared error at each iteration during the learning process [86]. The learning rule is consequently applied to the network to change the values of the weights and biases of the network after each successful epoch (one cycle of training) in order to minimize the difference between the network target and output. The term "Backpropagation" refers to the method used in determining the gradient of the performance function, along which the network's weights are moved. These types of networks are typically successful in approximating functions when trained on a data set that is representative of the ranges the network should be expected to predict.

5.5.1.1 The Hidden Layers

In creating the general architecture of the network, the number of hidden layers has to be specified, as well as the associated activation functions for them. For preliminary investigations, one hidden layer was used containing 5 neurons. The transfer function chosen for the hidden layer was chosen based on the learning rule (training function). This training function, which is known as trainbr is only able to accept input values ranging from -1 to 1. Therefore, the sigmoid layers of the network have a tan-sigmoid (tansig) transfer function. This function is differentiable between the limits of –1 and 1, and is continuous in this range; the use of this function enables the network to represent any complex nonlinear relation between inputs and outputs. Linear transfer function is chosen for the output layer of the network, as the output values should linearly correspond to the computed values in the network.

5.5.1.2 Learning Rule (Training Function)

One of the common problems associated with neural networks is overfitting. Overfitting refers to when the network memorizes the training data, thus lowering the error during training. However, when the network is presented with new data, its error is often larger. This happens because the network has not learned to generalize the function well. By incorporating a technique known as regularization, the likelihood of overfitting diminishes. In general, regularization modifies the performance function, which is typically chosen to be the sum-squared error of the network. If the performance function is changed to include the sum of the weights and biases of the network, the training of the network will minimize the error as well as the accompanied weights and biases. The net effect is a smoother network response [86]. Manually controlling the regularization of the network is a difficult task. Thus training function, trainbr, is used to automate the regularization process. This course of action is known as Bayesian Regulation framework

[87]. While several training algorithms are available at Matlab, the majority of literature reports lean toward using trainbr as the best algorithm for function approximation [88].

5.5.1.3 Data pre-processing and post-processing

Neural network training can be made more efficient if certain preprocessing steps are performed on the network inputs and desired targets. The trainbr algorithm generally works best when the network inputs and targets are scaled or normalized so that they fall approximately in the range of -1 to 1. The function *premnmx* is used to scale both of the input data, and the desired target data to the required range of -1 to 1. This function returns two variables referred to as *mint* and *maxt*, contain the minimum and maximum values of the original targets. After the network has been trained, these variables should be used to scale any future inputs that are applied to the network. The function *postmnmx* is used to convert the network output back into the original target data scale using the two variables mentioned previously. Whenever the trained network is simulated using new inputs, the original scale that were computed for the training set should be use (mint and maxt). The function *tramnmx* is used for that purpose.

5.6 Results and Discussion

In order to calibrate the FE results of the (VRM) method, the neural network structure has to be optimized for maximum network reliability and minimum error. Therefore, network architecture is investigated to assure good generalization and prevent over-fitting. One method for improving network generalization is to use a network that is large enough to provide an adequate fit. The larger the network used, the more complicated the function created by the network and the increase the likelihood of over-fitting this function. So, the desired network should be as small as possible, which will provide good generalization, but in the same time not too powerful to over-fit the data. Network parametric study includes, the effect of number of neurons, number of training cycles (number of epochs), and finally the number of hidden layers. Based on controlling those parameters, optimized network architecture can be obtained. In addition, network performance is measured in terms of network mean absolute error and correlation coefficient.

5.6.1 Effect of the Number of Neurons

The effect of the number of neurons in the hidden layers was investigated. This effect was measured as a function of the network mean absolute error (MAE) and the correlation coefficient (R) of the network. The higher the network correlation coefficient, the closer the network output results are to the desired targets, and hence the more accurate the network fitting. Starting with one hidden layer with five neurons and then increasing the number of neurons. Figure 5.6 at page 107 show the network performance as a function of mean absolute error for one hidden layer with several numbers of neurons.

Although the network performance is theoretically improves while increasing the number of neurons, this is not necessarily true. By adding more neurons, the network becomes more powerful and able to approximate the function more accurately. However, the chances of overfitting are increased. It is clear that beyond 15 neurons the network began to memorize the data as the error start to increase on the validation and training data sets. So, the optimal number of neurons for a single hidden layer is 15 neurons.

In order to, test the network performance in terms of good fitting, regression analysis should be performed. Regression analysis measures the correlation between targets and outputs, by calculating a coefficient of correlation (R). Figure 5.7 at page 107 shows those values as 0.868 for the training set and 0.682 for the validation set. It is clear that the value for the validation set is lower suggesting that the network is not yet powerful enough to generalize well. Thus the addition of another hidden layer that contains more neurons is needed.

5.6.2 Effect of number of training cycles (number of epochs)

Another important network parameter that can affect the network accuracy is the number of training cycles. Figures 5.8 and 5.9 at page 108 illustrate the effect of the number of training cycles on the network performance as a function of the network mean absolute error and correlation coefficient respectively. To investigate the effect of this parameter on the network performance, the previous architecture including the optimal number of neurons was used. The number of epochs was varied from a value of 100 to 700 epochs, and the network performance was measured.

As shown, the network best accuracy was evident at 500 epochs, at this point the mean absolute error for the training data set is 2.5%, and 10.1% when simulated with the validation data set. Despite the fact that increasing the number of training cycles improves the network accuracy, training the network at larger number of epochs than 500 can lead to overfitting problems, and the network starts to memorize the input data as the error on the validation data set increases. Typically, this early stopping criteria is used to determine the point at which network training stops.

Figure 5.9 illustrates, that at 500 epochs the correlation coefficients for the training data set and validation data set are 0.99 and 0.765 respectively. Although, this value for the training data set is quite good, but the other value for the validation data set is still low.

In order to improve that value the ability of the network to generalize well needs to be improved, this can be done by using two hidden layers instead of one. This improves the network efficiency and the ability to predict the function in a good manner.

5.6.3 Effect of number of Hidden Layers

By increasing the number of hidden layers, the network is theoretically able to approximate more complex functions. The more layers (i.e. neurons) available in the network architecture, the more correlations can be made between input data and resulting output data; and the more powerful the network becomes in predicting and approximating the function. In theory, this concept suggests that by increasing the number of hidden layers, the performance of the network also improves. Figure 5.10 at page 109 shows the different combinations of the new 2-hidden layers network architecture. It also shows the variation of the calculated mean absolute error for each corresponding layer size.

Using the suggested number of epochs that was determined by the parametric study, new network architecture with two hidden layers was used. The network is varied in size first by keeping the number of neurons in the second layer the same as of 2 neurons. Several runs are made for the first layer of size 4 to 12 neurons. Second, the size of the first hidden layer that matches the best network performance is kept the same at 9 neurons, and the size of the second layer is changed. For the second layer, several runs are performed for layer size ranging from 3 to 7 neurons. As shown, the network is found to perform optimally when the first hidden layer contains 9 neurons, and the second hidden layer contains 5 neurons. Figures 5.11 at page 109 and figure 5.12 at page 110 show the Final network performance as the new network architecture and the number of neurons in each layer was investigated. The optimal number of training epochs based on that new architecture is also investigated and was found to be of 300 epochs.

With a 9 neurons first hidden layer size, and 5 neurons second hidden layer size, the mean absolute error was determined to be 5.48% for the training data set, while that found for simulation with the validation data set was 8.5%. In general, the network performance is improved as more neurons are added as illustrated by the training data set. It is evident that beyond a certain number of neurons the network becomes powerful enough to over-fit the data as the error on the validation set starts to increase, for this reason 5 neurons is chosen for the second hidden layer. To test the final network, regression analysis was carried out again and it returned R-value of 0.974 for the training set and 0.885 for the validation set.

5.6.4 Final Network

After the completion of the parametric study, the most suitable network was obtained. This network consisted of two hidden layers with tan-sigmoid activation functions and output layer with one neuron with purelin activation function. The size of the hidden layers was 9 and 5 neurons respectively. The network was trained with two third of the total available data and was trained for 300 epochs. One third of the available data was used for network validation. This is the network architecture for the displacement ratio network. Similar network architecture for Von-Misses stress ratio network was developed, except that number of neurons in the first hidden layer was 8 neurons.

Figure 5.13 at page 110 and Figure 5.14 at page 111 show the target data supplied to the networks against the predicted networks output for the validation set of the displacement ratio network and Von-Misses stress ratio network respectively. These figures demonstrate that the neural networks can generalize well and the predicted output is in good agreement with the supplied target data [89]. This suggests that both networks developed for the displacement and Von-Misses can be used in a reliable manner to correct and calibrate the (VRM) results.

Conclusion

During the course of this work, Feedforward Backpropagation neural networks utilizing the EFM results were developed to calibrate the VRM results. In this process, the results obtained from both meshing techniques were used to train a Feedforward Backpropagation Neural Networks. In these network models, the available finite element data were divided into two thirds for training data set and one-third for validation data set. These networks showed a good generalization performance and the values of the coefficients of multiple correlations, extracted from regression analysis were quite satisfactory. These networks were shown to be reliable in predicting and calibrating the FE results of the lateral Electrostatic comb-drive actuator. For displacement ratio network, a regression analysis was carried out and a correlation coefficient (R) was found to be of 0.974 for the network training data set and 0.885 for the validation data set with 5.44% mean absolute error for the training data set and 8.5% for the validation data. For the Von-Misses stress ratio network, correlation coefficient (R) was found to be of 0.952 for the network training data set and 0.871 for the validation data set with 6.87% mean absolute error for the training data set and 9.92% for the validation data set.

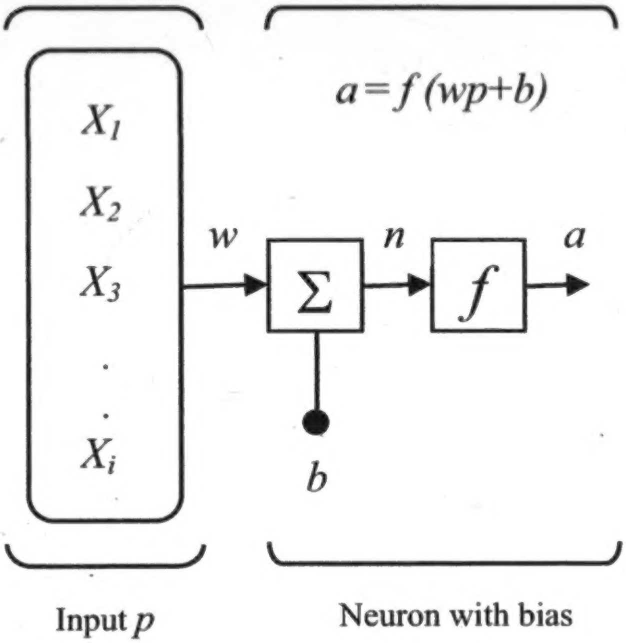
a=f (wp+b)
X_1
X_2
X_3
.
.
X_i
w
n
a
Σ
f
b
Input p
Neuron with bias

Figure 5.1: General model of neuron

Common Transfer Functions:

1) $Linear: f(x) = ax$

2) $Step\,(Hard\ Limiter): f(x) = \begin{cases} 0 \text{ if } & x < 0 \\ 1 \text{ if } & x \geq 0 \end{cases}$

3) $Radial\ Basis: f(x) = \exp(-x^2)$

4) $Sigmoid: f(x) = 1/(1+\exp(-x))$

5) $Tan-sigmoid: f(x) = 2/(1+\exp(-2x)-1)$

Figure 5.2: Common Transfer Functions for Neural Networks

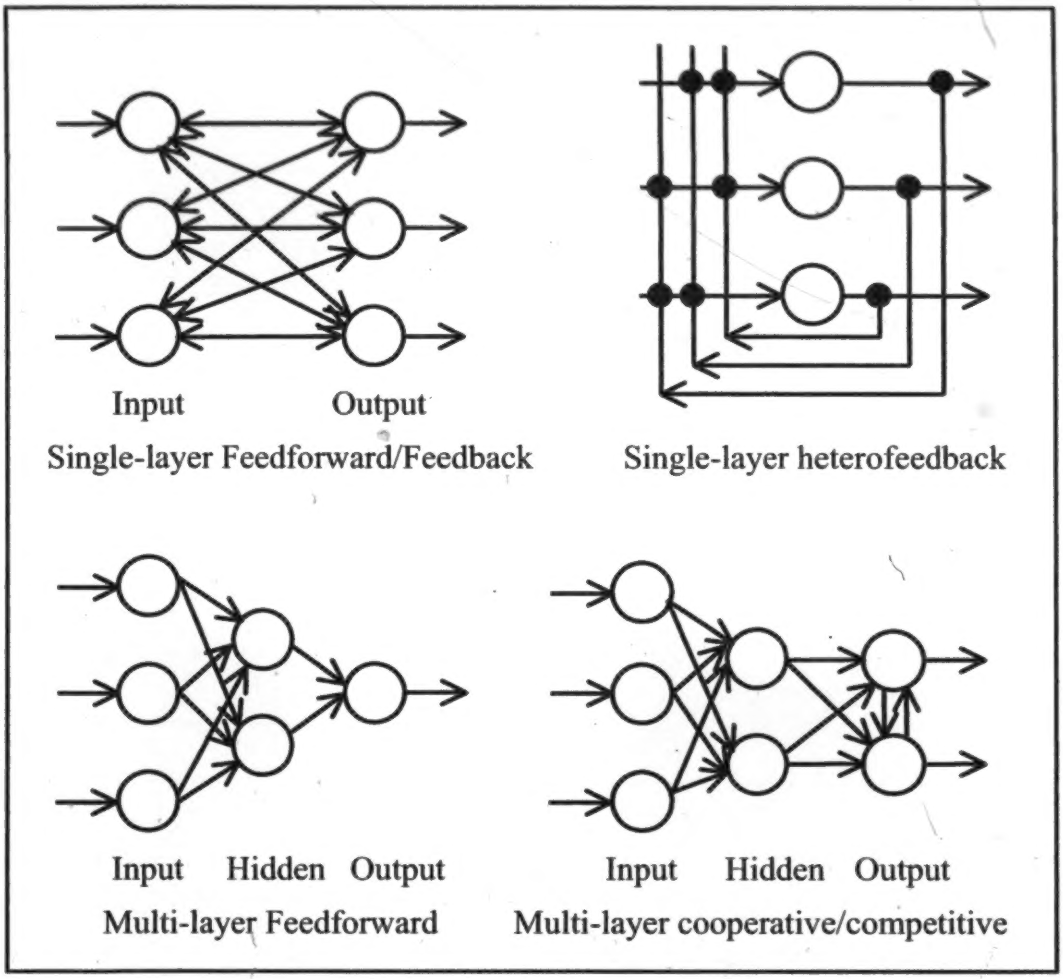

Single-layer Feedforward/Feedback

Single-layer heterofeedback

Multi-layer Feedforward

Multi-layer cooperative/competitive

Figure 5.3: Different architectures of networks include single-layer and multi-layers networks

Table 5.1: Design parameters for Comb-Drive actuator as an input to the neural network

Design Parameter	Value range
Number of Comb Fingers (n)	10 ~ 20
Finger thickness (t)	1.5 ~ 2.5 μm
Gap between Comb Fingers (g)	1.5 ~ 2.5 μm
Folded flexure spring length (Ls)	75 ~ 200 μm
DC driving Voltage (V)	10 ~ 40 Volts

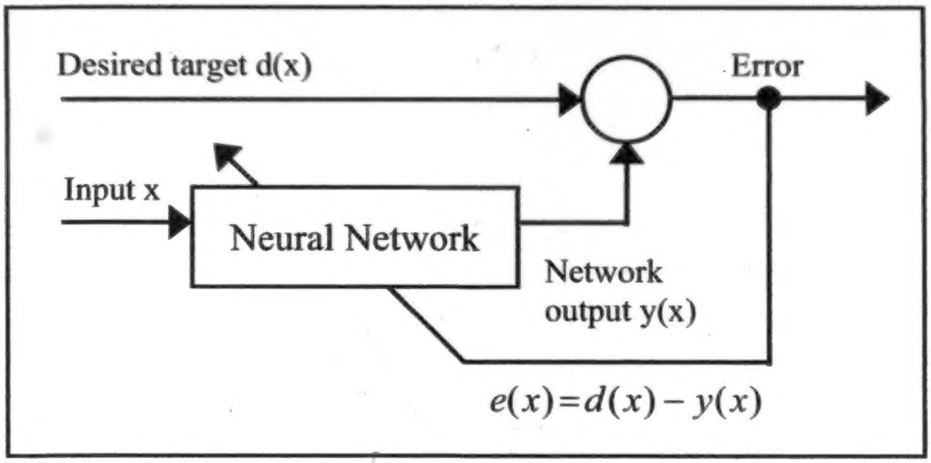
Desired target d(x)
Error
Input x
Neural Network
Network
output y(x)
$e(x)=d(x)-y(x)$

Figure 5.4: Typical Supervised Learning Scheme

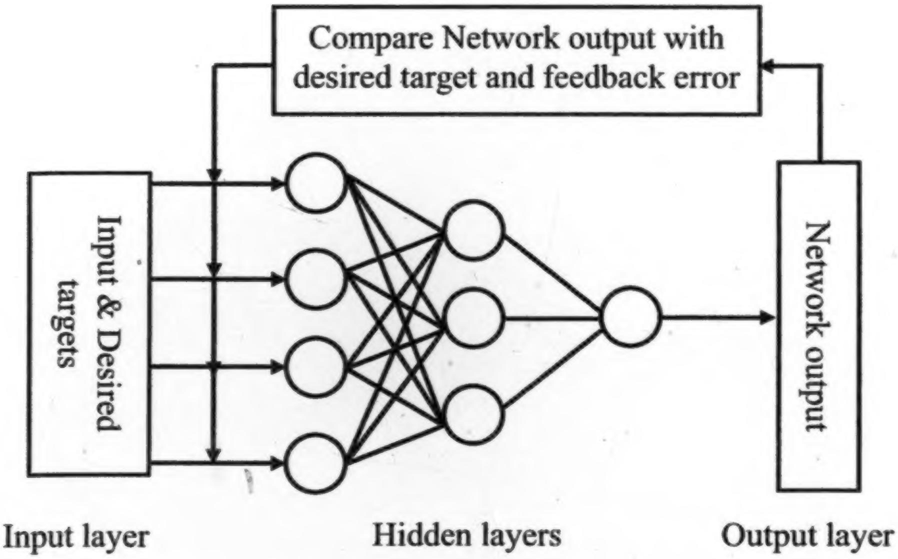
Compare Network output with desired target and feedback error
Input & Desired targets
Network output
Input layer
Hidden layers
Output layer

Figure 5.5: General architecture of Feedforward Backpropagation multi-layer neural network

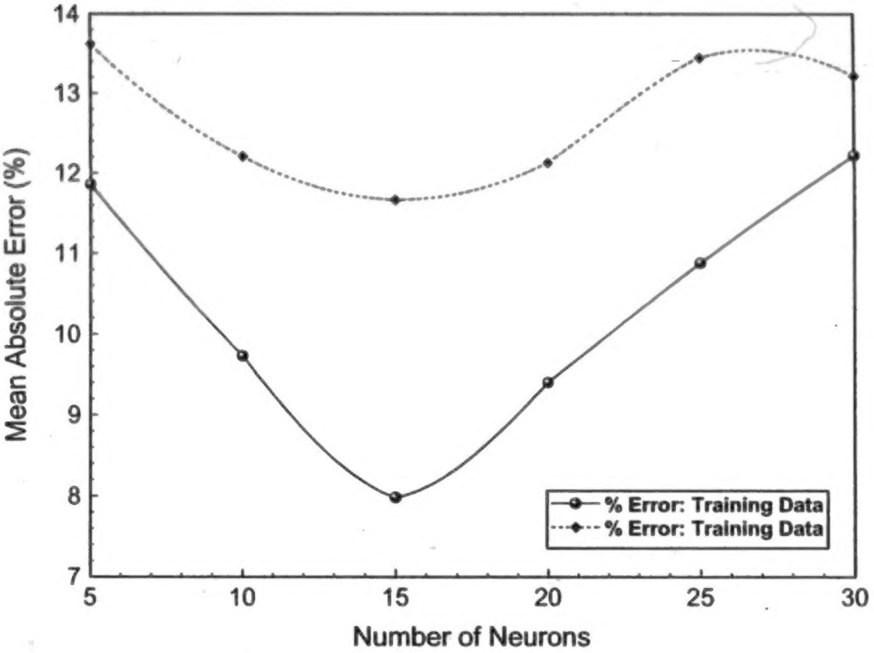

Figure 5. 6: Effect of number of neurons on network performance as function of mean absolute error

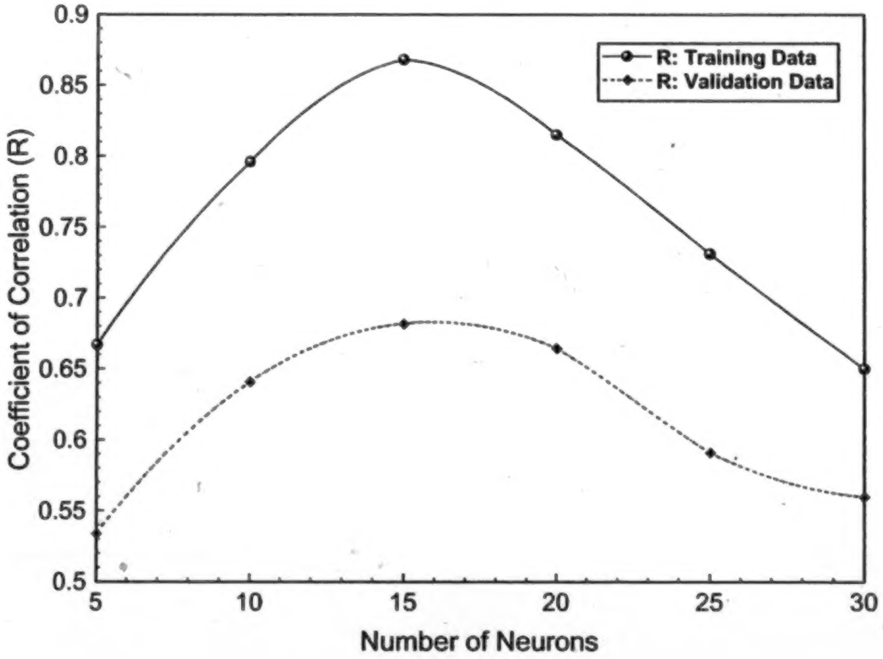

Figure 5.7: Effect of number of neurons on network performance as function of correlation coefficient

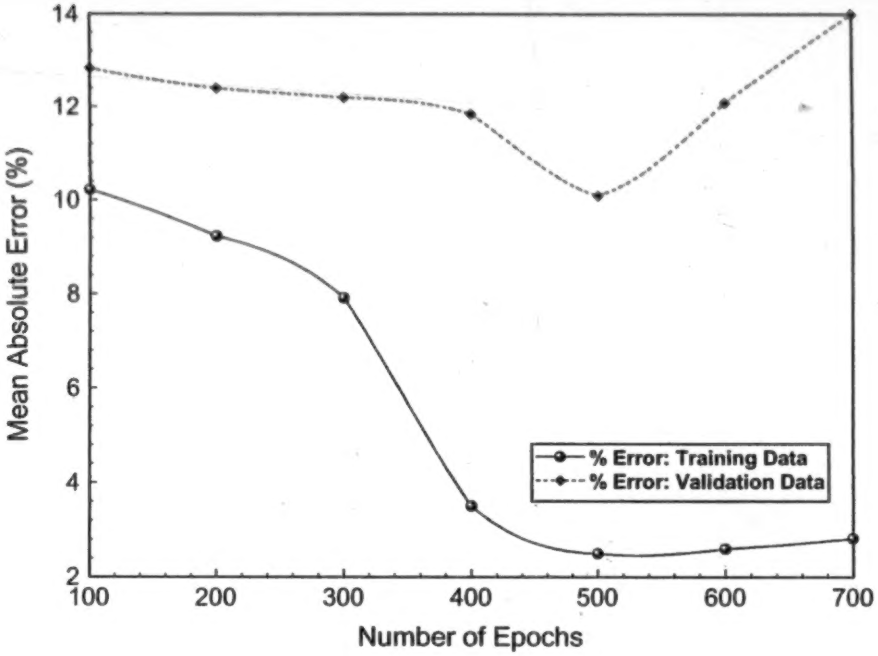

Figure 5.8: Effect of number of training cycles on network performance as function of mean absolute error

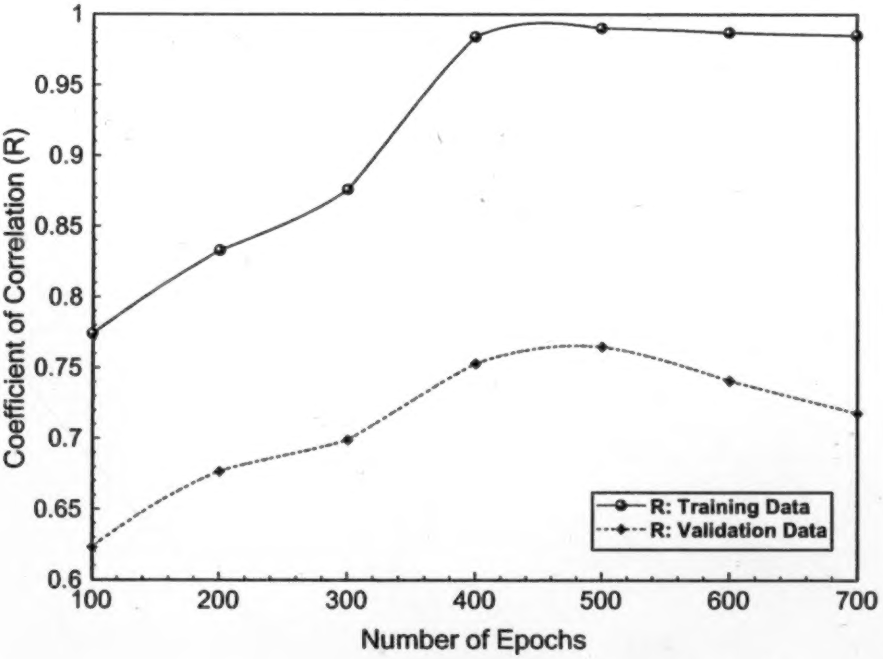

Figure 5.9: Effect of number of training cycles on network performance as function of correlation coefficient

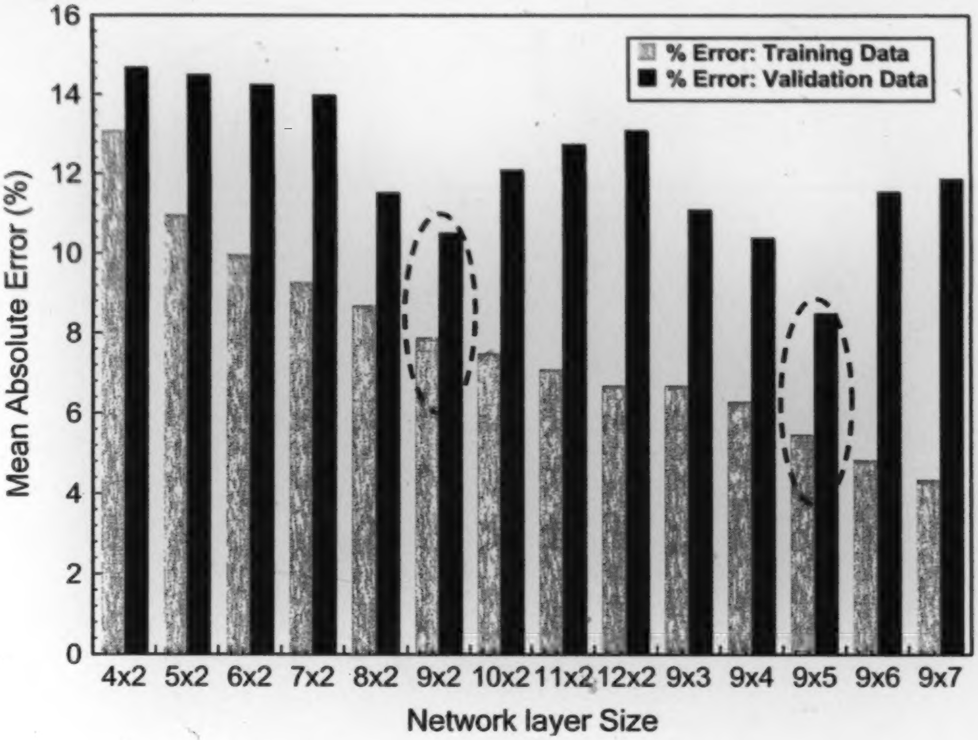

Figure 5.10: Mean absolute errors for the new 2-hidden layers network architecture

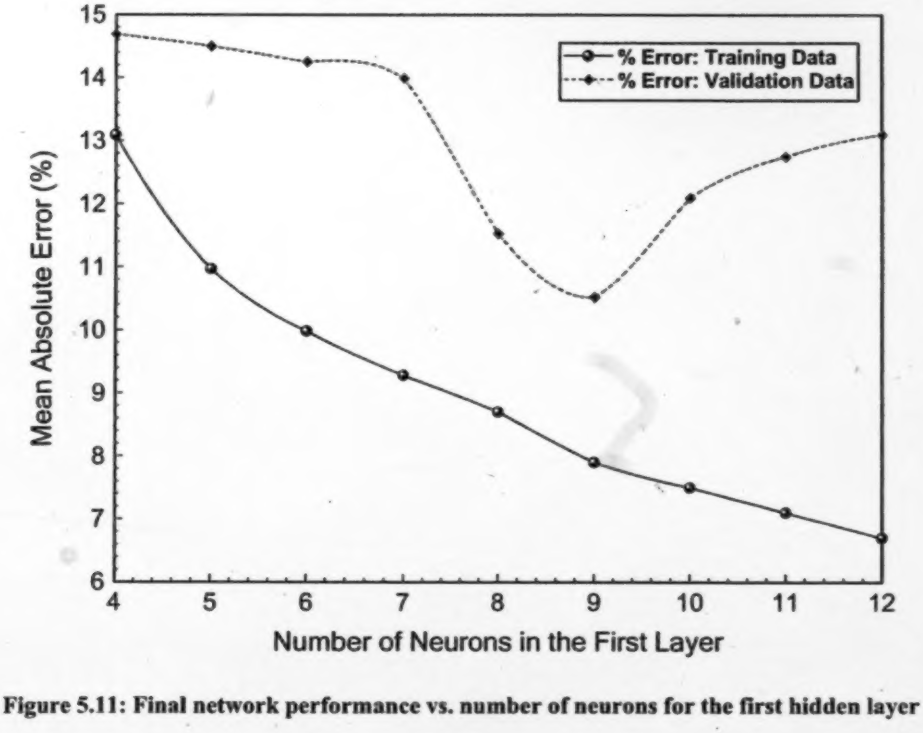

Figure 5.11: Final network performance vs. number of neurons for the first hidden layer

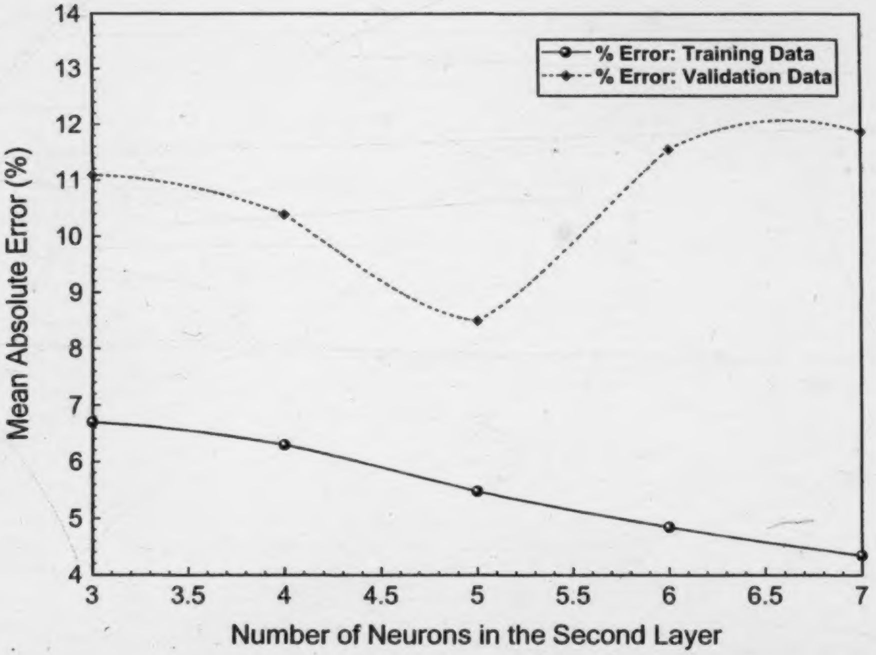

Figure 5.12: Final network performance vs. number of neurons for the second hidden layer

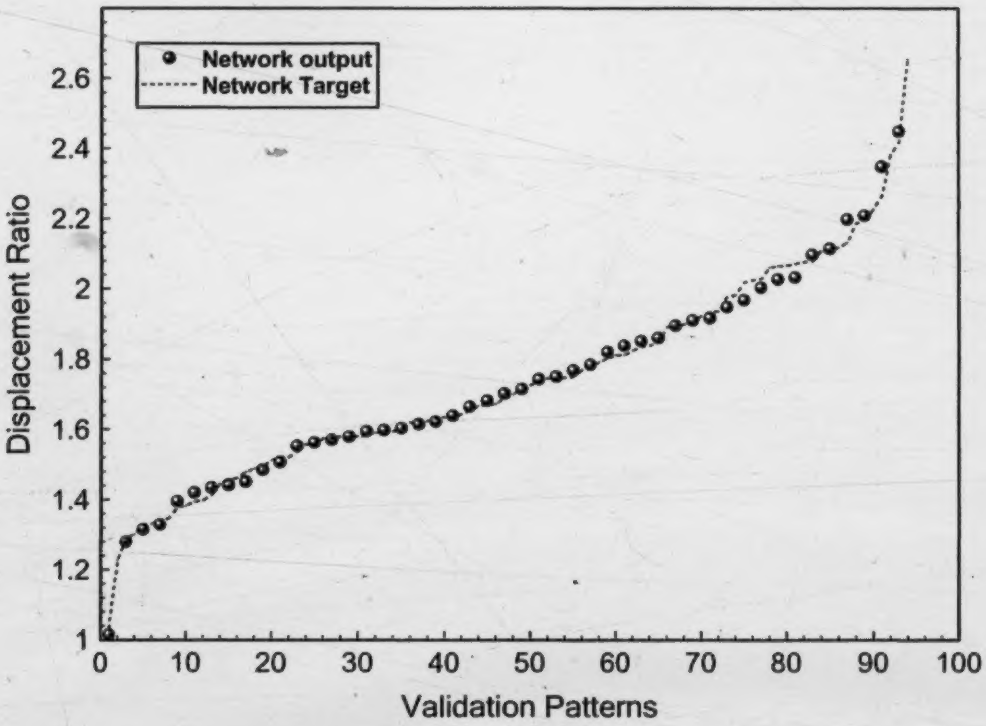

Figure 5.13: Final network output prediction vs. target data for displacement ratio network

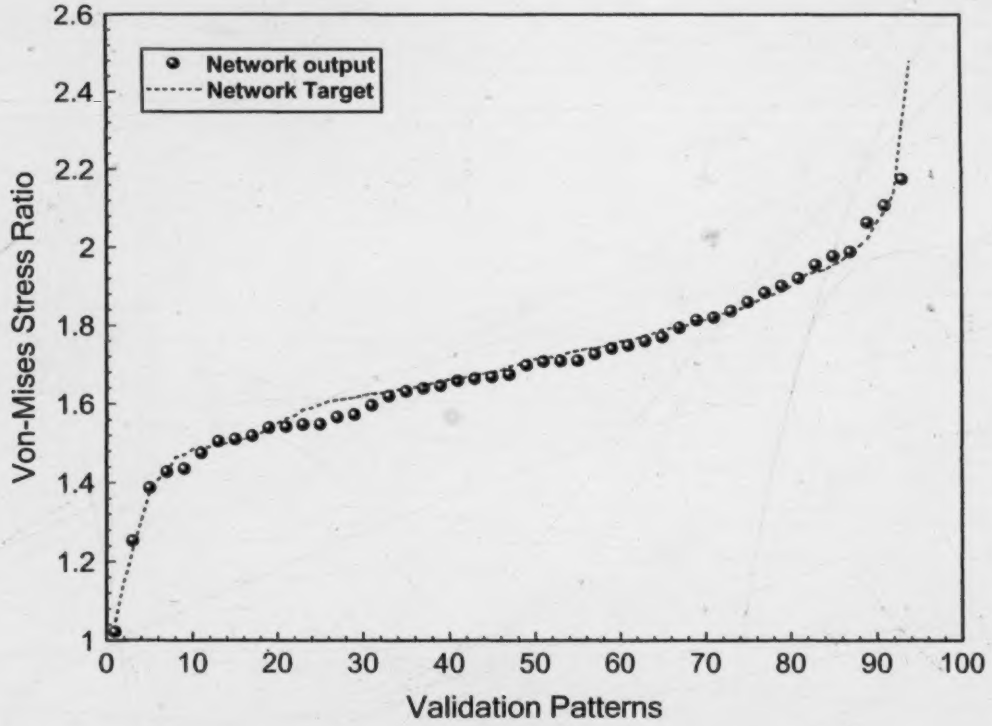

Figure 5.14: Final network output prediction vs. target data for Von-Mises stress ratio network

Chapter 6

Reliability Modeling

6.1 Introduction

In this chapter, a general overview of reliability is explained. Reliability models and different failure modes/mechanisms related to MEMS devices are documented. A particular attention to the reliability of Comb Drive actuators is considered. The reliability of this device and its lifetime is estimated by performing a dynamic analysis using finite element techniques. In addition to that, the quality factor of the device as a parameter affect its performance is investigated and is related to the device displacement based on the finite element results.

6.2 Reliability overview

In 1959, Feynman gave a famous lecture on micromachining, titled "There's plenty of room at the bottom" [90]. He discussed the possibilities of the different applications using the micromachining technology, focusing on possible future devices that might be fabricated, such as light shutters, microprobing devices for integrated circuits, 3-D devices, and data storage systems. Nowadays, not only have some of the devices he mentioned have been realized, but many more, for example accelerometers, gyroscopes, pressure sensors, valves, movable mirrors, ink-jet print heads, and hard disk drive heads. Despite the great development in the MEMS technology, still it turns out for many MEMS applications that putting them into large-scale products is more challenging than expected. MEMS technology has really been successful in only a limited number of applications, i.e. accelerometers, pressure sensors and ink-jet print heads. One reason is that the fabrication of a MEMS system involves many new tools and methods, including design, testing, packaging and reliability related issues. The early phases of MEMS fabrication are dominated by considerations of design, functionality, and feasibility. However, reliability issues that are discovered at a late phase may cause major delays in the product development going together with high costs. The need for reliability studies is becoming crucial to the success of MEMS devices especially towards the commercialization process.

MEMS reliability requires a lot of knowledge including the understanding of the properties of the new materials used in the fabrication, also complete control over the fabrication process is required to achieve a reliable MEMS device. In addition to the processes, the know-how on failure modes, the means and the procedures to perform reliability tests and consequent failure analysis are required. Unfortunately, many of those procedures for the MEMS industry are still in the phase of standardization. Fortunately, those tools/methods and procedures are in contrast with the huge amount of know-how available on reliability and failure analysis testing of IC-devices and standard IC-chip packaging. Most failure modes are well known and documented, and test procedures to follow are available and described in certain standards such as the military standards [91]. Fortunately, some of this know-how can directly be transferred for the study of MEMS and MEMS packaging. On the other hand, many key issues are unique to MEMS, i.e. those that are mainly related to the mechanical part of the structure and the packaging, and deal with failure issues such as creep, fatigue, fracture, wear, and stiction.

Reliability is defined as the probability that an item will perform a required function under stated conditions for a stated period of time. For MEMS, this definition inherently implies that the reliability specs depend highly on the intended application. For example an RF-MEMS switch that is intended for space applications might have reliability considerations different from the same RF-MEMS switch that might be intended for switching in a mobile phone. This adds another complication to the standardization of the reliability procedures. For those reasons, many researchers were motivated in the last few years to focus their research efforts on reliability studies. These studies become more and more important to the design process of MEMS devices.

A special attention is considered for the reliability of electrostatic Comb Drive actuators, as they are the most commonly used actuators among their counterparts. The next few sections of this thesis discuss the basic reliability models; the different failure modes/mechanisms associated with the MEMS devices and the physics behind them with emphasis on the application of Electrostatic Comb Drive actuators. And the last part of this work will study the expected lifetime of the comb drive based on a certain operation conditions. This study is conducted through performing a dynamic analysis at the resonance frequency using commercial finite element application IntelliSense$^{\text{TM}}$.

6.3 Reliability Models

Reliability can be understood as the probability that an item will perform its required function for a set amount of time. Reliability is also a measure of the rate at which things fail. The complementary failure and reliability rate functions for a system operating at time $t = 0$, and a time T as the time to failure can be defined as [92]:

$$F(t) \equiv P\{T \le t\} \qquad (6.3.1)$$

$$R(T) \equiv P\{T > t\} = 1 - F(t) \qquad (6.3.2)$$

Where P{a} is the probability that the event 'a' will occur, F(t) is the probability that a system fails in time [0,t], and R(t) is the probability that a system survives until time t.

Probability theory defines F(t) and R(t) as non-negative values. For example, if the probability of system to fail after certain time t is 30%, this means that system reliability is 70%. Several quantities are used to define the system's reliability such as Probability density function, failure rate, and reliability function. When data from a reliability test is collected, it is plotted as failure versus time. This plot is used to establish the reliability models by fitting the available data. From this model the probability density function is calculated. Probability density function is the measure of the probability of failure around a point in time t. Several probability models are often used to model failure of systems, those models describe the failure distributions versus time. Those models are:

- The Uniform Distribution
- The Weibull Distribution
- The Normal Distribution
- The Lognormal Distribution

A brief description of Normal Distribution is introduced in the next paragraph. Figure 6.1 at page 131 shows the probability density function (pdf) for the normal distribution. It is used later on to represent the distribution of the quality factor of different samples of Comb Drive actuators. Based on that distribution and the related Comb Drive performance results from the finite element analysis, Comb Drive reliability is calculated. This distribution is expressed by the following equation:

$$f(t) = \frac{1}{\sigma\sqrt{2\pi}} e^{\frac{-(t-t_0)^2}{2\sigma^2}} \tag{6.3.3}$$

Where σ is the standard deviation and t_0 is the mean time to failure (MTTF).

Simply, the reliability can be measured by submitting a large number of device samples to testing under normal operating conditions until failure occurs. However, highly reliable devices have a lifetime of several years, so this approach is often too costly and time consuming for most applications. Instead, devices are operated under accelerated conditions for a shorter period of time until failures occur and then, using probability theory, actual device lifetime is reconstructed by modeling it with one of the above probability distributions.

6.4 Failure modes and Mechanisms

Accurate study of MEMS reliability requires a comprehensive understanding of the nature of device failures in terms of its failure modes and mechanisms. Failure modes may be classified into two main distinct categories:

- Degradation failure, in this mode the device operates far enough from normal conditions that the component can no longer be trusted for reliable operation.
- Catastrophic failure, as the name implies, this mode is the complete end of the device operation.

In many cases, failure occur when the stresses on a specific device exceed its strength, in other words the failure mechanism in this case is overstresses. Due to the complex nature of the MEMS devices, more than one failure mechanism can contribute at the same time toward the device failure. In the next few paragraphs, a brief description of those mechanisms and the physics behind them are introduced. Table 6.1 at page 131 lists the common MEMS failure mechanisms [93].

6.4.1 Mechanical Fracture

Mechanical fracture can be defined as the breaking of a uniform material into two separate sections. It normally happens when the applied stress exceeds the failure stress of the structure or the tensile strength of the material. Mechanical fracture can be classified into tree types, ductile, brittle, and intercrystalline fracture. Ductile fracture is associated with ductile materials. Those materials exhibit a plastic deformation, which is signified by the necking at one specific point. While brittle fracture occurs along crystal plans and develops rapidly with little deformation. For intercrystalline fracture, it is almost like the brittle one except that fracture occurs along grain boundaries in the polycrystalline materials such as polysilicon. Since most of the MEMS materials are silicon based materials the later two types of fracture dominate.

In order to define the possibilities of structure fracture, the applied maximum stresses have to be calculated and compared with the fracture strength of the material. Since MEMS devices have often change in the cross section, stress concentration occurs and this has to be taken into consideration during calculations of maximum stresses. Stress concentration factor is a function of the geometry and their values are available in the literature. The maximum stresses can be calculated from the stress concentration factor and the average stress at a stress concentration point according to the equation:

$$\sigma_{\max} = k\,\sigma_{ave} \qquad (6.4.1.4)$$

Where $\sigma_{\max}$ is the maximum stress at a stress concentration point, σ_{ave} is the average stress at a stress concentration point, and k is the stress concentration factor.

The fracture strength of the material is limited by the defects that appear in the material due to the imperfection in the crystal growth techniques. Another type of mechanical fracture is the failure due to fatigue. Fatigue is a failure mechanism caused by cyclic loading of a structure below the yield or fracture strength of the material. This type of loading leads to the formation of surface microcracks that cause the slow weakening of the material over time and create localized plastic deformations. While brittle materials do not experience macroscopic plastic deformation, they will still experience fatigue.

Fatigue is typically modeled with a plot known as the SN curve. The plot, shown in Figure 6.2 at page 132, this plot relates the applied fracture stress, S, to the number of cycles of loading and unloading a material. The device lifetime in terms of number of cycles can be increased if the amplitude of the applied stress is decreased. Fatigue causes a gradual change in the properties of a material i.e. Young's modulus will gradually shift. This shift will change the resonant frequency of many devices. Fatigue also affect the dampening coefficient, which will increase over time and change the resonant frequency and quality factor Q of a structure [94]. The combined effect of these changes can lead to degradation failure. Later on, this plot for polysilicon is used to calculate the lifetime of the Electrostatic Comb Drive actuator.

6.4.2 *Stiction*

One of the most important and almost unavoidable problems in MEMS is stiction. Figure 6.3a and 6.3b at page 132 illustrate two scanning electron microscope (SEM) pictures for a released and stuck Comb Drive actuator. As MEMS structures are so small, surface forces can dominate all others and cause microscopic structures to stick together when their surfaces come into contact. Adhesion is caused by the van der Waals forces bonding the two clean polished surfaces of the MEMS device together. The van der Waals force is a result of the interaction of instantaneous dipole moments of the atoms. Merlijn et al. [95], Tasy et al. [96] and Maboudian and Howe [97] reviewed the in-use stiction problems and described the physics behind it. MEMS devices must be designed to eliminate any surface interactions, in order to avoid this problem.

6.4.3 *Friction and Wear*

Wear mechanism in silicon MEMS is not desirable because of its bad effect on the device life and reliability. Wear can be identified as adhesive wear, abrasive wear, corrosive wear, and surface fatigue wear. Adhesive wear is caused when one surface pulling fragments of another surface while they are sliding. Sliding motion causes the surfaces in contact to adhere to each other by surface forces. When the bonding forces break, they are unlikely to separate at the original interface, which fracture one the materials, this causes a partially worn surface and the accumulation of debris.

Abrasive wear occurs when a hard or rough surfaces slides on the top of a softer surfaces, this causes a stripping away the underlying material. The volume of a material fractured by adhesive or abrasive wear is determined by the equation [92]:

$$V_{AW} = \frac{K_{AW} F x}{3\sigma_y} \qquad (6.4.3.5)$$

Where σ_y is the yield strength of the material, K_{AW} is the material dependant wear constant, x is the sliding distance, and F is the load on the material.

In case of abrasive wear the constant K_{AW} is usually on the order of 10^{-3} to 10^{-6}. Corrosive wear occurs when two surfaces go under chemical reaction and the sliding process strips away one of the reaction products. This type of wear is common in the chemically active MEMS such as Microfluidic systems and biological MEMS, and it might cause their failure. Corrosive wear can be modeled as:

$$h_{CW} = \frac{K_{CW}\, x}{3} \qquad (6.4.3.6)$$

Where h_{CW} is the depth of wear and K_{CW} is the corrosive wear constant and on the order of 10^{-4} to 10^{-5}.

Surface fatigue wear occurs mostly in rolling applications, such as bearings and gears. Over time, the continued stressing and unstressing of the material under the roller will cause the appearance of fatigue cracks. These cracks then propagate parallel to the surface of a structure, causing material to flake off the surface. The most important consequence results from the wear mechanism is the increase of the voltage required to drive a device especially in microactuators devices. The increase in adhesion will require larger input signals to drive a device. The increase in drive signal will, in-turn, increase the force, and thus wear, on a structure and eventually the device could fail.

6.4.4 Delamination

Delamination occurs when the interface between two materials loses its adhesive bond. Pattern transfer error due to particulates on the wafer surface during the lithography fabrication process can cause Delamination. It can also arise as the result of fatigue induced by the long term cycling of structures with mismatched coefficients of thermal expansion. It can cause catastrophic effects as it might cause shorting or mechanical impedance if the material is still present on the device. Also, the mass loss due to Delamination can alter the mechanical characteristics of the device.

6.4.5 Electrostatic Discharge

Electrostatic discharge, or ESD, occurs when a device comes in contact with the human body due to improper handling. As the human body can develop an electric potential in excess of 1000V, this electric charge will be transferred to the device creating a large potential difference across it. This process is known to have catastrophic effects in circuits and could have similar effects in MEMS.

6.4.6 Parasitic capacitance

An area that is also important to consider in comb drive operation is the effect of parasitic capacitance to the substrate. Since the comb drive is a fairly large conductive surface suspended over another large conductive surface, there is a considerable parasitic effect between the substrate and the comb. While this effect can be used to produce out of plane torsional microactuators, it is often an undesirable side effect of the comb drive design. It is possible to have such a large parasitic motion that the comb drive will actually touch the substrate, which will lead to the adhesion and possibly shorting problems. In a sound design, the comb drive should be far enough removed from the substrate that the parasitic capacitance would not cause stiction. Particulates can also be problematic in comb drives. Conductive dust particles can electrically connect parts of a comb, which will short them out, producing catastrophic current flows.

6.5 Comb Drive reliability analysis

The previously mentioned failure modes are generally applicable to all MEMS devices. Electrostatic Comb Drive actuators are subjected to these failure mechanisms and modes. There have been extensive reliability studies in the literature that describe the failure modes associated with this type of actuators. For example, Miller et al. [98] identified in their published work the failure modes common to Comb Drive actuators. These failure modes are, stiction, friction-induced failures caused by improper operational methods, mechanical instabilities, and electrical instabilities. Also, Tanner et al. [99] categorize the major reliability issues concerning stiction, mechanical wear, fracture, fatigue, and shock loads.

In the following paragraphs, the author will try to highlight the possible failure modes in the Comb Drive actuators from the fracture point of view. The fracture can result from over applied stresses or due to over actuation stroke of the device (device displacement beyond permissible limit). An assumption was made for the availability of different Comb Drive samples with quality factor variation following the normal distribution, in the range of 10 to 50 with a standard deviation of 10. This assumption is used to study the variation effect of the quality factor on the device performance and is used to calculate the reliability rate for those samples based on the normal distribution probability model.

Fracture can also occur due to fatigue. In order to study the fatigue of the device and calculate the expected device lifetime, a dynamic analysis for the device at the resonance frequency was conducted using the commercial finite element package IntelliSense^{TM}. Based on the finite element results and using the S-N curve data for the polysilicon, the device lifetime was calculated.

6.5.1 Mechanical fracture

MEMS devices are normally made from brittle materials such as single crystal silicon or polycrystalline silicon. The device fails when the applied stresses exceed the fracture strength of the material. The mechanical properties of polysilicon thin films depend greatly upon the process parameters used in the deposition of these films. Tsuchiya et al. [100] reported in their published work that the mean fracture strength of polysilicon depends also on the length of the test specimen and it has been found to be in the order of 2 to 3 GPa. Comb Drive actuators, are the source of mechanical motion in many MEMS systems. They are excited either under static load condition (DC actuation voltage) and in this case they produce static deflection or under dynamic load condition (AC harmonic voltage) where they work as resonators. The last mode of operation produces vibrational motion. The developed stresses in the Comb are different in both cases and consequently, the failure mechanism will be different too. In the following paragraphs failure in both cases are investigated.

6.5.1.1 Static-actuation induced failure

Based on the discussion at section 6.4.1, a relaxation analysis (Static Analysis) was conducted for the Comb Drive. A DC voltage of 30 volts was applied to the fixed Comb fingers to calculate the static deflection and the associated maximum stresses developed in the Comb (Von Misses Stresses). This analysis assumes the Comb material to be isotropic material, which implies that Young's modulus is constant in all directions. Figure 6.4 at page 133 illustrates numerical analysis results, where the maximum stress is found to be 12.5 MPa. Its location is shown to be at the edges of the folded flexure spring beams and at the anchors of the moving Comb as shown by the red highlighted areas. The stress concentration factor was calculated based on figures available in the literature [101]. The value of this factor equals to 3. Using equation (6.4.1.4), the maximum stress at the stress concentration point is calculated and was found to be 37.5 MPa. This value is so small compared to the yield strength of the polysilicon, which is in the order of 1.2 GPa. This implies a safe operation of the Comb at this load.

The design of the simulated Comb permits a maximum displacement or actuation of 12 μm. In order to test the Comb at the maximum possible actuation range, another analysis was done at excitation voltage that produces this maximum displacement and the developed Von mises stress was found to be 150 MPa as shown in Figure 6.5 at page 133. Again shows the maximum stress at the stress concentration point is calculated and was found to be 450 MPa. This indicates that even at the most possible actuation range the Comb Drive will still function normally and safely as the applied stress is much less than the fracture strength.

If the applied voltage load is higher than the excitation voltage that produces this maximum displacement, failure could happen due to over actuation. This failure is due to over actuation or over displacement not due to over stress. The spring flexure beams could collide violently with the moving comb anchor points leading to fracture. Although this could be avoided by increasing the gap between the spring beams to extend the travel range of the comb, however another series problem could arise which is the stiction. If the applied actuation voltage is higher than the critical value corresponding to stiction, stiction could happen and lead to a complete failure due to short out in the comb as shown in figure 6.6 at page 134.

6.5.1.2 Dynamic-actuation induced failure

Operation of MEMS devices at resonance mode is favorable in many applications. It maximizes the device output in terms of displacement and velocity, but the amount of output amplification is limited by the system damping. Damping is an energy dissipation mechanism inherent to mechanical systems and could be structural (depend on device geometry) or viscous damping, which is due to the fluid or gas surrounding the device. The magnitude of amplification of the natural response of structure is quantified by the quality factor Q. it can be measured by determining the frequency range for a system at which $\delta_{out} = \delta_{max} / \sqrt{2}$, for small damped systems where the system damping ratio $\zeta \ll 1$, the quality factor can be approximated as [92]:

$$Q = \frac{\omega_n}{\Delta\omega} = \frac{1}{2\zeta} \qquad (6.5.1.2.7)$$

Where ω_n is the resonance frequency, $\Delta\omega$ is the frequency range defined at δ_{out}, and ζ is the system-damping ratio.

In order to investigate the effect of damping on the Comb Drive performance and study the reliability issues that could be related to it, an assumption was made that several samples of Comb Drive are available and their quality factor variation follow a normal distribution in the range of 10 to 50 with a standard deviation of 10 as shown in figure 6.7

at page 134. A Dynamic analysis for the individual Combs was done at the resonance frequency with different damping ratios derived from equation (6.5.1.2.7) based on the suggested quality factor distribution. An AC harmonic voltage load was applied to one side of the Comb fixed fingers in the form of $V=V_0\sin(\omega_n t)$. The voltage amplitude (V_0) was defined as 30 volts and the resonance frequency (ω_n) was calculated prior to dynamic analysis using finite element procedure. The comb drive resonance frequency was calculated by implementing a modal analysis and it was found to be in the order of 19.552 KHz. The time interval (t) was chosen long enough to ensure proper functioning of damping. Finite element analysis revealed that increasing the quality factor, which means lowering the system's damping ratio is increasing the system response. This was expected, as the quantity of system response magnification is directly proportional to the Quality factor, also increasing the Quality factor will increase the time required for the system to reach the steady state vibration. Figure 6.8 at page 135 and figure 6.9 at page 135 show this effect. Table 6.2 at page 138 lists the finite element results and shows the effect of Quality factor on the response of the system, it also lists the developed Von mises stresses. Figures 6.10 to 6.12 at page 136 and page 137 show also the Comb performance under the load of a 30 Volts DC pulse of width 30 milliseconds. These figures indicate the overshoot phenomenon that happened when a mechanical system is under pulse load. Furthermore, after a certain elapsed time the damping mechanism starts to dissipate the system energy until it reaches a stable performance state. The value of the peak displacement (overshoot displacement) depends on the damping ratio and is increased with decreasing the damping ratio as shown by the figures. Figure 6.13 at page 137 show the variation of the Comb Drive displacement with the damping ratio.

The analyzed system response data were linearly fitted as shown in figure 6.14 at page 138 and the fitting formula was calculated as:

$$X = a + bQ \tag{6.5.1.2.8}$$

Where a and b are the equation constants and equal 0.871111 and 0.384667 respectively. Using equation (6.5.1.2.8) and the normal distribution from Figure 6.7, we could develop a distribution of the system response, which is illustrated by Figure 6.15 at page 139. This distribution was used to calculate the reliability rate for the group samples of the Comb Drives. Simply, the maximum permissible displacement that permits a safe operation of the Comb Drives was marked. From that distribution any displacement value above it will cause device failure and any other value lower than the critical one will leads to safe operation. The area under the curve for the safe operation region was calculated and it was found to be of 46% of the total distribution curve area. This means that the reliability rate is 46% for those Comb samples.

6.5.2 Fatigue

The outcome of the numerical analysis is done at ideal case conditions. These results are shown at table 6.2. These conditions assume no residual stresses in the deposited film of the Comb structure, no stress gradient though the film thickness and no variation in the effective Young's modulus of the polycrystalline films. It also does not take into consideration the manufacturing variations in the flexure dimensions and the proof mass. Those variations alert the value of the effective spring stiffness and shift the Comb resonant frequency. In the following paragraphs an attempt is made to quantify the effect of those parameters on the induced stresses in the Comb. In order to predict the Comb lifetime, the modified state of stress that could match the real fabricated device will be used.

6.5.2.1 Comb Drive Dimensions

Comb drive actuators can be fabricated using different processes such as Multi-User MEMS Process (MUMPs^{TM}) or Ultra-Planar Multi-Level MEMS Technology (SUMMiT). Those processes have relative inaccuracies in their lithography, etching, and deposition fabrication steps. For example, the tolerance for the individual layer thickness after deposition is reported to be approximately 0.15 μm for a polysilicon layer of 2 μm thickness. Those tolerances can be found in the MUMPs^{TM} Design Handbook [102]. This suggests about 15% reduction in the layer cross-section, which increases the stress level by about 15 to 20%. In addition to that, over-etching can lead to variations in the smoothness and angle of the sidewalls of the spring flexure resulting in trapezoidal cross sections. Muller et al. [103] reported in their published review a reasonable estimate for this variation of ±10% for patterned and etched 2 μm-thick polysilicon beams. This can easily alert the spring stiffness of the structure and affect the induced stress levels by a factor of 1.10 to 1.15, depending on the severity of the situation.

6.5.2.2 Young's Modulus

Recent research has shown that the Young's modulus of polysilicon films is highly dependant on the deposition conditions and range between 140 to 210 GPa [104]. This could lead to another stress increase factor by about 30% of the ideal condition.

6.5.2.3 Residual Stresses

Residual stresses play a major role in the successful use and reliability of MEMS devices. In many devices with freestanding structures, residual stresses can wrap the device to a degree that the structure either curls upward or touches the substrate causing device failure. For example, in micromirror arrays, residual stress gradients can destroy the flatness of the mirror surfaces making them unusable or reduce reflective efficiency. With a non-uniform doping profile, residual stress gradients are present. With additional doping and high temperature annealing, the residual stresses can be reduced. Residual stresses in polysilicon films were reported to vary from (-300 to 400 MPa) depending on the deposition temperature and pressure [92, 105]. This level of stress can be added to the induced stresses causing a stress level increase in the device by a factor of 2 to 2.5 depending on the value of the inherent residual stresses.

The previous mentioned factors could lead to the assumption of an approximate correction factor of 3.0 to 3.5 that can be used to modify the finite element results at table 6.2. For example, for case number 5 the Von Mises stress will be on the order of 1890 to 2360 MPa instead of 527 MPa. Taking into consideration all these correction factors, the overall stress can be approximated to simulate the actual condition of the real fabricated device. S-N curve reported in the literature [106] was used to estimate the lifetime of the Comb Drive actuator. This study suggests the endurance limit for test specimen of cantilevered polysilicon beam subject to cyclic stress to be in the order of 2 GPa at life of 10^9 cycles. Using this data to construct the constant-life fatigue curve, which is referred to as Goodman's curve [101] and the S-N curve, the device life was estimated to be approximately $5x10^8$ cycles as illustrated by figure 6.16 at page 139.

6.6 Conclusion

During the course of this work, general overview of reliability issues related to MEMS devices were discussed, with particular attention to the lateral electrostatic Comb Drive actuators. Reliability models and different failure modes/mechanisms were explained. Both dynamic and static analyses were performed to evaluate the reliability of Comb Drive. Static analysis results showed a safe operation even at the maximum actuation range. Dynamic analysis results in conjunction with S-N data for polysilicon were used to estimate the Comb Drive lifetime. Comb Drive lifetime was found to be of $5x10^8$ cycles. In addition to that, the quality factor of the device as a parameter affect its performance was investigated and related to the device displacement based on the dynamic analysis results. Reliability rate was found to be 46% for assumed group of Comb Drive samples.

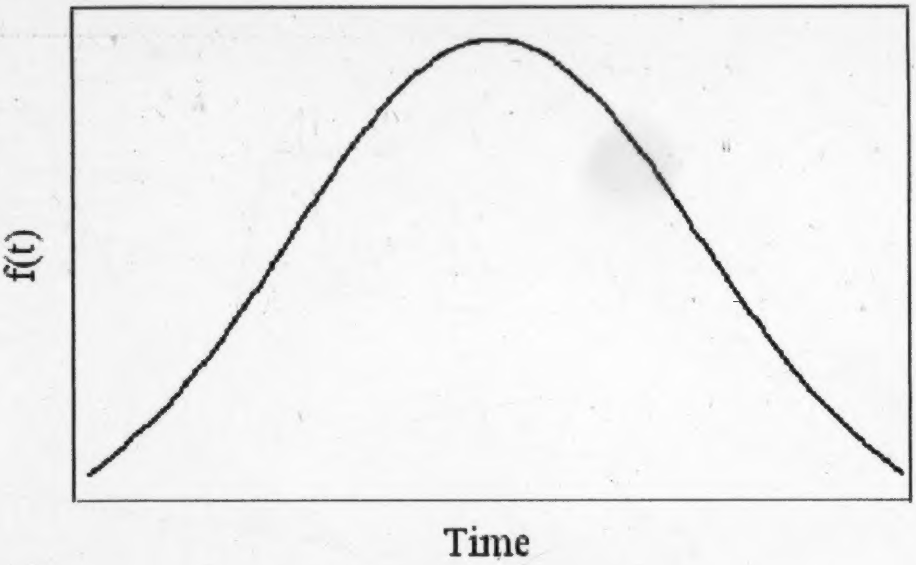

Figure 6.1: pdf of the normal distribution.

Table 6.1: Common MEMS failure mechanisms

Mechanical Fracture
Creep
Stiction
Electromigration
Wear
Degradation of dielectrics
Delamination
Contamination
Electrostatic discharge

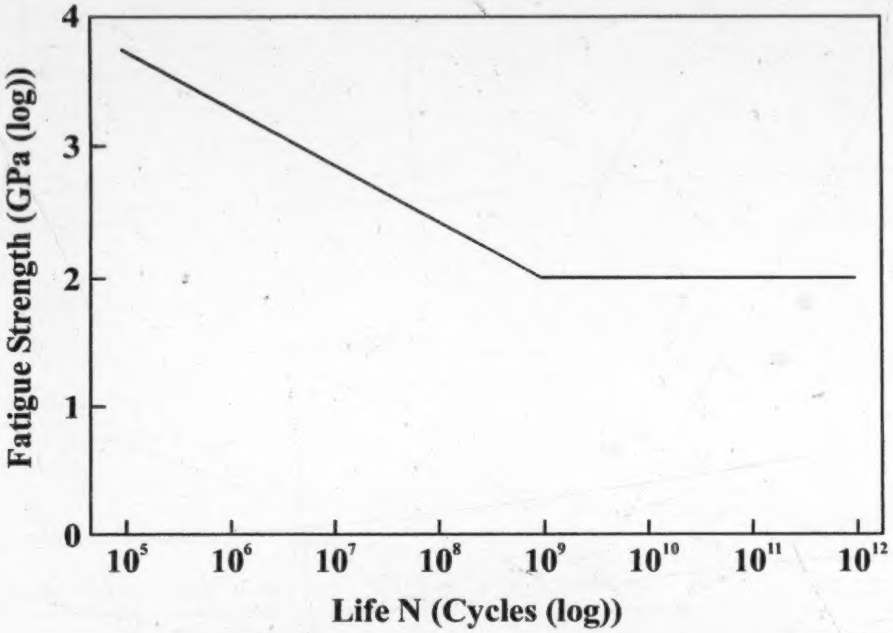

Figure 6.2: Typical SN curve for a brittle material.

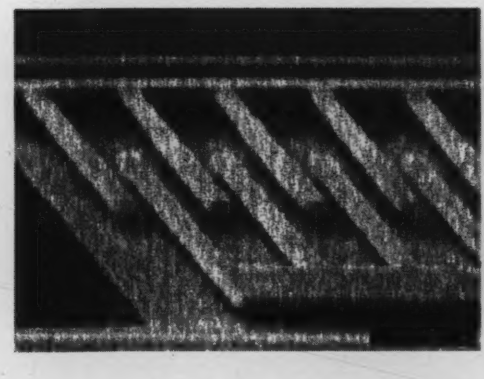

Figure 6.3a: SEM picture of released Comb Drive (courtesy of IMEC).

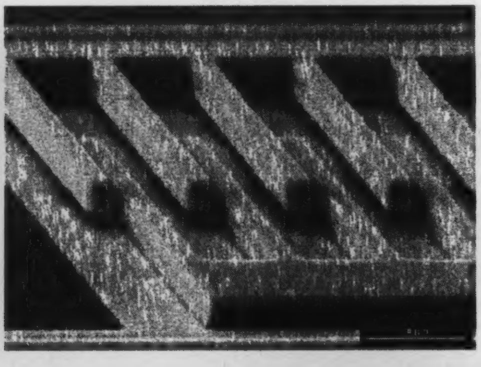

Figure 6.3b: SEM picture of a stiction failure of Comb Drive (courtesy of IMEC).

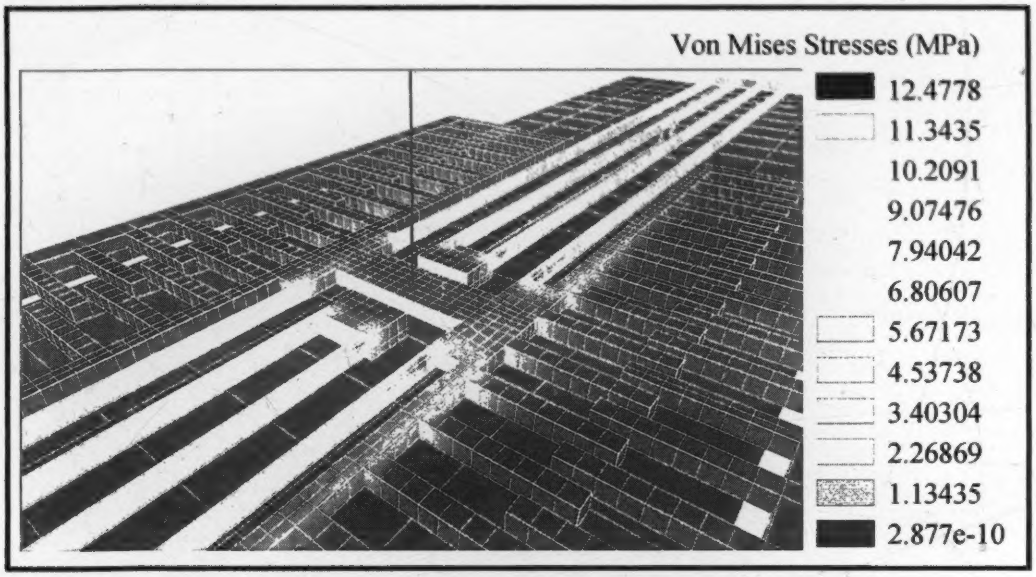

Figure 6.4: Von mises stress distribution for Comb Drive at 30 DC Volts load

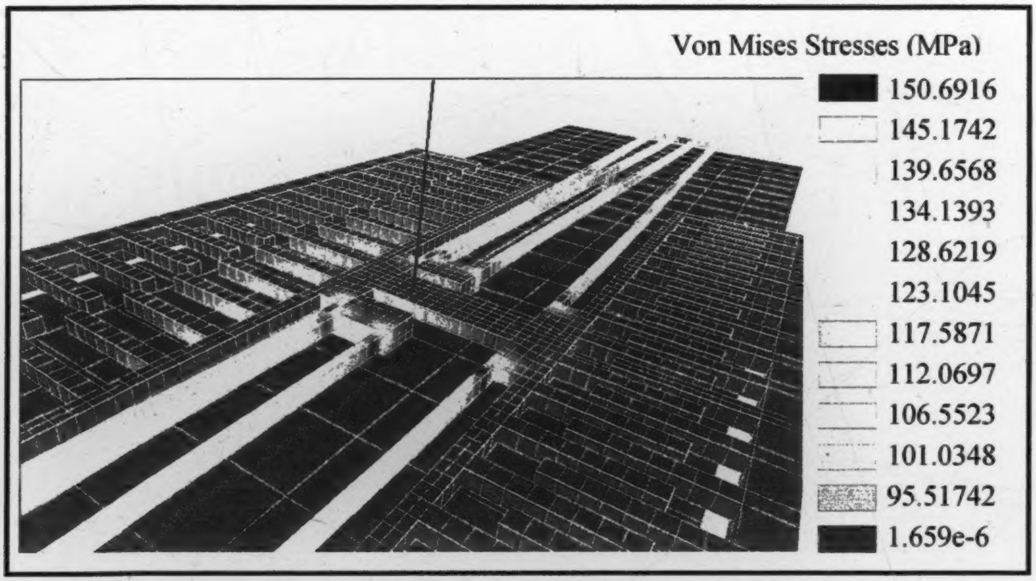

Figure 6.5: Von mises stress distribution for Comb Drive at maximum actuation range

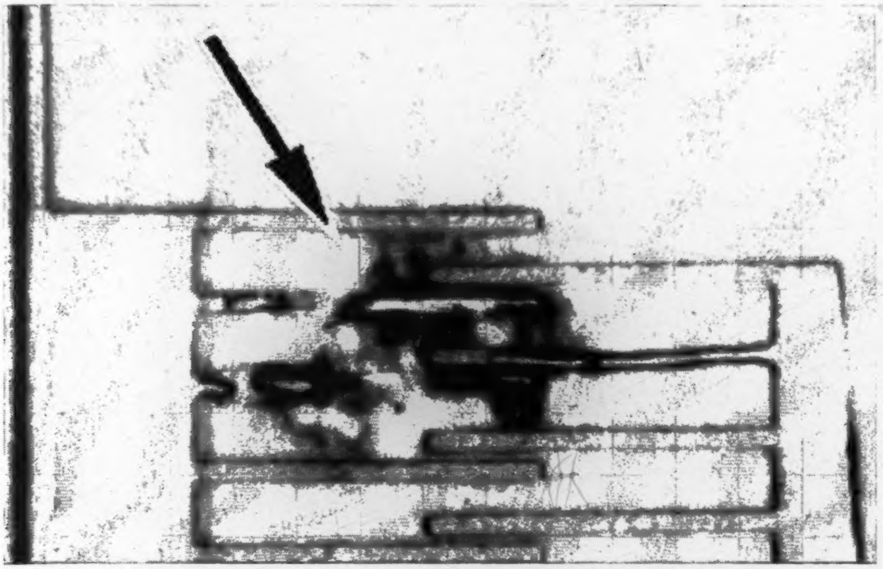

Figure 6.6: Comb Drive failure when two fingers come into contact and short out the device

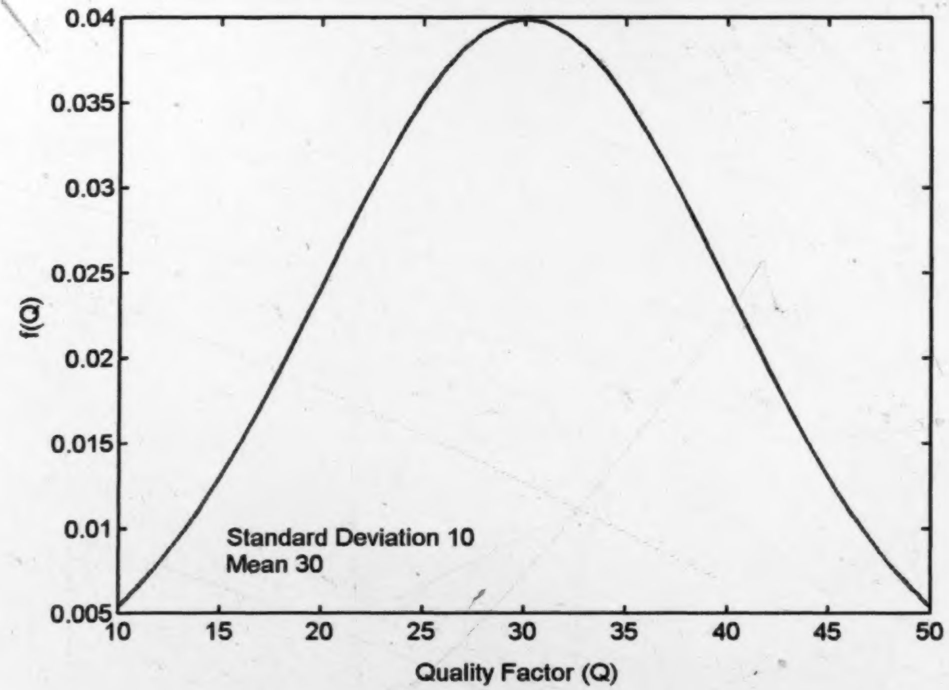

Figure 6.7: Normal distribution of the Quality factor for Comb Drives

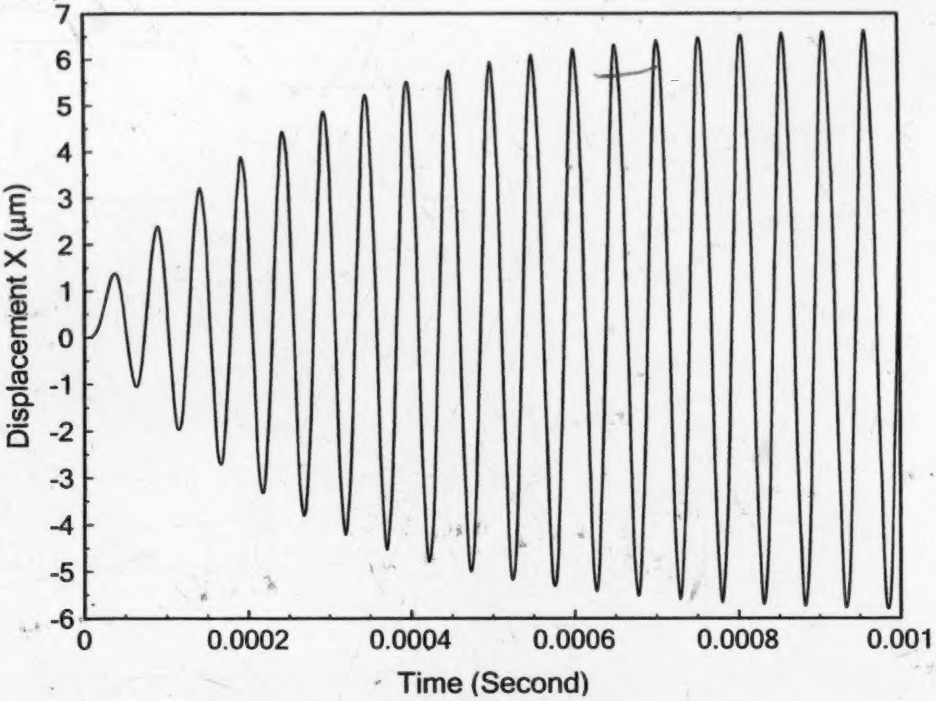

Figure 6.8: Effect of damping on Comb Drive performance at quality factor 15 during resonance

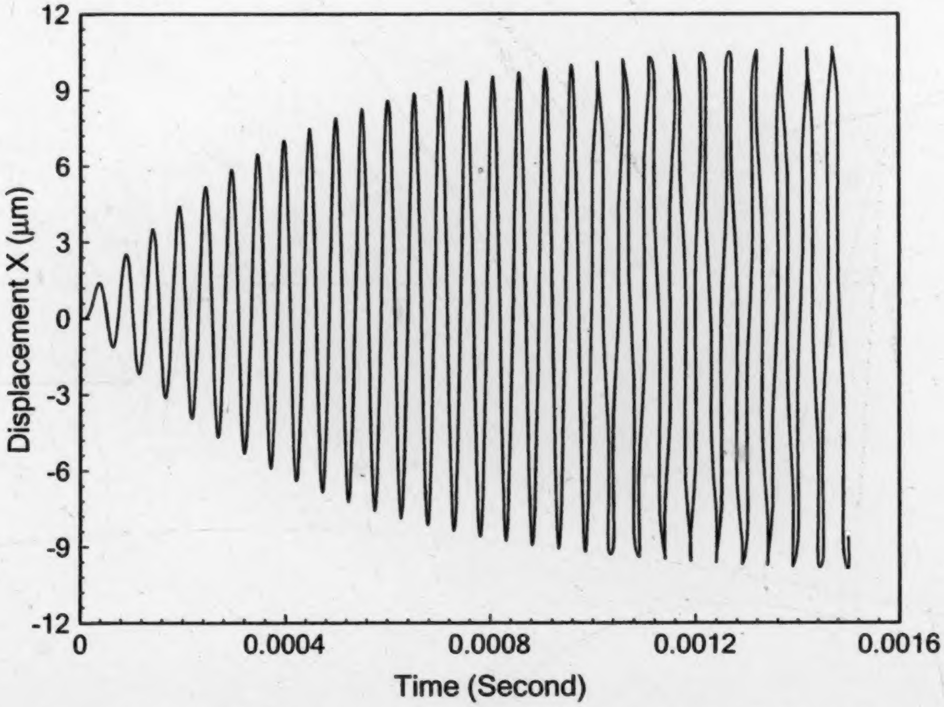

Figure 6.9: Effect of damping on Comb Drive performance at quality factor 30 during resonance

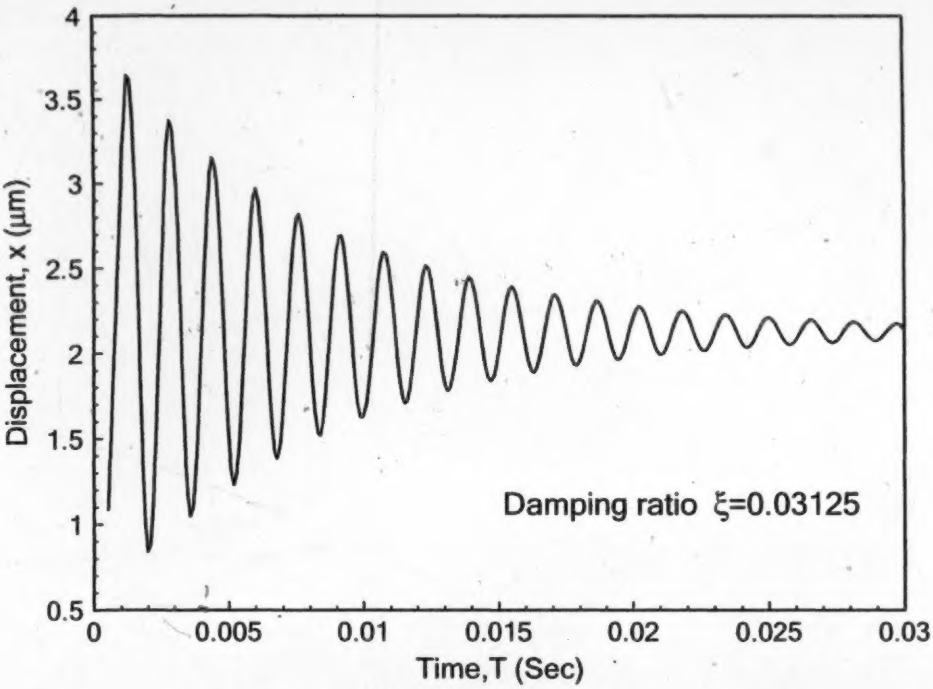

Figure 6.10: Effect of damping on Comb Drive performance at damping ratio 0.03

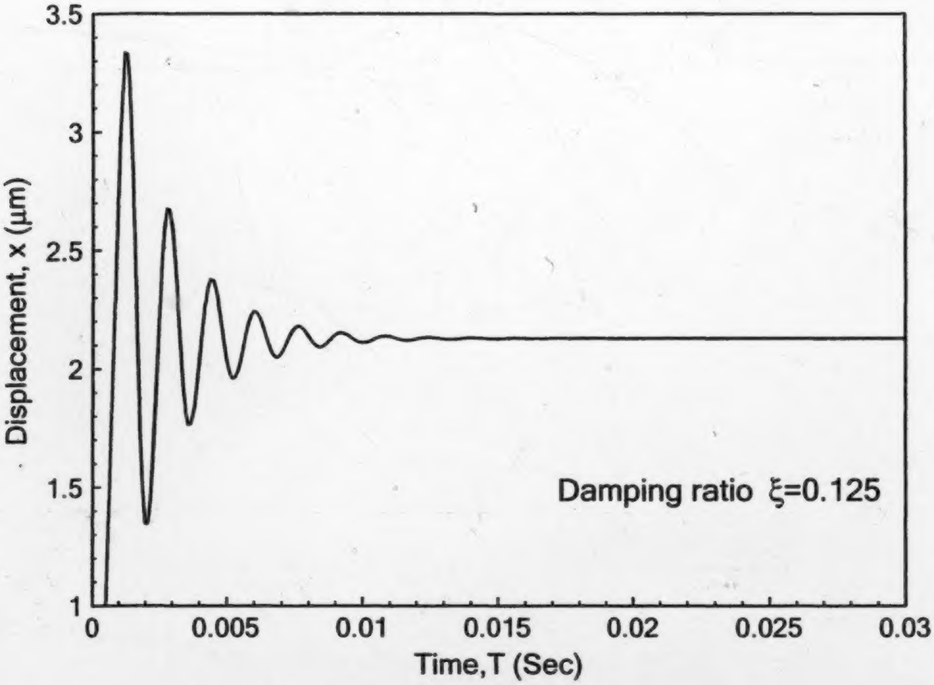

Figure 6.11: Effect of damping on Comb Drive performance at damping ratio 0. 125

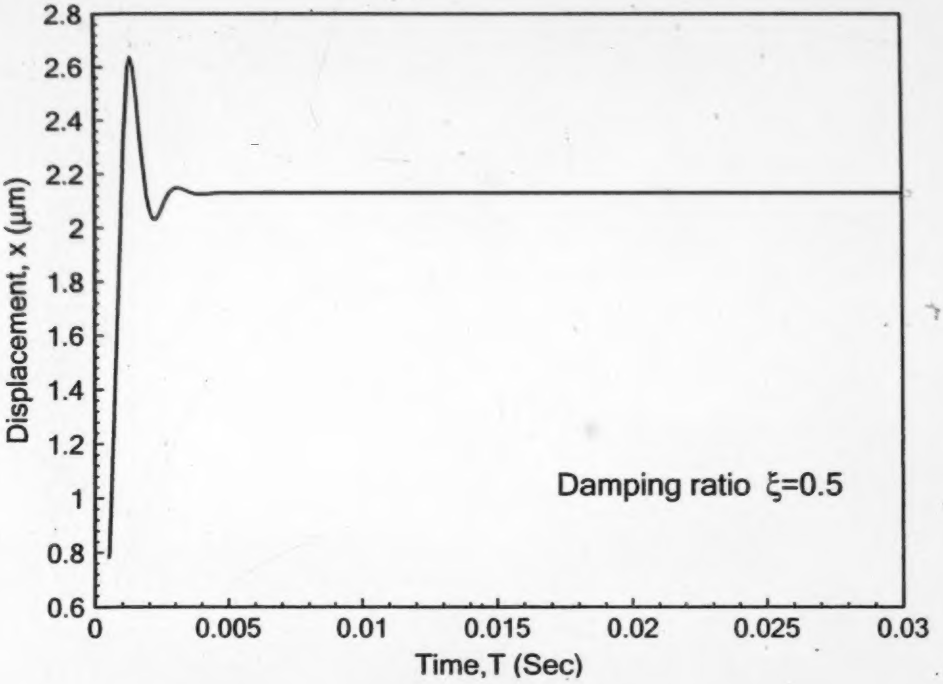

Figure 6.12: Effect of damping on Comb Drive performance at damping ratio 0. 5

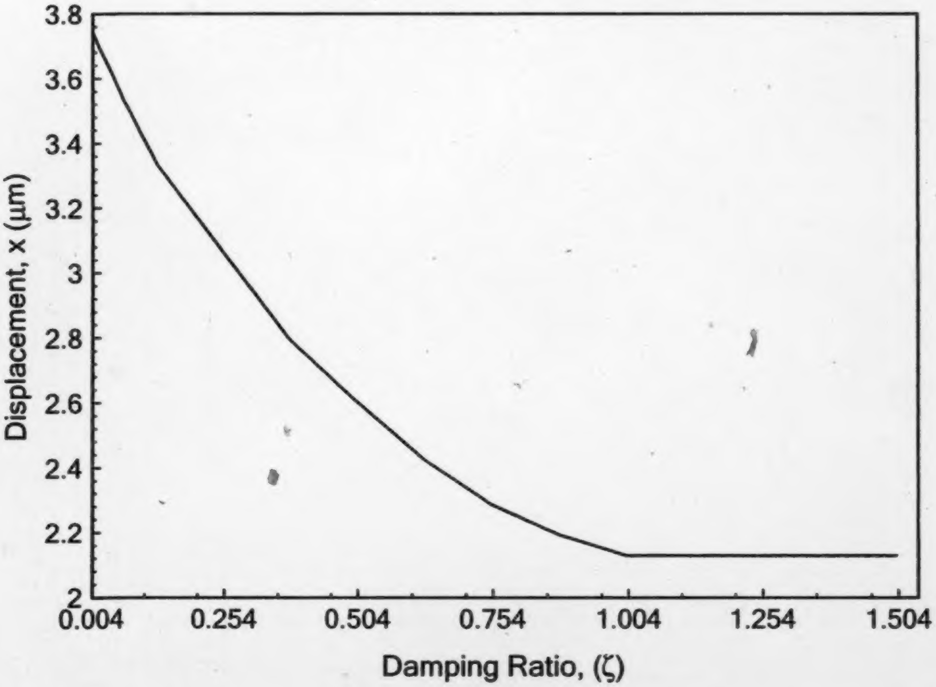

Figure 6.13: The variation of Comb Drive Displacement vs. Damping ratio at 30 Volts DC pulse

Table 6.2: Dynamic analysis results (Effect of Quality factor on system response)

No.	Quality Factor (Q)	X Displacement (μm)	Von Mises Stress (MPa)
1	10	4.6	445
2	15	6.4	463
3	20	8.6	482
4	25	11	505
5	30	12.5	527
6	35	14	550
7	40	16.6	575
8	45	18	592
9	50	20	620

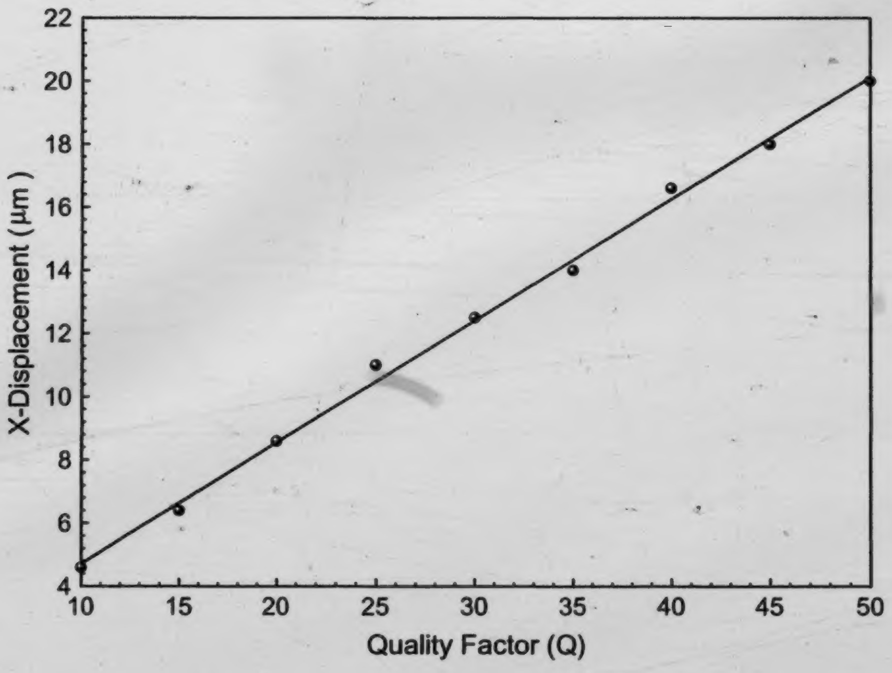

Figure 6.14: The variation of X-Displacement vs. the Quality factor for Comb Drives

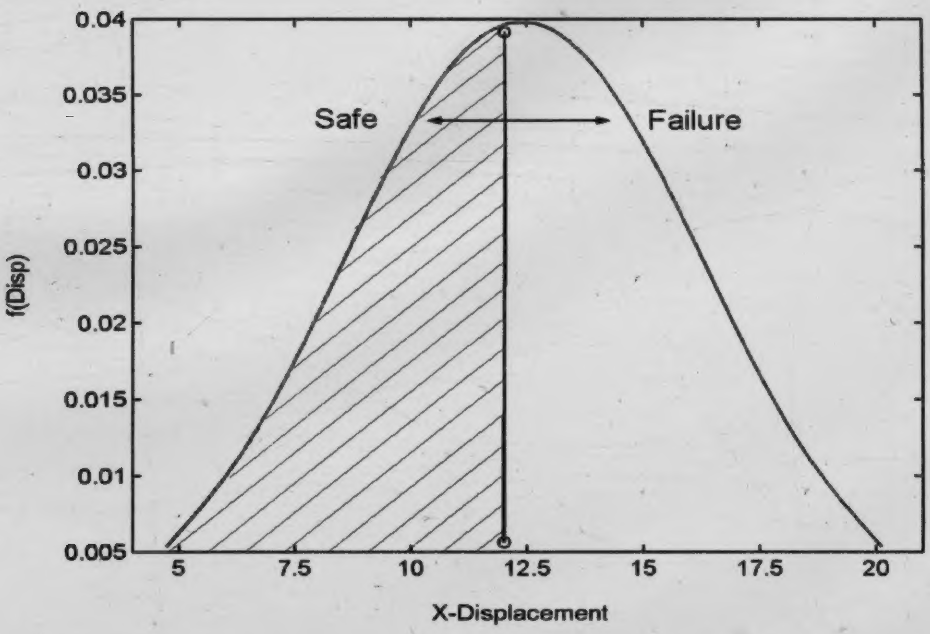

Figure 6.15: Normal distribution of X-Displacement for the Comb Drives determining Reliability rate

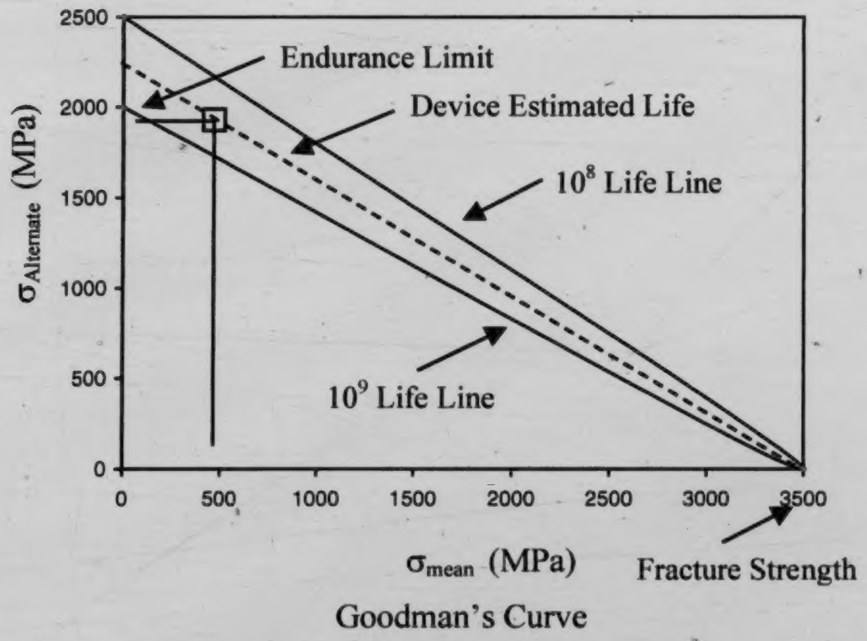

Figure 6.16: Goodman's curve for Comb life estimation

Chapter 7

Conclusions

7.1 Lateral Electrostatic Comb Drive Actuators

During the course of this work, two-dimensional and three-dimensional models for lateral electrostatic Comb Drive actuators were designed and simulated using finite element analysis (FEA). The effect of the design parameters of lateral Electrostatic Comb Drive actuators on the actuation performance was explored in both models through a parametric study. In the three-dimensional models two different meshing techniques commonly known as, the Volume Refining Meshing (VRM) method, and the Exposed Face Meshing method (EFM) were implemented. Feedforward Backpropagation neural network was developed to calibrate the (VRM) method results.

Reduced Order Modeling (ROM) principles were used to create two-dimensional FE model of lateral electrostatic comb drive actuators. In this model, the thickness, gab and overlap between the Comb fingers were varied. The design of this model was also modulated to account for the change in the number of Comb fingers and the applied driving voltage. The analytical model available from literature validated numerical simulation results. Good agreement with the analytical method over a typical range of operational voltage has been achieved. The error of the maximum displacement between both results is less than 5%. Reduced Order Modeling technique proved to be accurate and reliable method to simulate lateral electrostatic Comb Drive actuators. However, this technique has few drawbacks. For example, it gives the Comb response in terms of displacement in only one major actuation direction. In addition to that it is not possible to calculate the maximum stresses developed in the system as the system is represented by lumped elements not a real finite element domain. Also, this model is not capable of predicting the out of plane displacement.

To overcome these limitations in the 2D model, a full 3D parametric model was constructed. This 3D model utilized the application of two different meshing techniques commonly known as, the Volume Refining Meshing (VRM) method, and the Exposed Face Meshing method (EFM). The latter, showed a significant reduction in the computation time over the (VRM) method with better agreement with the analytical results. On one hand, the simulation for the displacement response for the EFM method is in a good agreement with analytical method over a typical range of operational voltages from 10 to 40 volts and the error of the maximum displacement between both results is less than 10%. On the other hand, the VRM method results are significantly deviated away from the analytical results and need to be fine-tuned. Simulation process time comparison for different meshing methods showed a 46% reduction in simulation process time over the (VRM) method. In addition to that, an accuracy improvement of 38% over (VRM) was achieved when validated with the analytical results.

However, the VRM method is characterized by the ability to develop input files that can be easily used to create the model geometry and perform the analysis process without the need to use the GUI. This advantage is highly desirable for the parametric and optimization studies. Moreover, in the EFM method the simulation process steps such as load application and mesh refinement…etc has to be performed through GUI, which is cumbersome process. Therefore, a tool based on the Artificial Neural Network was developed to calibrate the VRM results to the accurate EFM results. This tool can be used efficiently in the optimization process and could be used to speed up the simulation process. The results obtained from both meshing techniques were used to train a Feedforward Backpropagation Neural Networks. In these network models, the available finite element data were divided into two thirds for training data set and one-third for validation data set. Networks architecture were investigated and optimized for minimum network size in order to prevent network over-fitting problems and for maximum reliability and performance. These networks showed a good generalization performance and the values of the coefficients of multiple correlations, extracted from regression analysis were quite satisfactory. These networks were shown to be reliable in predicting and calibrating the FE results of the lateral Electrostatic comb-drive actuator. For displacement ratio network, a regression analysis was carried out and a correlation coefficient (R) was found to be of 0.974 for the network training data set and 0.885 for the validation data set with 5.44% mean absolute error for the training data set and 9.44% for the validation data. For the Von-Misses stress ratio network, correlation coefficient (R) was found to be of 0.95 for the network training data set and 0.871 for the validation data set with 6.87% mean absolute error for the training data set and 9.92% for the validation data set.

Finally, general overview of reliability issues related to MEMS devices were discussed, with particular attention to the lateral electrostatic Comb Drive actuators. Reliability models and different failure modes/mechanisms were explained. Both dynamic and static analyses were performed to evaluate the reliability of Comb Drive. Static analysis results showed a safe operation even at the maximum actuation range. Dynamic analysis results in conjunction with S-N data for polysilicon were used to estimate the Comb Drive lifetime. Comb Drive lifetime was found to be of $5x10^8$ cycles. In addition to that, the quality factor of the device as a parameter affect its performance was investigated and related to the device displacement based on the dynamic analysis results. Reliability rate was found to be 46% for assumed group of Comb Drive samples with quality factor variation follow a normal distribution.

7.2 Future Work

The work presented in this thesis can be continued and improved by building a MEMS device that utilizes the lateral actuation of the Comb Drive as the prime source of actuation in a system-on-a-chip MEMS application. Comb Drive can be used as the actuator to drive a micropump in Microfluidic on-a-chip systems. Applications for these systems include drug delivery, or possibly in the cooling of microprocessors actively involved in space vehicles. In addition, the constructed FE models and the neural network tool may effectively contribute to the development of reliable and optimized designs for this MEMS device.

Bibliography

[1]. Tai-Ran Hsu, "MEMS and Microsystems: Design and Manufacture." 2002, McGraw Hill.

[2]. Ernst Thielicke and Ernst Obermeier, "Microactuators and their technologies." *Journal of Mechatronics*, Vol. 10, no. 4-5, June 2000, pp. 431-455.

[3]. Hyeon-Cheol Kim Sang-Wook Lee, Keon Kuk and Yong-Soo Oh, "A monolithic inkjet print head: DomeJet." *Sensors and Actuators A: Physical*, Vol. 95, no. 2-3, 1 January 2002, pp. 114-119.

[4]. D. Dittmann M. Kohl, E. Quandt and B. Winzek, "Thin film shape memory microvalves with adjustable operation temperature." *Sensors and Actuators A: Physical*, Vol. 83, no. 1-3, 22 May 2000, pp. 214-219.

[5]. M Koch, A G R Evans, and A Brunnschweiler, "The dynamic micropump driven with a screen printed PZT actuator." *Journal of Micromechnics and Microengineering*, Vol. 8, no. 2, June 1998, pp. 119-122.

[6]. Xie HK, Pan YT, and Fedder GK, "A CMOS-MEMS mirror with curled-hinge comb drives." *Journal of Microelectromechanical Systems*, Vol. 12, no. 4, AUG 2003, pp. 450-457.

[7]. H J Cho and C H Ahn, "Magnetically-driven bi-directional optical microscanner." *Journal of Micromechanics and Microengineering*, Vol. 13, no. 3, May 2003, pp. 383-389.

[8]. Xiaorong Xiong, Yael Hanein, Weihua Wang, Daniel T. Schwartz, and Karl F. Böhringer1, "Fabrication of functional structures on thin silicon nitride membranes." *Journal of Microelectronic Engineering*, Vol. 67-68, no. 1, June 2003, pp. 422-429.

[9]. P. Attia, G. Tremblay, R. Laval and P. Hesto, "Characterisation of a low-voltage actuated gold microswitch." *Materials Science and Engineering B*, Vol. 51, no. 1-3, 27 February, pp. 263-266.

[10]. C.-J. Kim, Pisano A.P., and Muller R.S., "Silicon-processed overhanging microgripper." *Journal of Microelectromechanical Systems*, Vol. 1, no. 1, Mar 1992, pp. 31-36.

[11]. Ye Wang, Zhihong Li, Daniel T. McCormick and Norman C. Tien, "A micromachined RF microrelay with electrothermal actuation." *Sensors and Actuators A: Physical*, Vol. 103, no. 1-2, 15 January 2003, pp. 231-236.

[12]. Yang Xu, Miller S.A., and MacDonald N.C., "Microelectromechanical Scanning Tunneling Microscope." Proceedings of *The 8th International Conference on Solid-State Sensors and Actuators, 1995 and Eurosensors IX. Transducers '95.*, Vol. 1, Cornell University, 25-29 Jun, 1995, pp. 640-643.

[13]. J Brugger, V P Jaecklin, C Linder, N Blanc, P F Indermuhle, and N F deRooij, "Microfabricated tools for nanoscience." *Journal of Micromechanics and Microengineering*, Vol. 3, no. 4, December 1993, pp. 161-167.

[14]. M. Lutwyche, C. Andreoli, G. Binnig, J. Brugger, U. Drechsler, W. Häberle, H. Rohrer, H. Rothuizen, P. Vettiger, G. Yaralioglu and C. Quate, "5×5 2D AFM cantilever arrays a first step towards a Terabit storage device." *Sensors and Actuators A: Physical*, Vol. 73, no. 1-2, 9 March 1999, pp. 89-94.

[15]. Wu MC, Fan L, and Su GD, "Micromechanical photonic integrated circuits." *IEICE TRANSACTIONS ON ELECTRONICS*, Vol. E83-C, no. 6, JUN 2000, pp. 903-911.

[16]. Papautsky I, Brazzle JD, Weiss RB, Ameel TA, and Frazier AB., "Parallel sample manipulation using micromachined pipette arrays." Proceedings of *SPIE: Microfluidic Devices and Systems*, Vol. 3515, Santa Clara, California, USA., September 1998, pp. 104-114.

[17]. Chihchung CHEN, Chengkuo LEEy, Yen-Jyh LAI, and Wenchih CHEN, "Development and Application of Lateral Comb-Drive Actuator." *Japanese Journal of Applied Physics*, Vol. 42, no. 6B, Part 1, June 2003, pp. 4059–4062.

[18]. Houzego P J, "Electrostatic micromotors." Proceedings of *8th Int. Conf. Electrostatics*, Vol. 118, Oxford, UK, April 1991, pp. 2810-2812.

[19]. Gregory T.A. Kovacs, "Micromachined Transducers sourcebook." 1998, McGraw Hill.

[20]. S. Akamine, T. R. Albrecht,M. J. Zdeblick and C. F. Quate, "A planar process for microfabrication of a scanning tunneling microscope." *Sensors and Actuators A: Physical*, Vol. 23, no. 1-3, April 1990, pp. 964-970.

[21]. Rich C.A. and Wise K.D., "A high-flow thermopneumatic microvalve with improved efficiency and integrated state sensing." *Journal of Microelectromechanical Systems*, Vol. 12, no. 2, April 2003, pp. 201- 208.

[22]. Shigeaki TOMONARI, Hitoshi YOSHIDA, Masanao KAMAKURA, Kazushi YOSHIDA, Keiko KAWAHITO, and Hiroshi KAWADA Masaaki SAITOH, Saulius JUODKAZIS1 and Hiroaki MISAWA1, "Efficient Microvalve Driven by a Si–Ni Bimorph." *Japanese Journal of Applied Physics*, Vol. 42, no. 7A, Part 1, July 2003, pp. 4593–4597.

[23]. Rob Legtenberg, A W Groeneveld and M Elwenspoek, "Comb-drive actuators for large displacements." *Journal of Micromechanics and Microengineering*, Vol. 6, no. 3, September 1996, pp. 320-329.

[24]. Johnson W A and Warne L K, "Electrophysics of micromechanical comb actuators." *Journal of Microelectromechanical Systems*, Vol. 4, no. 1, March 1995, pp. 49-59.

[25]. K.E. Petersen, "Silicon as a Mechanical Material." Proceedings of *IEEE*, Vol. 70, 1982, pp. 420-457.

[26]. Howe R T and Muller R S, "Polycrystalline silicon micromechanical beams." *Journal of the Electrochemical Society*, Vol. 130, no. 06, June 1983, pp. 1420-1423.

[27]. Howe R T and Muller R S, "Resonant microbridge vapor sensor." *IEEE Transactions on Electron Devices, ED-33*, no., April 1986, pp. 499-506.

[28]. Wiliam C. Tang, Tu-Cuong H. Nguyen, and Roger T. Howe, "Laterally Driven Polysilicon Resonant Microstructures." Proceedings of *IEEE Micro Electro Mechanical Systems*, Salt Lake City, UT, U.S.A, February 20-22, 1989, pp. 53-59.

[29]. E. J. Garcia and J. J. Sniegowski, "Surface micromachined microengine." *Sensors and Actuators A: Physical*, Vol. 48, no. 3, 30 May 1995, pp. 203-214.

[30]. Frank Goodenough, "AIRBAGS BOOM WHEN IC ACCELEROMETER SEES 50-G." *ELECTRONIC DESIGN*, Vol. 39, no. 15, August 8, 1991.

[31]. V P Jaecklin, C Linder, N F de Rooij and J M Moret, "Micromechanical comb actuators with low driving voltage." *Journal of Micromechanics and Microengineering*, Vol. 2, no. 4, December 1992, pp. 250-255.

[32]. Guangya Zhou and Philip Dowd, "Tilted folded-beam suspension for extending the stable travel range of comb-drive actuators." *Journal of Micromechanics and Microengineering*, Vol. 13, no. 2, March 2003, pp. 178-183.

[33]. Wiliam C. Tang, Lim M.G., and Roger T. Howe, "Electrostatic Comb Drive Levitation and Control Method." *Journal of Microelectromechanical Systems*, Vol. 1, no. 4, December 1992, pp. 53-59.

[34]. G.K. Fedder, "Top Down Design of MEMS." Proceedings of *International Conference on Modeling and Simulation of Microsystems*, San Diego, California, U.S.A., March 27-29, 2000, pp. 7-10.

[35]. M.H. Zaman, S.F. Bart, V.L. Rabinovich, C.K. Ghaddar, I. Tchertkov and J.R. Gilbert, "A Technique for Extraction of Macro-Models in System Level Simulation

of Inertial Electro-Mechanical Micro-Systems." Proceedings of *International Conference on Modeling and Simulation of Microsystems*, San Juan, Puerto Rico, U.S.A., April 6-8, 1999, pp. 163-167.

[36]. S.F. Bart, N.R. Swart, M. Mariappan, M.H. Zaman and J.R. Gilbert, "An Environment for MEMS Design and Verification." Proceedings of *International Conference on Modeling and Simulation of Microsystems*, Santa Clara, California, U.S.A., April 6-8, 1998, pp. 386-391.

[37]. Hung E.S., Senturia S.D., "Generating efficient dynamical models for microelectromechanical systems from a few finite-element simulation runs." *Journal of Microelectromechanical Systems*, Vol. 8, no. 3, September 1999, pp. 280-289.

[38]. Guangya Zhou, Francis E.H. Tay and Fook Siong Chau, "Macro-modelling of a double-gimballed electrostatic torsional micromirror." *Journal of Micromechanics and Microengineering*, Vol. 13, no. 5, September 2003, pp. 532-547.

[39]. Ty Harness, Richard R A Syms, "Characteristic modes of electrostatic comb-drive X-Y microactuators." *Journal of Micromechanics and Microengineering*, Vol. 10, no. 1, March 2000, pp. 7-14.

[40]. Meng-Hsiung Kiang, Solgaard O., Lau K.Y. and Muller R.S., "Electrostatic combdrive-actuated micromirrors for laser-beam scanning and positioning." *Journal of Microelectromechanical Systems*, Vol. 7, no. 1, March 1998, pp. 27-37.

[41]. Sandia National Laboratories, "Sandia Lab News." Vol. 53, no. 13, June 29, 2001.

[42]. G.K. Fedder, "Simulation of Microelectromechanical Systems." UC Berkeley, *Electrical Engineering*, PhD Thesis, 1994, pp. 1-200.

[43]. Steve Groothuis, "Analyzing Microminiature Devices." *ANSYS Solutions*, Vol. 1, no. 1, Spring, 1999, pp. 12-15.

[44]. SAS IP, Inc., "ANSYS Release 6.0 user Manual" 2000

[45]. Dale Ostergaard, "Tooling Up for Microelectromechanical Systems (MEMS)." *ANSYS Solutions*, Vol. 2, no. 1, winter, 2000, pp. 22-26.

[46]. Juergen Wibbeler Jan Mehner, "Analyzing electrostatic-structural interactions in Microelectromechanical Systems." *ANSYS Solutions*, Vol. 3, no. 2, Spring, 2001, pp. 20-22.

[47]. Miklos Gyimesi Dale Ostergaard, "Finite Element Based Reduced Order Modeling of Micro Electro Mechanical Systems (MEMS)", in *International Conference on Modeling and Simulation of Microsystems"* San Diego, California, U.S.A. pp. 684 - 687.

[48]. Juergen Wibbeler Jan Mehner, "Exporting macromodels for circuit and system simulation tools." *ANSYS Solutions*, Vol. 3, no. 4, Fall, 2001, pp. 25-27.

[49]. Dale Ostergaard, Miklos Gyimesi, "Electro-Mechanical Transducer for MEMS Analysis in ANSYS." Proceedings of *International Conference on Modeling and Simulation of Microsystems*, San Juan, Puerto Rico, U.S.A., April 6-8, 1999, pp. 270 - 273.

[50]. Dale Ostergaard, Miklos Gyimesi, "Capacitance Computation with Ammeter Element." University of Toronto, Department of Electrical Engineering,

[51]. Wiliam C. Tang, "Electrostatic comb drive for resonant sensor and actuator application." California, Berkeley, *Electrical Engineering and Computer Science*, 1990.

[52]. Jan Mehner, Juergen Wibbeler, "Analyzing fluid-structural interactions." *ANSYS Solutions*, Vol. 3, no. 3, Summer, 2001, pp. 20-22.

[53]. Young-Ho Choa, Byung Man Kwaka, Albert P. Pisanob and Roger T. Howe, "Slide film damping in laterally driven microstructures." *Sensors and Actuators A: Physical*, Vol. 40, no. 1, January 1994, pp. 31-39.

[54]. Hesham Ahmed, Walied A. Moussa, Wael A. Badawy, Medhat A. Moussa, "Investigating the Design Parameters Affecting the Performance of Electrostatic Comb-Drive Actuators Using Finite Element Analysis." Proceedings of *International Conference on MEMS, NANO and Smart Systems (ICMENS'02)*, Banff, Alberta, Canada, July 20 - 23, 2002.

[55]. Walied A. Moussa, Hesham Ahmed, Wael Badawy, and Medhat Moussa, "Investigating the Reliability of Electrostatic Comb-Drive Actuators Utilized in Microfluidic and Space systems Using Finite Element Analysis." *Canadian Journal on Electrical and Computer Engineering*, Vol. 27, no. 4, October 2002, pp. 195-200.

[56]. Yie He, James Marchetti, and Fariborz Maseeh, "Improved meshing technique and its application in the analysis of large and complex MEMS systems." Proceedings of *SPIE Micromachined Devices and Components III*, Vol. 3224, 1997, pp. 238-244.

[57]. Yie He, James Marchetti, and Fariborz Maseeh, "MEMS Computer-aided Design." Proceedings of *European Design & Test Conference and Exhibition Microfabrication*, Paris, France, March 17-20, 1997.

[58]. Senturia S.D., Harris R.M., Johnson B.P., Kim S., Nabors K., Shulman M.A., and White J.K., "A computer-aided design system for microelectromechanical systems." *Journal of Microelectromechanical Systems*, Vol. 1, no. 1, March 1992, pp. 3-13.

[59]. V.I. Zhulin, S.J. Owen, and D.F. Ostergaard, "Finite Element Based Electrostatic-Structural Coupled Analysis with Automated Mesh Morphing." Proceedings of *International Conference on Modeling and Simulation of Microsystems*, San Diego, California, U.S.A., March 27-29, 2000, pp. 501 - 504.

[60]. Corning, Inc., "IntelliSense User Manual Ver 6.1" 2000

[61]. Gilbert J.R., Legtenberg R., and Senturia S.D., "3D coupled electro-mechanics for MEMS: applications of CoSolve-EM." Proceedings of *IEEE MEMS '95*, 29 Jan.-2 Feb, 1995, pp. 122-127.

[62]. X. Cai, H. Yie, P. Osterberg, J. Gilbert, S. Senturia, and J. White, "A relaxation/multipole-accelerated scheme for self-consistent electromechanical analysis of complex 3-D microelectromechanical structures." Proceedings of *the IEEE/ACM international conference on Computer-aided design*, Santa Clara, California, U.S.A., November 07-11, 1993, pp. 283-286.

[63]. Nabors K. and White J., "FastCap: a multipole accelerated 3-D capacitance extraction program." *IEEE Transactions on Computer-Aided Design of Integrated Circuits and Systems*, Vol. 10, no. 11, November 1991, pp. 1447-1459.

[64]. RD Cook, "Concepts and Applications of Finite Element Analysis." 3rd ed. 1995, John Wiley.

[65]. Fury Christ Gene A. Tagliarini, Wdward W. Page, "Optimization using Neural Networks." *IEEE Transactions on Computers*, Vol. 40, no. 12, Dec. 1991, pp. 1347-1358.

[66]. R. Paul Gorman and Terrence J. Sejnowski, "Analysis of hidden units in a layered network trained to classify sonar targets." *Neural Networks*, Vol. 1, no. 1, 1988, pp. 75-89.

[67]. J.B. Hampshire, II and Waibel, A.H., "A novel objective function for improved phoneme recognition using time-delay neural networks." *IEEE Transactions on Neural Networks*, Vol. 1, no. 2, Jun. 1990, pp. 216-228.

[68]. Liying Ma and K. Khorasani, "Application of Adaptive Constructive Neural Networks to Image Compression." *IEEE Transactions on Neural Networks*, Vol. 13, no. 5, September. 2002, pp. 1112 -1126.

[69]. Jose R. Noriega and Hong Wang, "A Direct Adaptive Neural-Network Control for Unknown Nonlinear Systems and Its Application." *IEEE Transactions on Neural Networks*, Vol. 9, no. 1, January 1998, pp. 27 -34.

[70]. A. Ongkodjojo F. E. H. Tay, Y. C. Liang, "Backpropagation approximation approach based generation of macromodels for static and dynamic simulations." *Microsystem Technologies*, Vol. 7, no. 3, October 2001, pp. 120-136.

[71]. A. Rasmussen O. Mikulchenko, K. Mayaram, "A Neural Network Based Macromodel for Microflow Sensors." Proceedings of *International Conference on Modeling and Simulation of Microsystems*, March 27-29, 2000, pp. 540-543.

[72]. Robert J. Marks Russell D. Reed, "Neural Smithing: Supervised Learning in Feedforward Artificial Neural Networks." 1999, the MIT Press.

[73]. Steffen Brueckner and Stephan Rudolph, "Neural Networks Applied to Smart Structure Control." Proceedings of *SPIE Aerosense 2000 Conference On Applications and Science of Computational Intelligence III*, Vol. 4055, Orlando, Florida, U.S.A, April 24-28, 2000.

[74]. R.J. Rider E.I. Gaura, N.C. Steele and A. Beaumont, "Smart Accelerometer Designs based on Neuro-Control Techniques." Proceedings of *the IASTED International conference on Control and Applications*, Cancun, Mexico, May 24-27, 2000, pp. 261-267.

[75]. N. Steele E.I. Gaura, and R.J. Rider, "A Neural Network Approach for the Identification of Micromachined Accelerometers." Proceedings of *International Conference on Modeling and Simulation of Microsystems*, March 27-29, 2000, pp. 245 - 248.

[76]. N. Ferreira E.I. Gaura, R.J. Rider and N. Steele, "Closed-Loop, Neural Network Controlled Accelerometer Design." Proceedings of *International Conference on Modeling and Simulation of Microsystems*, March 27-29, 2000, pp. 513 - 516.

[77]. X. P. Cheng and R. V. Patel, "Neural network based tracking control of a flexible macro–micro manipulator system." *Neural Networks*, Vol. 16, no. 2, March 2003, pp. 271-286.

[78]. W Z Lin Y C Liang, H P Lee, S P Lim, K H Lee, and D P Feng, "A neural-network-based method of model reduction for the dynamic simulation of MEMS." *Journal of Micromechanics and Microengineering*, Vol. 11, no. 3, May 2001, pp. 226–233.

[79]. L.P. Kaelbling, Littman, M.L., and Moore, A.W., "Reinforcement Learning: A Survey." *Journal of Artificial Intelligence Research*, Vol. 4, no. 1, 1996, pp. 237-285.

[80]. C. Ribeiro, "Reinforcement Learning Agents." *Artificial Intelligence Review: An International Science and Engineering Journal*, Vol. 17, no. 3, May 2002, pp. 223-250.

[81]. Richard S. Sutton and Andrew G. Barto, "Reinforcement Learning: An Introduction." 1998, Cambridge, MA, MIT Press.

[82]. Athanasios V. Vasilakos Antonios F. Atlasis, "The Use of Reinforcement Learning Algorithms in Traffic Control of High Speed Networks." Proceedings of *European Symposium on Intelligent Techniques, ESIT 2000*, Aachen, Germany, September 14-15, 2000, pp. 283 - 288.

[83]. Robert Coultrip, "A CMOS binary pattern classifier based on Parzen's method." *IEEE Transactions on Neural Networks*, Vol. 9, no. 1, January 1998, pp. 2 -10.

[84]. Thomas Martinetz Helge Ritter, and Klaus Schulten, "Neural Computation and Self-Organizing Maps - An Introduction." 1992, New York, Addison-Wesley.

[85]. D.C. Wunsch, II; Caudell, T.P.; Capps, C.D.; Marks, R.J., II; Falk, R.A., "An optoelectronic implementation of the adaptive resonance neural networks." *IEEE Transactions on Neural Networks*, Vol. 4, no. 4, July. 1993, pp. 673-684.

[86]. Beale M. Demuth H., "Neural Network Toolbox: User's Guide; For Use with Matlab", Version 4.

[87]. David J.C MacKay, "Bayesian Interpolation." *Journal of neural computation*, Vol. 3, no. 4, May 1991.

[88]. Sapiyan Baba Sameem Abdul-Kareem, Yong Zulina Zubairi, U Prasad, Mohd Ibrahim A Wahid, "BACK PROPAGATION NEURAL NETWORK FOR MEDICAL PROGNOSIS: A COMPARISON OF DIFFERENT TRAINING ALGORITHMS." *Electronic Journal of the School of Advanced Technologies*, Vol. 3, no. 1, April 2001.

[89]. Hesham Ahmed, Walied A. Moussa, "Optimizing the Performance of Electrostatic Comb-Drive Actuators Using Neural Networks." Proceedings of *International Conference on MEMS, NANO and Smart Systems (ICMENS'03)*, Banff, Alberta, Canada, July 20 - 23, 2003, pp. 62-68.

[90]. Feynman R.P., "There's plenty of room at the bottom [data storage]." *Journal of Microelectromechanical Systems*, Vol. 1, no. 1, March 1992, pp. 60 -66.

[91]. De Wolf I, "MEMS reliability." *Journal of MICROELECTRONICS RELIABILITY*, Vol. 43, no. 7, July 2003, pp. 1047-1048.

[92]. B. Stark, "MEMS Reliability Assurance Guidelines for Space Applications." Jet Propulsion Laboratory, California Institute of Technology, Pasadena, CA, U.S.A, January 1999

[93]. W. Merlijn van Spengen, "MEMS reliability from a failure mechanisms perspective." *Journal of MICROELECTRONICS RELIABILITY*, Vol. 43, no. 7, July 2003, pp. 1049-1060.

[94]. M. Tabib-Azar, K. Wong and Wen Ko, "Aging phenomena in heavily doped (p+) micromachined silicon cantilever beams." *Sensors and Actuators A: Physical*, Vol. 33, no. 3, June 1992, pp. 199-206.

[95]. W. MERLIJN VAN SPENGEN, ROBERT PUERS, and INGRID DE WOLF, "On the physics of stiction and its impact on the reliability of microstructures." *Journal of Adhesion Science & Technology*, Vol. 17, no. 4, 2003, pp. 563–582.

[96]. Niels Tasy, Tonny Sonnenberg, Henri Jansen, Rob Legtenberg and Miko Elwenspoek, "Stiction in surface micromachining." *Journal of Micromechanics and Microengineering*, Vol. 6, no. 4, December 1996, pp. 385-397.

[97]. Roya Maboudian and Roger T. Howe, "Critical Review: Adhesion in surface micromechanical structures." *Journal of Vacuum Science & Technology B*, Vol. 15, no. 1, January 1997, pp. 1-20.

[98]. S. L. Miller, M. S. Rodgers, G. LaVigne, J. J. Sniegowski, P. Clews, D. M. Tanner, and K. A. Peterson, "Failure Modes in Surface Micromachined Microelectromechanical Actuators." Proceedings of *IEEE International Reliability Physics Symposium*, March 31-April 2, 1998, pp. 7-25.

[99]. Danelle M. Tanner, "Reliability of Surface Micromachined Microelectromechanical Actuators." Proceedings of *International Conference in Microelectronics*, Nis, Yugoslavia, May 2000, pp. 97-104.

[100]. Toshiyuki Tsuchiya , Osamu Tabata, Jiro Sakata, and Yasunori Taga, "Specimen size effect on tensile strength of surface-micromachined polycrystalline silicon thin films." *Journal of Microelectromechanical Systems*, Vol. 7, no. 1, March 1998, pp. 106-113.

[101]. Robert C. Juvinall and Kurt M. Marshek, "Fundamentals of Machine Component Design." 2000, John Wiley.

[102]. Jonathan W Wittwer, Troy Gomm, and Larry L Howell, "Surface micromachined force gauges: uncertainty and reliability." *Journal of Micromechanics and Microengineering*, Vol. 12, no. 1, January 2002, pp. 13-20.

[103]. Bustillo J.M., Howe R.T., and Muller R.S., "Surface micromachining for microelectromechanical systems." Proceedings of *THE IEEE*, Vol. 86, No. 8, August 1998, pp. 1552 -1574.

[104]. Aris Christou, "Materials and reliability issues in MEMS and Microsystems." Proceedings of *6th European Symposium on Reliability of Electronic Devices, Failure Physics and Analysis*, Bordeaux, France, 1995.

[105]. L.A. Starman Jr., J.A. Lotta, M.S. Amer, W.D. Cowan, and J.D. Busbee, "Stress characterization of MEMS microbridges by micro-Raman spectroscopy." *Sensors and Actuators A: Physical*, Vol. 104, no. 2, April 2003, pp. 107–116.

[106]. C.L. Muhlstein, S.B Brown, and R.O. Ritchie, "High-cycle fatigue and durability of polycrystalline silicon thin films in ambient air." *Sensors and Actuators A: Physical*, Vol. 94, no. 3, November 2001, pp. 177-188.